

In The Name of God

Journal of Interfaces, Thin Films and Low dimensional systems

Volume 4, Issue 2, Winter and Spring, 2021

Publisher: **Alzahra University**

Chief Executive: **F. Shahshahani:** *Associate Professor of Physics, Alzahra University*

Editor-in-chief: **A. A. Masoudi:** *Professor of Physics, Alzahra University*

English Editor: **S. Vasheghani Farahani:** *Associate Professor of Physics, Tafresh University*

Managing Director: **Z. S. Hosseini:** *Assistant Professor of Physics, Nuclear Science and Technology Research Institute*

Editorial Board

- **H. Hakimi Pajouh:** *Associate Professor of Physics, Alzahra University*
- **R. Malekfar:** *Professor of Physics, Tarbiat Modares University*
- **E. Mohajerani:** *Professor of Physics, Shahid Beheshti University*
- **A. Morteza Ali:** *Professor of Physics, Alzahra University*
- **G. Palasantzas:** *Professor of Physics, University of Groningen, Netherlands*
- **K. Ravichandran:** *Associate Professor of Physics, A.V.V.M Sri Pushpam College, India*
- **S. Rouhani:** *Professor of Physics, Sharif University of Technology*
- **F. Shahbazi:** *Associate Professor of Physics, Isfahan University of Technology*
- **S. Uyaver:** *Associate Professor of Physics, Turkish-German University of Istanbul, Turkey*

Contents

- 1. An evaluation for CIGS based thin-film solar cells development**
Mojtaba Jamiati 365
- 2. Thermal entanglement in spin chain with XX, XY, and XZ Heisenberg interactions**
Maryam Mahmoudi, Mohammad Reza Soltani, and Arezu Jahanshir 379
- 3. DFT study of silicon channel effects embedded between armchair graphene nanoribbons with different widths on mechanical and electronic properties**
Mehdi Zarepour 385
- 4. Effect of vacancy defects on the Josephson current in zigzag graphene narrow strips**
Somayyeh Zareei, Vahid Daadmehr, Hossein Hakimi Pajouh, Zahra Faraei 393
- 5. Optimization of electron scattering from random potential barriers on the surface of topological insulators**
Hamid Dehnavi, Mehdi Saadat 405
- 6. Electrical properties of magnetic tunnel junctions affected by two types of interfacial roughness**
Zhaleh Ebrahimnejad 415



An evaluation for CIGS based thin-film solar cells development

Review paper

Mojtaba Jamiati*

Department of Physics, Naragh Branch, Islamic Azad University, Naragh, Iran

ARTICLE INFO

Article history:

Received 14 March 2021

Revised 20 November 2021

Accepted 20 November 2021

Available online 8 December 2021

Keywords:

Solar cell

CIS

CIGS

Thin film

Photovoltaic

ABSTRACT

Thin film solar cells are desirable due to minimal material usage, cost effective synthesis processes, and a promising trend in efficiency rise. This review summarizes the current status of chalcopyrite $\text{Cu}(\text{InGa})(\text{S,Se})_2$ (CIGS) thin film solar cell technology with a focus on recent advancements and emerging concepts intended for higher efficiency and novel applications. The recent developments and trends of research in laboratory and industrial achievements communicated within the last years are reviewed and the major developments linked to alkali post deposition treatment and composition grading in CIGS, surface passivation, buffer and transparent contact layers are emphasized. In recent years, a lot of effort has been initiated to develop low-cost thin-film solar cells, which are alternatives to high-cost silicon (Si) solar cells. Copper Indium Gallium Selenide (CIGS) based solar cells have become one of the most promising candidates among the thin film technologies for solar power generation. The current record efficiency of CIGS has reached 22.6%, which exceeds the current multi crystalline Si record efficiency (21.9%). However, material properties and efficiency on small area devices are crucial aspects to be considered before manufacturing into large scales. Chalcopyrite-based solar cells were first developed using CuInSe_2 absorber material, but it quickly became dependent on the $[\text{Ga}/(\text{In} + \text{Ga})]$ ratio. CIGS and related alloys are a direct band gap semiconductor with high efficiency, low cost, large absorption coefficient, and very good stability in outdoor tests.

1 Introduction

At the beginning of the 21st century, numerous different energy sources were used to satisfy the World's need for electricity. The sunlight is one of the largest energy sources in nature. However, so far human has not been able to provide a large share of his energy from this source. Hence, in recent decades, extensive efforts have been done in solar cells modeling and fabricating to use this energy. In order to convert this energy to a usable form, special absorbent materials are needed, which (1) have optimum bandgap to sunlight energy and (2) are not harmful to the environment [1]. The sun is the most abundant source of renewable energy to meet up the present and

future global energy demands in terawatt (TW) scale deployment. In this direction, solar cell is one of the best possible means for directly converting sunlight into usable energy without producing any harmful by products. In general, there are two approaches for the conversion of harvested sunlight into electricity, namely single junction and multi junction solar cells.

Among all types of solar cells, second generation thin film cells are favorable because of their low cost material usage and promising trend in efficiency rise. Although first generation silicon (Si) solar cells are still dominant players in photovoltaic (PV) literatures, Silicon (Si) solar cells dominate the PV market (92%) followed by cadmium telluride

*Corresponding author.

Email address: drmjamiati@gmail.com

DOI: 10.22051/jitl.2022.35435.1051

(CdTe, 5%), copper indium gallium selenide (CuInGaSe₂ or CIGS, 2%) and amorphous silicon (a-Si:H, ~1%). Si wafer with thickness around 180µm is the traditional material being used for module manufacturing and it has attained significant level of maturity at the industrial level. Its production cost is a major concern for energy applications. About 50% of the cost of Si solar cell production is due to Si substrate while device processing and module processing accounts for 20% and 30% respectively [2].

Alternate to Si solar cells are thin film solar cells fabricated on glass substrates. The main demerits of using glass substrates are fragile nature of modules, cost of glass wafer having thickness of 300–400µm, and low specific power (kW/kg) etc. Specific power is an important factor when solar cells are used in space applications. A high specific power exceeding 2 kW/kg can be achieved by flexible solar cells on polymer films which is useful for terrestrial as well as space applications. Production cost can be lowered by using flexible substrates and roll-to-roll production (R2R) technique. However, flexible solar cell technology is less mature when compared to the cells fabricated on rigid substrate counterparts. Due to four main requirements - high efficiency, low-cost production, and high throughput and high specific power, a major research and development focus has been shifted towards flexible solar cells. It can offer a unique way to reach terawatt scale installation by using the high throughput R2R fabrication technique [3].

The process of cost reduction in non-Si thin-film solar cells is easier than Si solar cells. We can obviously improve the performance of thin solar cells whereas the parameters connected with Si solar cell efficiency are not capable to be enhanced. The main drawback with the Si solar cells is that it is an indirect band gap semiconductor and needs a thick layer around 180-300 µm to absorb photons [4].

The band gap of 1.1 eV for Si does not absorb more than 50% of the visible spectrums. CIGS cell efficiency and stability are comparable to Si solar cells. Recently, Tiwari group (EMPA Switzerland) reported a record efficiency of 20.4% on flexible polymer foil (23% in glass), independently confirmed by Fraunhofer Institute for Solar Energy Systems Freiburg [5]. Recently, the same group reported an

efficiency of 20.8% using low temperature processing of 450°C [6]. Similar to the CIGS absorber, CdTe is also an excellent absorber material for thin film solar cells due to its ideal bandgap of ~1.5 eV.

In the TFSCs family, cuprous sulfide-cadmium sulfide (Cu₂S/CdS) single junction is the first reported solar cell developed for space applications that showed high efficiency (~9.1%). Several start-up companies have been established to commercialize this technology but diffusion of copper into CdS matrix and doping of the CdS layer led to long-term performance degradation, for which most of the research activities on Cu₂S/CdS cells were declined [7]. Eventually, other genre of TFSCs took over the researchers and manufacturers interests. Among these TFSCs, amorphous silicon (a-Si) solar cell is preferable to researchers because of its material availability, non-toxicity, low processing temperature, and low cost. Meanwhile, chalcopyrite based CIGS solar cells showed comparable efficiencies to the polycrystalline Si solar cell, but the production cost of this cell is reported to be much lower than that of the polycrystalline Si solar cell. One of the major barriers in commercialization of this cell is the resource limitation, since Indium (In) and Gallium (Ga) are considered as scarce materials. On the other hand, quaternary semiconducting compound Copper Zinc Tin Sulphide (CZTS) is anatomically similar to CIGS but uses the earth-abundant elements that alleviate the material scarcity issue precluding CIGS cell potentials. Recently, a promising binary material: Cadmium Telluride (CdTe) is showing much promises due to its frequently reported higher efficiencies in comparison to polycrystalline Si solar cells [8] despite its growth nature and crystal structure is remarkably different from other p-n junction based TFSCs. As a result, CdTe received more attention than other TFSC materials as an absorber for achieving a highly efficient and low-cost solar cell. Besides, non p-n junction based DSSC cells are unique among the TFSCs in terms of structure, light absorption capacity, electron and hole transport mechanism etc. It is also a promising candidate in the TFSC technology, because of its cheap constituent materials without requiring higher purity which lowers the fabrication cost [9].

The aim of this research is to study the properties of thin films to search for the suitability of these films for the manufacture of solar cells

based on Cu(InGa)Se_2 semiconductor material for better utilization of the solar spectrum to yield higher efficiency and performance stability. Existing issues to be solved are discussed and methods to further improve the cell performance are suggested. Future prospects of these solar cells are outlined.

2 Inception and progress

History of CIGS thin-film solar cells accounts that, the first CuInSe_2 (CIS) thin film was synthesized by Hahn in 1953 [10]. The very first CIS material being synthesized was in 1953, and then, an efficiency of 12% has been reported for single crystal CuInSe_2 -based solar cells in 1974 [11]. In 1976, the first CIS thin film solar cell with buffer layer CdS was fabricated with an efficiency of 4–5% by evaporating CuInSe_2 powder in the presence of excess Se vapor (coevaporation) [12]. CIG-based thin film solar cell (CuInSe_2) started to receive even more attention in 1981 when Mickelsen and Chen achieved an efficiency of 9.4% by using a coevaporation technique from an evaporated n-type CdS atop the crystalline p- CuInSe_2 onto inexpensive substrates [13]. Incorporation of Ga into the CIS matrix to raise the absorber bandgap, open-circuit voltage and a fill factor led to achieve high efficiency CIGS cell fabricated by PVD of the constituent elements on the Mo-coated soda lime glass substrate. To date, NREL is a leading research organization in CIGS solar cell development. The record efficiencies of this solar cell reported by NREL were 17.1% in 1995 [14], 18.8% in 1999 [15], and 19.9% in 2008 [16]. For depositing absorber layer, glass substrate is the most commonly used substrate; however, the current trend is to develop flexible solar cells on metal foils [17-19] where by using alternative of metal foil substrates, the first report in the use of polyimide as a flexible substrate and a CIGS cell has been developed by a two-step process of sputtering metal precursors [10-22]. In 1992, the absorber layer has been deposited on flexible Mo, Ti, and Al foils by using an e-beam evaporation process with subsequent selenization [23] and state-of-the-art highest efficiency CIGS solar cells were prepared on polymer foil 2013 [24]. The efficiency champion CIGS solar cell fabricated by CIS absorber engineering and enhanced surface treatment of the absorber layer using a co-evaporation process on rigid glass substrate has been reported about 22.6% [25].

3 Crystal structure of CIGS

The I–III–VI₂ ternary compounds CuInSe_2 (CIS), CuGaSe_2 (CGS), and their alloy are well known to crystallize in chalcopyrite (ch) structure with tetrahedral bonding character [26,27]. Figure 1 depicts the chalcopyrite CIGS Crystal structure [28]. Each I(Cu) or III(In) atom has four bonds to the VI atom(Se).

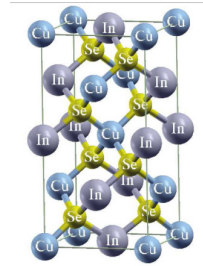


Figure 1. Tetragonal unit cell of CuInSe_2 [28]. Permission to use this figure has been obtained from the relevant journal.

The ternary chalcopyrites crystallize in the tetragonal structure type of space group I42d. Thus the chalcopyrite structure is a super-lattice of the Zinc Blende structure (ZnS) by doubling its unit cube along the z-axis converted to the c-axis of the chalcopyrite structure. In most real chalcopyrite crystals, the ratio of c/a is approximately equal to two, whereas in an ideal chalcopyrite structure the ratio of the unit cell length c to a is equal to two. The tetrahedral coordination implies that the bonding is primary covalent with SP^3 hybrid bonds prevalent, although there is some ionic character because the atoms are different. I–III–VI₂ compounds can be regarded as the ternary analogs of the II–VI binary compounds with some interesting structural anomalies relative to their binary nature. First, unlike their binary analogs, the ternary chalcopyrites have two different cations, e.g. ZnSe and CuGaSe_2 . Starting from the A atom and translating it into the vertical direction through intervals of $c/2$, the sequence ABAB can be found, whereas horizontal translation with an interval of A , the sequence AAAA can be found. Secondly, the ratio of the lattice parameters $n = c/2a$ differs from 1 by about 2%. Thirdly, the anions are displaced from their zinc-blende sites. This reflects the fact that each cation A has four anions X as nearest neighbors in binary AX, Zinc Blende compounds, whereas in a ternary chalcopyrite ABX_2 , each cation A and B has four anions X as nearest neighbors, and each anion has two A and B cations as the nearest neighbors. As a result,

the anion X usually adopts an equilibrium position closer to one pair of cations than to the other, which results in unequal bond lengths $R_{AX} \neq R_{BX}$ (bond alternation). The nearest neighborhood anion–cation bond lengths are given by:

$$R_{AX} = a \left[U^2 + \frac{(1+n)^2}{16} \right]^{1/2},$$

and

$$R_{BX} = a \left[\left(U - \frac{1}{2} \right)^2 + \frac{(1+n^2)}{16} \right]^{1/2}.$$

Hence, the anion displacement $U - 1/4 = (R_{AX}^2 - R_{BX}^2)/a^2$ shows the extent of bond alternation in the system. The structural anomalies $n - 1$ and $u - 1/4$ relative to the Zinc Blende structure ($n = 1$ and $u = 1/4$) are seem to be significant [29].

4 Electronic properties

Among group II-VI compound semiconductor nanoparticles, ZnS and CdS are the most promising materials. ZnS is a good material for detecting ultraviolet and violet radiation due to its primary band gap of 3.68 eV (345 nm) and high sensitivity. It has potential applications in optics, optoelectronics, and solar energy. CdS with a direct band gap of 2.42 eV (515 nm) has applications in window layers, light emitting diodes, and photodetectors. Its applications in photodetector and solar cells when used in conjunction with narrow band gap materials such as CdTe have been reported [30].

Here we describe the energy band structure and the electronic charge distribution in CuInSe_2 and CuGaSe_2 , the simplest ternary analogs of II-IV zincblende compounds. The uppermost valence bands of I-III-VI₂ compounds are profoundly influenced by the proximity of noble metal d-levels in the valence band. The presence of the noble metal d-levels in the valence band has been confirmed directly by the observation of electro reflectance structure due to transitions from the d-levels themselves to the lowest conduction band minimum [31]. The energy gap is 1.3 eV less than that of the binary analog $\text{Zn}_{0.5}\text{Cd}_{0.5}\text{Se}$, and the spin-orbit parameter of 0.23 eV is considerably less than that of measured in CdSe. These two anomalies, the downshift of the energy gaps relative to the binary analogs, and reduced spin-orbit splitting have been observed to various degrees in all I-III-VI₂ compounds investigated. Shay and Kasper [32]

have pointed out that the anomalous reduction in the band gaps of ternary chalcopyrite related to their binary analogs are correlated with the existence of d bonding in former compounds. They found that the band gap anomaly ΔE_g correlates almost linearly with the percentage of d character, αd , deduced by comparing the spin-orbit splitting of the ternary and binary compound, i.e., $\Delta E_g = a \alpha d$ with $a \approx 3.125$ eV. They have suggested that CuInSe_2 and CuGaSe_2 have a nearly constant percentage of d character ($\alpha d = 0.34$ and 0.36 , respectively). The I-III-VI₂ ternary compounds (CuInSe_2 , CuGaSe_2 , and their alloys $\text{CuIn}_x\text{Ga}_{1-x}\text{Se}_2$) are promising materials for thin-film solar cells with high conversion efficiencies and low production costs [33,34].

The reason CIGS has been one of the most promising absorber layers for thin film photovoltaic devices is due to its high absorption coefficient for solar radiation and compatibility of its bandgap (1.6 eV–1.0 eV) [35]. The advantages of CIGS-based solar cells over CIS-based solar cells are as follows: (i) the bandgap can be tuned by adjusting the Ga/In ratio to match the solar spectrum. If all indium (In) is replaced by gallium (Ga), the CIGS bandgap increases from about 1.04 eV to 1.68 eV [36]. It has been stated that CIGS absorber layer can absorb most parts of the solar spectrum with a thickness of $1 \mu\text{m}$ [35]. Hence, a layer thickness of $\sim 2.0\text{--}2.5 \mu\text{m}$ will be sufficient for the completed device, and a thinner layer device means reduction in raw material usage and lower production cost incurred. (ii) Ga incorporation can also improve the open-circuit voltage V_{oc} of CIGS since $V_{oc} \sim E_g/2$ (E_g is referring to bandgap) [37].

The electronic properties of I-III-VI₂ semiconductors have been subject of study for nearly 40 years by different authors using distinct methodologies. As representative examples, we can mention the seminal work of Jaffe and Zunger where they studied self consistently within the density-functional theory (DFT), the chemical trends in the electronic structure of six Cu-based ternary chalcopyrite semiconductors including CuGaS_2 [34,35]. They reported 1.65 and 1.25 eV for the energy gap of CuAlSe_2 and CuGaS_2 , far from the accepted experimental values 2.65 and 2.43 eV, respectively. Using full-potential linear muffin-tin orbital method based on the local-density approximation and with the Hedin and Lundqvist

parametrization for the exchange and correlation potential, Ahuja et al, obtained a similar value for the energy gap of CuGaS₂ (1.2 eV) [38].

The first theoretical investigation of chalcopyrite semiconductors was published by Jaffe and Zunger in 1983 [38]. They calculated lattice parameters, tetragonal distortions, anion displacements, and band-structures of CuGaS₂, CuInS₂, CuGaSe₂, and CuInSe₂. In 1992, Wei, Ferreira, and Zunger used ab initio electronic structure calculations, the cluster expansion technique, and Monte Carlo simulations to calculate the order-disorder transition temperature for CuInSe₂ [39]. These researches support the statement that particular combination of methods can accurately describe the complex behavior of solids. In the mid-1990s, simulations were extended beyond the absorbing materials. Wei, Zhang, and Zunger looked at the CuInSe₂/CdS heterojunction of CIGS solar cells [40]. They calculated the band offsets for this essential part of the cell. Subsequently, Wei, and Zunger added the investigation of optical bowing parameter [41]. Gloeckler and Sites (2005) by numerical studies found that band gap grading can provide a beneficial effect on the solar cell [42]. Zhang et al. (1997,1998) published fundamental papers on defects in CuInSe₂[43,44]. They contain the calculation of defect levels and formation energies of defected complexes. A subsequent study by the same authors focused on the influence of Na on the electrical and structural properties of CuInSe₂[45]. In 1998, Wei, Zhang, and Zunger dealt with the issue of Ga addition to CuInSe₂ [46], providing a comprehensive picture of how Ga influences the band gap. The topic was recently revisited and extended by Huang [47]. He used computer simulations to show that a band gap of 1.5 eV should lead to the greatest efficiency and explains why record efficiency CIGS solar cells have a much lower band gap of about 1.15 eV.

The reason is that the open circuit voltage does not increase with increasing the Ga content above a gap of 1.15 eV. Lately, a lot of studies have been dedicated to grain boundaries. They seem to be important for good solar cells, because cells made from monocrystalline CIGS perform worse than polycrystalline cells [48]. In 2005, Gloeckler et al. studied the recombination of charge carriers at grain boundaries with two-dimensional simulations [49].

An important step towards cheaper solar cells would be the replacement of In and Ga by cheaper materials. In 2005, Raulot, Domain, and Guillemoles studied potential In- and Ga-free absorbers with ab initio methods [50].

Reduce the material costs, the expensive group-III elements (In and Ga) can be substituted by group-II-IV elements (Zn plus Sn) (CZTSe) i.e. sulfide counterpart Cu₂ZnSnS₄ (CZTS). A 1.04 eV voltage for CuInSe₂ can be tuned from for CuInSe₂ over 1.54 eV for CuInS₂ and to 1.68 eV for CuGaSe₂ to achieve a desired value and an enhanced current conversion efficiency [51, 52].

By using heterostructures in materials with different band gap (Table 1), the lattice constants must match to avoid dislocations/defects appearance at the interface. These dislocations/defects act as recombination centers and decrease the performances of solar cells.

Table 1. Band energy gap of thin-film absorbers.

absorber	M		Ref.
CuInSe ₂	HSE	0.76	[53]
	GW	0.79	
	GW	1.04	
CuIn _{0.75} Ga _{0.25} Se ₂	LDA	0.8	[54]
	GGA	0.7	
CuIn _{0.5} Ga _{0.5} Se ₂	LDA	0.9	[54]
	GGA	0.8	
CuIn _{0.25} Ga _{0.75} Se ₂	LDA	1.2	[54]
	GGA	0.8	
CuGaSe ₂	HSE	1.35	[53]
	GW	1.56	
	GW	1.663	

5 Optical properties of CIGS

The study of the optical functions helps to give a better understanding of the electronic structure which can find potential applications in photoelectron devices and the semiconductor industry. The optical properties may be obtained from the complex dielectric function:

$$\varepsilon(\omega) = \varepsilon_1(\omega) + i\varepsilon_2(\omega). \quad (1)$$

The imaginary part of the dielectric function (ε) is calculated as follows:

$$\begin{aligned} \mathcal{E}_2^{\alpha\beta}(\omega) &= \frac{4\pi^2 e^2}{\Omega} \lim_{q \rightarrow 0} \sum_{c,v,k} 2W_k \delta(E_{cK} - E_{vK} \\ &- \omega) \langle u_{cK+e_{\alpha}q} | u_{vK} \rangle \langle u_{cK+e_{\beta}q} | u_{vK} \rangle^*, \end{aligned} \quad (2)$$

where k , c , and v are the Bloch wave function vector, conduction band, and valance band respectively. E_{jk} is the single-electron energy state of band j in wave vector k , while U_{jk} is the cell periodic part of the wave function. Ω is the volume of primitive cell. W_k is the k -point weight, and e_{α} is the unit vector in the Cartesian coordinates system.

The real part of the dielectric function is given by the Kramers-kronig relation:

$$\begin{aligned} \mathcal{E}_1^{\alpha\beta}(\omega) &= 1 + \frac{2}{\pi} P \int_0^{\infty} \frac{\mathcal{E}_2^{\alpha\beta}(\omega') \omega'}{\omega'^2 - \omega^2 + i\eta} d\omega', \end{aligned} \quad (3)$$

where P is the principal value and η is an infinitesimal number. The knowledge of both the real and imaginary parts of the dielectric function make it possible to calculate other optical properties. Since the electron-optical phonon coupling is not considered in the calculations, we cannot describe the static dielectric constant \mathcal{E}_0 . The high-frequency dielectric constant \mathcal{E}_{∞} is experimentally determined in the in-gap region [i. e., $\mathcal{E}_{\infty} \approx \mathcal{E}_1(0 \ll \omega \ll E_g)$]. In our calculations, this constant is determined from the dielectric function at $\mathcal{E}_1(\omega=0)$ and complementary also at $\mathcal{E}_1(\omega = \frac{E_g}{2})$. The absorption coefficient is obtained directly from the dielectric function by:

$$\alpha(\omega) = \frac{\sqrt{2}\omega}{c} [\sqrt{\mathcal{E}_1(\omega)^2 + \mathcal{E}_2(\omega)^2} - \mathcal{E}_1(\omega)]^{1/2}, \quad (4)$$

where c is the speed of light.

The maximum optical absorbance of the CIGS films was found with the films deposited on Mo substrate as compared to the other substrates. The absorption shift towards higher wavelengths may be attributed to the increase of crystallinity and growth in grain size which is already confirmed by XRD and SEM analysis. The highest transmittance value is observed for the CIGS deposited on ITO approximately 30% and for the Mo-

CIGS film with lower transparency of 20%. This transparency is interconnected to the optical band gap which shows precise absorption edge to the optical band gap of the CIGS films deposited on Mo. This tendency of transmission spectra supports the AFM analysis of the films which could be attributed to the increment in the surface roughness that might occur to the influences on the transmission of the incident light due to the light scattering [55].

The average dielectric functions $E(\omega)$ generated by the GW method are shown in Fig. 2 [53]. Overall, all compounds show similar dielectric functions over a broad range of energy. The main difference is related to the variation in the energy gap and onset to absorption. This directly affects the real part of the dielectric function since a large gap usually implies a small dielectric constant.

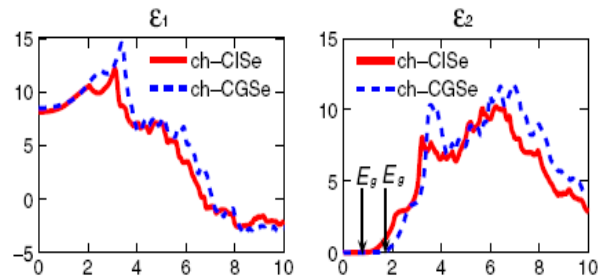


Figure 2. The average dielectric function $\mathcal{E}(\omega) = [2\mathcal{E}^{\perp}(\omega) + \mathcal{E}^{\parallel}(\omega)]/3$ obtained from the GW calculation. Overall, CISe, and CGSe have all rather similar spectra. The high-frequency dielectric constant \mathcal{E}_{∞} depends on the energy gap E_g , and materials with large gap have a small dielectric constant [53]. Permission to use this figure has been obtained from the relevant journal.

The high-frequency dielectric constants \mathcal{E}_{∞} are presented in Table 2 in terms of transverse (\perp) and longitudinal (\parallel) components with respect to the crystalline c -axis, in comparison with earlier calculated [56] and experimental results [57,58]. The GW dielectric constants support EV+QP results for CISe and CGSe. Approximately, all the three theoretical approaches tabulated in Table 2 give the same size order of dielectric constants. The difference between $\mathcal{E}_{\infty}^{\perp}$ and $\mathcal{E}_{\infty}^{\parallel}$ demonstrates the existence of an anisotropy in the dielectric functions which is induced by the anisotropy of the crystalline structures. The stannite structure shows stronger anisotropy $\mathcal{E}_{\infty}^{\perp}/\mathcal{E}_{\infty}^{\parallel} < 1$ compared with the corresponding kesterite structure.

In Fig. 3 the GW absorption coefficients are displayed. CIGSe has larger optical absorption coefficients than CGSe in the energy range below 2.5 eV. However, materials with absorption starting from 1.5 eV (e.g., CGSe) should be more absorbing materials in solar cells. The GW results demonstrate that the absorption peak of CZTS in energy range of the visible spectrum (1.8–3.1 eV) is a beneficial property for photovoltaic applications [33].

Table 2. The high-frequency dielectric constant $\epsilon_{\infty} = \epsilon_1(0)$ is determined by excluding the electron–phonon interaction. We also present the dielectric function at $\epsilon_1(\omega=E_g/2)$ in the brackets. The transverse (\perp) and longitudinal (\parallel) components refer to the crystalline c-axis.

	ch-CIGSe	ch-CGSe	ke-CZTS	Ref.
$\epsilon_{\infty}^{\perp}$	HSE	8.18 (8.29)	7.31 (7.45)	[23]
	GW	8.26 (8.37)	8.51 (8.72)	[53]
	EV+QPa	8.2	7.6	[56]
	Expt.b	7.8, 6.86	5.13	[57,58]
$\epsilon_{\infty}^{\parallel}$	HSE	7.62 (7.69)	7.25 (7.39)	[53]
	GW	7.83 (7.92)	8.42 (8.64)	[33]
	EV+QPa	7.8	7.5	[56]
	Expt.b	7.8, 6.0	4.2	[57,58]

a Refs. [56]: a GGA potential plus a quasi-particle correction of the band gap.

b Refs. [57] and [58]: experimental results.

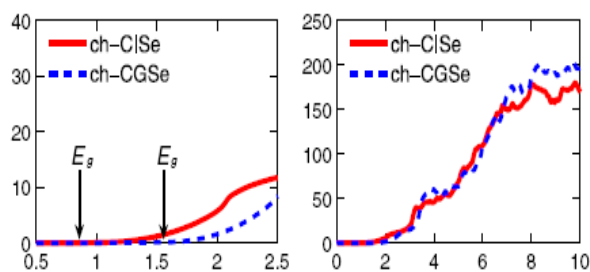


Figure 3. The optical absorption coefficient $\alpha(\omega)$ is obtained directly from the GW dielectric functions in scheme 3 using Eq. (3). We show both the absorption close to the visible spectrum (left panels) and in a broader energy region (right panels) [53]. Permission to use this figure has been obtained from the relevant journal.

6 Cell materials, configuration and fabrication procedure

The active materials of CIGS solar cells are composed of direct band gap tetrahedrally bonded compound-element semiconductors having a chalcopyrite crystal structure. Figure 4 shows the typical structure of a CIGS solar cell, indicating some commonly used materials for the different layers. A more detailed description is available elsewhere [59–62]. The most commonly used substrate is rigid, 3–4 mm thick soda-lime glass (SLG), as it is thermally stable, chemically inert, has a similar thermal expansion coefficient as the absorber. It also has a smooth surface, insulating properties suitable for monolithic interconnection and can supply alkali elements for high efficient cells (see section “Alkali post deposition treatment of CIGS layer”). However a significant amount of work has also been done for CIGS on flexible substrates such as metal foils, ceramics and polymer films, as discussed in more detail elsewhere [60].

The preferred back contact consists of sputtered molybdenum, serving as a quasi-ohmic contact with the absorber by formation of a MoSe_2 intermediate layer during absorber growth. The p-type CIGS absorber can be grown by co-evaporation processes, with selenization followed by sulfurization of precursors deposited by sputtering, electrodeposition, or printing. While co-evaporation led to the highest efficiencies for a long time [61–63], the largest commercial manufacturer and current world record holder Solar Frontier is using a sputtered precursor with subsequent selenization and sulfurization which reported a record efficiency of 22.3% [64,66]. Various CIGS compositions are used, mainly aiming at tuning the material band gap (In-Ga ratio, Se-S ratio), as well as its bulk and surface electronic properties. Among others, the introduction of a band gap grading and the presence of alkali elements are two key features that have fueled the development of higher efficiencies in recent years.

Generally, CIGS solar cells are grown in a substrate configuration. This configuration provides the highest efficiency owing to favorable process conditions and material compatibility but requires an additional encapsulation layer and/or glass to protect the cell surface. This covering glass, in contrast, is not required

for the cells grown in the superstrate configuration. CIS-based superstrate solar cells were investigated by Duchemin et al. [67] using spray pyrolysis deposition, but the efficiencies did not exceed 5%. CdS/CIGS superstrate cells do not provide the desirable interdiffusion of Cd into CIS (or CIGS) during high temperatures required for absorber deposition on CdS buffer layers [68].

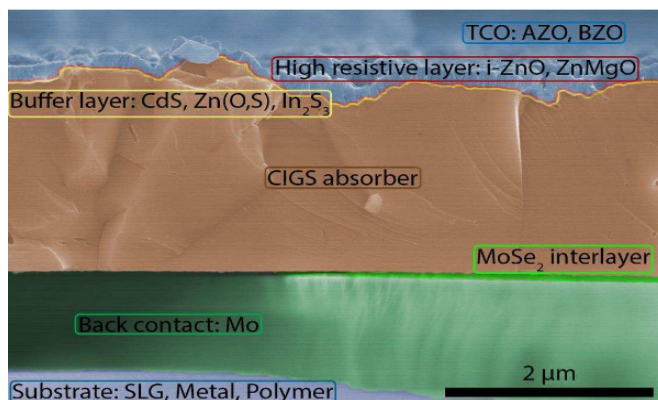


Figure 4. Schematic diagram of a typical CIGS solar cell, with examples of the most commonly used materials [62]. Permission to use this figure has been obtained from the relevant publication.

The main reason for this low efficiency in CdS/CIGS superstrate cells is the undesirable interdiffusion of Cd in to CIS (or CIGS) during the elevated temperatures required for absorber deposition on CdS buffer layers [68]. To overcome this problem of interdiffusion more stable buffer materials and low-temperature deposition processes such as electrodeposition (ED), low-substrate temperature coevaporation, and screen printing were investigated. Nakada and Mise [69] achieved a breakthrough by replacing CdS with undoped ZnO and coevaporating Na_xSe during CIGS deposition. With the additional introduction of composition grading in absorber layer, 12.8% efficiency cells were developed [70].

Numerous simulation and experimental studies have been performed in the photovoltaic field to obtain high conversion efficiency and to increase the stability and durability of the technology. The evolution from 6% efficient crystalline silicon (c-Si) cell is reached to 25.0% [69]. The emergence of new materials, and the new concept boost the efficiency up to 44.7 % for multi-junction (tandem four junction) solar cell [71]. For chalcopyrite thin-film solar cells, in CIGS the experimental and simulation results for different combination have been compared in a recent work

[72]. The efficiency for CIGS has obtained an efficiency of 20.8 % for 1 sun but it is 22.8% for concentrated solar cell applications [73].

The CIGS film consists of a p-CIGS absorber layer with combination of n-CdS layer and ZnO window layer. The band gap here is a function of Gallium and can be varied from 1.0 – 1.67 eV, that would cause the effect in the variation of other solar cell parameters [74]. Simulation results giving efficiencies above 25% are also published. Though its efficiency is high but still it is difficult to commercialize due to the availability of resources in addition to particularly rare metals, Indium (In) and gallium (Ga), that adds to the costs of the CIGS based technology [75].

Addition of alkali elements, especially Na, has long been subject of studies in the chalcopyrite thin film community, due to the beneficial impact on the electronic properties of the absorber and solar cells. If not diffusing directly from the glass substrate during the absorber deposition at elevated temperatures [76], similar beneficial effect on the bulk electronic properties were observed when adding them in a controlled manner prior, during, or after CIGS growth [77]. Whereas Na long showed the most beneficial effect, the controlled addition of KF in a post-deposition treatment (PDT) yielded a significant improvement in efficiency up to a world record efficiency of 20.4% [63]. Such a PDT treatment was originally found to be the most beneficial method to add Na onto CIGS grown at low-temperature on plastic substrates [78], because it allows separating the influence of Na on CIGS film growth from its beneficial effect on electronic properties.

While it was found that Na PDT mainly modifies the bulk electronic properties of the CIGS layer, with no discernible surface modification, addition of KF in a similar PDT treatment leads to a significant alteration of the CIGS surface composition, namely Cu and Ga depletion. Furthermore, a decrease in Na content for samples treated with K is also systematically observed [63, 79], possibly based on an ion exchange mechanism. The modified CIGS surface has strong implications on the interface formation and growth of subsequent layers, especially when grown by chemical bath methods [63, 64]. A review of the impact of addition of KF after the growth of CIGS is presented in ref. [63]. Strengthened by several consecutive world

records for the CIGS technology when applying a process based on alkali-addition after CIGS growth [63,64], these findings shed new light on the importance of considering the alkali addition process together with alkali type and their combination and the effects on both bulk as well as surface/interface properties of CIGS and solar cells. Whether the effect of KF PDT is a direct electronic effect due to the modified surface composition of the CIGS layer or whether it indirectly affects the junction quality by modifying the interface properties during buffer layer deposition is still under discussion. Influence on the bulk properties are also to be considered and cannot be excluded from the overall effects on solar cell efficiency [80].

CIGS thin film technology has been mostly developed on glass substrates, and for a long time CIGS solar cells deposited on flexible substrates such as plastic films or metal foils could not reach similar efficiencies. Limitations due to impurity diffusions or the need for lower growth temperatures imposed by the choice of the substrate were reasons for such efficiency gap. Recent developments [80] however showed that those challenges can be overcome, and is best exemplified with an efficiency above 20% achieved on polyimide (PI) foil. Deposition on a flexible substrate has advantages not only for manufacturing (large area roll-to-roll deposition is possible), but opens up a whole new field for solar module designs and applications. Especially, flexible and lightweight CIGS solar modules enable novel applications and concepts for solar electricity generation. Flexibility in shape, power rating, and form factor are some of the advantages that allow clear differentiation from traditional rigid and heavy PV technologies, opening the doors to BIPV and TIPV markets. Beside full flexible solar modules, BIPV solutions can be provided by laminating lightweight solar modules directly onto metallic building elements. Significant reduction of BOS, transport and installation cost can be expected compared to conventional glass-glass technologies.

The Gallium concentration was changed and the effect of different parameters were observed in the CIGS thin film solar cell; the summary of results were tabulated in Table 4. The open circuit voltage (Voc) and the band gap of the CIGS layer increases as the gallium (Ga) content increases. The short circuit current

represented by (J_{SC}) decreases as the band gap increases due to the recombination of carriers, thus it has the reverse effect than Voc. Similarly, the Fill-Factor (FF) increases up to 50%, moreover, due to an increase in Ga contents beyond 50% which causes decrease in FF, the same phenomenon is also observed in the case of external quantum efficiency η (%). By increasing η up to 66% of Ga contents, further increase of Ga causes decrease in η [73]. The summary of result obtained by using scaps (solar cell capacitance simulator) are demonstrated in Table 3 [81].

Table 3. Photovoltaic parameters for CIGS solar cells with different Ga content [81].

Ga content	Method	Voc (V)	Jsc (mA/cm2)	FF (%)	eta (%)
0.00	scaps	0.5282	48.3933	79.75	20.38
0.31	scaps	0.6747	46.2690	82.37	25.71
0.45	scaps	0.7733	45.7018	83.43	29.48
0.66	scaps	0.8768	42.0037	84.04	30.0
1.00	scaps	0.8807	38.5823	83.59	28.40

Eta: Estimated Time Of Arrival

7 Results and discussion

To date, CIGS cells have comparable efficiencies to the polycrystalline Si solar cell. These cells could be deposited on both rigid glass substrates or flexible substrates and it was observed that the efficiency is higher when the cell is deposited on rigid substrates, i.e., soda lime glass substrate due to the positive effect of Na. In Fig. 6, two separate efficiency lines can be seen for the CIGS solar cell, one is based on a rigid substrate (R) and another is for a flexible substrate (F). Notice that the efficiency of CIGS cells deposited on a flexible substrate gradually progresses towards the cell deposited on a rigid substrate. It is already mentioned that the manufacturing cost of this cell is lower than that of crystalline solar cell but scarcity of In and Ga is still the vital challenge. Most of the buffer layer of CIGS contain toxic cadmium content is another bottleneck that limits the potential of this solar cell. Similar to (CIGS), the CdTe is one of the most investigated materials among the second generation thin film solar cells. However, there are some issues regarding the cost of raw materials. Toxicity. CZTS is another promising thin film solar cell which is anatomically similar structured like CIGS. That is, fabrication procedure of different layers such as buffer, window, and TCO layer of CZTS is also similar to the CIGS cell. Beside these, DSSC cells are unique among

the TFSCs in terms of cell structure and constituent materials. This solar cell is the promising likewise of CZTS because of earth abundance of its constituent elements and their environmentally benign nature. Therefore, CZTS is one of the most desirable and adorable PV materials despite its' reported efficiency is lower compared to CIGS and CdTe. A summary of the five TFSCs research works has been presented in Table 6 as a comparative data for structural, optical, and electrical properties, material availability, toxicity, stability, and highest efficiency.

Thin-film solar cells cover around 4.5% of worldwide photovoltaic market share where a-Si:H covered 0.3%, CIGS covered 1.9%, and CdTe covered 2.3% of the market share in 2018. Both CIGS and CdTe solar cell enjoy the advantage of their matured fabrication technology, presently their efficiency is comparable with multicrystalline silicon solar cells but their cost is comparatively lower than this type of Si solar cells. Both of these cells can be deposited on either rigid glass substrates or flexible glass substrates, both can be configured in either superstrate or substrate stacks. However, both of them use scarce and toxic materials which are the major limitations of these cells. Again, efficiency of a-Si:H is relatively lower in comparison with CIGS and CdTe and reduced after a certain time. In contrast, CZTS and DSSC are most promising solar cells in the thin film family, because of raw materials' abundance, environmentally benign nature, low- cost as well as easy to synthesis and processing techniques. These solar cells are still in the research and development phase, so its market share is not mentionable but their progress is slowly moving forward for commercializing in global PV markets.

7 Conclusions

In this article, remarkable development, constituent cell materials, fabrication procedures of major types of thin film solar cells have been reviewed. Modification of the layers in cell configuration from the primitive cell to the state-of-the-art cell has been discussed with possible inclusion of new raw materials and fabrication processes. Limitations for which performance of these cells that are still below market-dominant silicon solar cell have also been discussed. The record efficiency, to date, for a-Si:H, CIGS, CZTS, CdTe, and Dye sensitized solar cell (DSSC) is 13.4%, 22.5%, 12.6%, 22.1%, and 15% respectively. Among them, CZTS and

DSSC are still in research and development phase while the efficiencies of CIGS and CdTe solar cell are comparable with the c-Si solar cells efficiency. However the manufacturing process of c-Si cell poses more challenges than thin film solar cells. So, thin film PV technologies are believed to be the most promising for terawatt scale PV deployment among the existing renewable energy technologies that could mitigate present as well as future energy crisis. Therefore, extensive research efforts must be given to overcome the critical issues related to the TFSCs for popularization as well as for viable commercialization.

References

- [1] M. Jamiaty, B. Khoshnevisana, M. Mohammadib, "Second- and third-order elastic constants of kesterite CZTS and its electronic and optical properties under various strain rates." *Energy Sources, Part A: Recovery, Utilization, and Environmental Effects*, **40** (2018) 977.
- [2] A. Kowsar, S. F. U. Farhad, "High Efficiency Four Junction III-V Bismide Concentrator Solar Cell: Design, Theory, and Simulation." *International Journal of Renewable Energy Research (IJRER)*, **8** (2018) 17621769.
- [3] D. Jeyakumar Ramanujama, et al., "Flexible CIGS, CdTe and a-Si:H based thin film solar cells: A review." *Progress in Materials Science*, **110** (2020) 100619.
- [4] R. Light, "Trapping in thin silicon solar cells: A review on fundamentals and technologies." *Progress in photovoltaics*, **7** (2021) 3440.
- [5] C. Romain, et al., "Advanced alkali treatments for high-efficiency Cu(In,Ga)Se₂ solar cells on flexible substrates." *Advanced Energy Materials*, **9** (2019) 1900408.
- [6] A. Bosio, S. Pasini, N. Romeo, "The History of Photovoltaics with Emphasis on CdTe Solar Cells and Modules." *Advances in Thin Films for Photovoltaic*, **10** (2020) 344.
- [7] Y. Wu, et al., "Synthesis and photovoltaic application of copper (I) sulfide nanocrystals."

- Nano letters, **8** (2008) 2551.
- [8] M. A. Green, et al., "Solar cell efficiency tables (version 52)." *Progress in Photovoltaics: Research and Applications*, **26** (2018) 427.
- [9] A. Kowsar, et al., "Progress in Major Thin-film Solar Cells: Growth Technologies, Layer Materials and Efficiencies." *International Journal of renewable energy research*, **9** (2019) 579.
- [10] U. Rau, H. W. Schock, "Cu(In,Ga)Se₂ solar cells," in *Clean Electricity from Photovoltaics*, ed: World Scientific, (2001) 277-345.
- [11] S. Wagner, J. Shay, P. Migliorato, H. Kasper, "CuInSe₂/CdS heterojunction photovoltaic detectors." *Applied Physics Letters*, **25** (1974) 434.
- [12] L. L. Kazmerski, F. R. White, G. K. Morgan, "Thin-film CuInSe₂/CdS heterojunction solar cells." *Applied Physics Letters*, **29** (1976) 268.
- [13] R. Mickelsen, W. Chen, "Development of a 9.4% efficient thin-film CuInSe₂/CdS solar cell." in *15th photovoltaic specialists conference*, (1981) 800.
- [14] J. Tuttle, et al., "Accelerated publication 17.1% efficient Cu(In,Ga) Se₂- based thin- film solar cell." *Progress in Photovoltaics: Research and Applications*, **3** (1995) 235.
- [15] M. A. Contreras, et al., "Progress toward 20% efficiency in Cu (In, Ga) Se₂ polycrystalline thin- film solar cells." *Progress in Photovoltaics: Research and applications*, **7** (1999) 311.
- [16] I. Repins, et al., "Characterization of 19.9%efficient CIGS absorbers." *Photovoltaic Specialists Conference, 2008. PVSC'08. 33rd IEEE*, (2008) 1-6 .
- [17] T. Satoh, et al., "Cigs solar cells on flexible stainless steel substrates," in *Photovoltaic Specialists Conference, 2000. Conference Record of the Twenty-Eighth IEEE*, (2000), 567-570 .
- [18] R. Wuerz, et al., "CIGS thin-film solar cells on steel substrates." *Thin Solid Films*, **517** (2003) 24152418.
- [19] C. Shi, et al., "Cu(In,Ga)Se₂ solar cells on stainless-steel substrates covered with ZnO diffusion barriers." *Solar Energy Materials and Solar Cells*, **93** (2009) 654.
- [20] B. M. Başol, et al., "Flexible and light weight copper indium diselenide solar cells on polyimide substrates," *Solar Energy Materials and Solar Cells*, **43** (1996) 9398.
- [21] M. Feli, F. Parandin, "A Numerical Optimization of an Efficient Double Junction InGaN/CIGS Solar Cell." *Journal of Electrical. Computer Engineering Innovations*, **6** (2018) 53.
- [22] H. Zachmann, et al., "Characterisation of Cu(In,Ga)Se₂-based thin film solar cells on polyimide." *Thin Solid Films*, **517** (2009) 2209.
- [23] B. M. Başol, et al., "Copper indium diselenide thin film solar cells fabricated on flexible foil substrates." *Solar Energy Materials and Solar Cells*, **29** (1993) 163.
- [24] M. A. Green, et al., "Solar cell efficiency tables (version 42)." *Progress in Photovoltaics: Research and Applications*, **5** (2013) 827.
- [25] Michael Powalla, et al., "Advances in Cost-Efficient Thin-Film Photovoltaics Based on Cu(In,Ga)Se₂." *Engineering*, **3** (2017) 445.
- [26] J. Parkes, R. D. Tomlinson, M. J. Hampshire, "Crystal data for CuInSe₂." *Journal of Applied Crystallography*, **6** (1973) 414.
- [27] S. C. Abrahams, J. L. Bernstein, "Piezoelectric nonlinear optic CuGaSe₂ and CdGeAs₂: Crystal structure, chalcopyrite microhardness, and sublattice distortion." *Journal of Chemical Physics*, **61** (1974) 1140.
- [28] S. Chen, X. G. Gong, S. H. Wei, "Band-structure anomalies of the chalcopyrite semiconductors CuGaX₂ versus AgGaX₂ (X=S and Se) and their alloys." *Physical Review B*, **75** (2007) 205209.

- [29] C. D. R. Ludwig, T. Gruhn, C. Felser, "Indium-Gallium Segregation in $\text{CuIn}_x\text{Ga}_{1-x}\text{Se}_2$: An Ab Initio-Based Monte Carlo Study." *Physical Review Letters*, **105** (2010) 025702.
- [30] J. Osuntokun, P. A. Ajibade, "Structural and Thermal Studies of ZnS and CdS Nanoparticles in Polymer Matrices." *Journal of Nanomaterials*, **2016** (2016) 3296071.
- [31] J. L. Shay, H. M. Kasper, L. M. Schivone, "Electronic Structure of AgInSe_2 and CuInSe_2 ." *Physical Review B*, **7** (1973) 4485.
- [32] J. L. Shay and H. M. Kasper, "Direct Observation of Cu-d Levels in I-III-VI₂ Compounds." *Physical Review Letters*, **29** (1972) 1162.
- [33] U. Rau, K. Taretto, S. Siebentritt, "Grain boundaries in $\text{Cu}(\text{In,Ga})(\text{Se,S})_2$ thin-film solar cells." *Applied Physics A*, **96** (2009) 221.
- [34] P. Palacios, et al., "Thermodynamics of the Formation of Ti- and Cr-doped CuGaS_2 Intermediate-band Photovoltaic Materials." *Journal of Physical Chemistry C*, **112** (2008) 9525.
- [35] T. D. Lee, A. Ebong, "Thin film solar technologies: a review." in 2015 12th International Conference on High-capacity Optical Networks and Enabling/Emerging Technologies (HONET), Islamabad, Pakistan, December 2015, (2015) 1.
- [36] Y. C. Wang, H. P. D. Shieh, "Double-graded bandgap in $\text{Cu}(\text{In,Ga})\text{Se}_2$ thin film solar cells by low toxicity selenization process." *Applied Physics Letters*, **105** (2014) 073901.
- [37] J. Ramanujam, U. P. Singh, "Copper indium gallium selenide based solar cells – a review." *Energy & Environmental Science*, **10**(6) (2017) 1306.
- [38] J. E. Jaffe, A. Zunger, "Electronic structure of the ternary chalcopyrite semiconductors CuAlS_2 , CuGaS_2 , CuInS_2 , CuAlSe_2 , CuGaSe_2 , and CuInSe_2 ." *Physical Review B*, **28** (1983) 5822.
- [39] S. H. Weiand, L. G. Ferreira, A. Zunger, "First-principles calculation of the order-disorder transition in chalcopyrite semiconductors." *Physical Review B*, **45** (1992) 2533.
- [40] S. H. Weiand, A. Zunger, "Band offsets at the $\text{CdS}/\text{CuInSe}_2$ heterojunction." *Applied Physics Letters*, **63** (1993) 2549.
- [41] S. H. Weiand, A. Zunger, "Band offsets and optical bowings of chalcopyrites and Zn-based II-VI alloys." *Journal of Applied Physics*, **78** (1995) 3846.
- [42] M. Gloeckler, J. R. Sites, "Guidelines for Optimization of the Absorber Layer Energy Gap for High Efficiency $\text{Cu}(\text{In,Ga})\text{Se}_2$ Solar Cells." *Journal of Physics and Chemistry of Solids*, **66** (2005) 1891.
- [43] S. B. Zhang, S. H. Weiand, A. Zunger, "Stabilization of Ternary Compounds via Ordered Arrays of Defect Pairs." *Physical Review Letters*, **78** (1997) 4059.
- [44] S. B. Zhang, S. H. Weiand, A. Zunger, H. Katayama-Yoshida, "Defect physics of the CuInSe_2 chalcopyrite semiconductor." *Physical Review B*, **57** (1998) 9642.
- [45] S. H. Weiand, S. B. Zhang, and A. Zunger, "Effects of Na on the electrical and structural properties of CuInSe_2 ." *Journal of Applied Physics*, **85** (1999) 7214.
- [46] S. H. Weiand, S.B. Zhang, and A. Zunger, "Effects of Ga addition to CuInSe_2 on its electronic, structural, and defect properties." *Applied Physics Letters*, **72** (1998) 3199.
- [47] C. H. Huang, "Effects of Ga content on $\text{Cu}(\text{In,Ga})\text{Se}_2$ solar cells studied by numerical modeling." *Journal of Physics and Chemistry of Solids*, **69** (2008) 330.
- [48] Z. A. Shukri, et al., "Preliminary photovoltaic cells with single crystal CIS substrates." *Solar Energ. Mater. and Solar Cells*, **37** (1995) 395.
- [49] M. Gloeckler, J. R. Sites, W. K. Metzger, "Grain-boundary recombination in $\text{Cu}(\text{In,Ga})\text{Se}_2$ solar cells." *Journal of Applied*

- Physics, **98** (2005) 113704.
- [50] J. M. Raulot, C. Domain, J.F. Guillemoles, "Ab initio investigation of potential indium and gallium free chalcopyrite compounds for photovoltaic application." *Journal of Physics and Chemistry of Solids*, **66** (2005) 2019.
- [51] W. N. Shafarman, S. Siebentritt and L. Stolt, *Handbook of Photovoltaic Science and Engineering*, Wiley, New York (2011).
- [52] P. Jackson, et al., "High quality baseline for high efficiency, $\text{Cu}(\text{In}_{1-x}\text{Ga}_x)\text{Se}_2$ solar cells." *Progress in Photovoltaics: Research and Applications*, **15** (2007) 507.
- [53] H. Zhao, C. Persson, "Optical properties of $\text{Cu}(\text{In,Ga})\text{Se}_2$ and $\text{Cu}_2\text{ZnSn}(\text{S,Se})_4$." *Thin Solid Films*, **519** (2011) 7508.
- [54] M. Chandramohan, S.Velumani, T. Venkatachalam, "Band structure calculations of $\text{Cu}(\text{In}_{1-x}\text{Ga}_x)\text{Se}_2$." *Journal of Materials Science and Engineering B*, **174** (2010) 200.
- [55] A. Bouich, et al., "Deposit on different back contacts: to high-quality $\text{Cu}(\text{InGa})\text{S}_2$ thin films for photovoltaic application." *Journal of Materials Science: Materials in Electronics*, **30** (2019) 20832.
- [56] C. Persson, "Electronic and optical properties of $\text{Cu}_2\text{ZnSnS}_4$ and $\text{Cu}_2\text{ZnSnSe}_4$." *Journal of Applied Physics*, **107** (2010) 053710.
- [57] T. Kawashima, et al., "Optical constants of CuGaSe_2 and CuInSe_2 ." *Journal of Applied Physics*, **84** (1998) 5202.
- [58] N. N. Syrbu, et al., "Lattice vibrations in $\text{CuIn}_{(1-x)}\text{Ga}_x\text{Se}_2$ crystals." *Journal of Physics B*, **229** (1997) 199.
- [59] F. Ghavami, A. Salehi, "High-efficiency CIGS solar cell by optimization of doping concentration thickness and energy band gap." *Modern Physics Letters B*, **34**(4) (2020) 2050053.
- [60] P. Reinhard, et al., "Review of Progress Toward 20% Efficiency Flexible CIGS Solar Cells and Manufacturing Issues of Solar Modules." *IEEE Journal of Photovoltaics*, **3** (2013) 572.
- [61] W. N. Shafarman, S. Siebentritt, L. Stolt, " $\text{Cu}(\text{InGa})\text{Se}_2$ solar cells in: Luque A, Hegedus S," *Handbook of photovoltaic science and engineering*, England: John Wiley & Sons Ltd; pp. 546-599 (2010).
- [62] R. Scheer, H. W. Schock, " *Chalcogenide Photovoltaics: Physics, Technologies and Thin Film Devices*." John Wiley & Sons Ltd; pp. 154-172 (2011).
- [63] A. Chirilă, et al., " Potassium-induced surface modification of $\text{Cu}(\text{InGa})\text{S}_2$ thin films for high efficiency solar cells." *Nature Materials*, **12** (2013) 1107.
- [64] T. Feurer, et al., "Progress in Thin Film CIGS Photovoltaics – R&D, Manufacturing and Applications." *Progress in Photovoltaics*, **25** (2017) 645.
- [65] K. Kushiya, "CIS-based thin-film PV technology in solar frontier K.K " *Solar Energy Materials and Solar Cells*, **122** (2014) 309.
- [66] " Solar Frontier Achieves World Record Thin-Film Solar Cell Efficiency : 22.3%." *Solar Frontier company webpage* December 8, 2015 Accessed April 25, 2016. <http://www.solar-frontier.com/eng/news/2015/C051171.html>.
- [67] S. Duchemin et al., in: *Photovoltaic Solar Energy. Proc. 8th European Conference*, pp. 1038- 1042, Florence, Italy, (1988).
- [68] T. Nakada et al., *Photovoltaic Energy Conversion. IEEE First World Conference*, pp. 95-98, Hawaii, USA (1994).
- [69] M. A. Green, "The path to 25% silicon solar cell efficiency: History of silicon cell evolution." *Progr. in Photovolt.: Research and Applications*, **17** (2009) 183.
- [70] T. Nakada, T.Mise, "High-efficiency superstrate type cigs thin film solar cells with graded bandgap absorber layers." *Proceedings of the 17th European Photovoltaic Solar Energy*

- Conference, pp. 1027–1030, Munich, Germany (2001).
- [71] F. Dimroth, et al., "Wafer bonded four-junction GaInP/GaAs//GaInAsP/GaInAs concentrator solar cells with 44.7% efficiency." *Progr. in Photovolt.: Research and Applications*, **22** (2014) 277.
- [72] S. Keshmiri, H. S. Sharbati, "Model for increased efficiency of CIGS solar cells by a stepped distribution of carrier density and Ga in the absorber layer." *Science China: Physics, Mechanics and Astronomy*, **56** (2013) 1533.
- [73] P. Jackson, et al., "Compositional investigation of potassium doped Cu(In,Ga)Se₂ solar cells with efficiencies up to 20.8%." *Physica Status Solidi (RRL)-Rapid Research Letters*, **8** (2014) 219.
- [74] H. Ullah, B. Mari, H. N. Cui, "Investigation on the Effect of Gallium on the Efficiency of CIGS Solar Cells through Dedicated Software." *Applied Mechanics and Materials*, **448** (2014) 1497.
- [75] M. Tawheed Kibria, et al., "A Review: Comparative studies on different generation solar cells technology." *Proceedings of 5th International Conference on Environmental Aspects of Bangladesh [ICEAB 2014]*.
- [76] J. Hedstrom, et al., "Zno/Cds/Cu(in,Ga)Se₂ Thin-Film Solar-Cells with Improved Performance." *Conference Record of the Twenty Third Ieee Photovoltaic Specialists*, (1993) 364.
- [77] D. Rudmann, et al., "Sodium incorporation strategies for CIGS growth at different temperatures." *Thin Solid Films*, **480** (2005) 55.
- [78] D. Rudmann, et al., "Efficiency enhancement of Cu(In,Ga)Se₂ solar cells due to post deposition Na incorporation." *Applied Physics Letters*, **84** (2004) 1129.
- [79] P. Reinhard, et al., "Features of KF and NaF Postdeposition Treatments of Cu(In,Ga)Se₂ Absorbers for High Efficiency Thin Film Solar Cells." *Chemistry of Materials*, **27** (2015) 5755.
- [80] L. M. Mansfield, et al., "Enhanced Performance in Cu(In,Ga)Se Solar Cells Fabricated by the Two-Step Selenization Process With a Potassium Fluoride Postdeposition Treatment." *IEEE Journal of Photovoltaics*, **4** (2014) 1650.
- [81] H. Ullah, B. Marí, L. M. Sánchez Ruiz, "Comparative analysis of CIGS thin film and Multilayer Solar cells." *Proc.Int. Conf. Engineering Education and research, Riga, Latviya, ICEE/ICIT* (2014) 103.



Thermal entanglement in spin chain with XX, XY, and XZ Heisenberg interactions

Scientific research paper

Maryam Mahmoudi^{1*}, Mohammad Reza Soltani², and Arezu Jahanshir³

¹*Department of Physics, University of Guilan, 41335-1914, Rasht, Iran*

²*Department of Physics, Yadegar-e-Imam Khomeini (RAH) Shahre Rey Branch, Islamic Azad University, Tehran, Iran*

³*Department of Physics and Engineering Sciences, Imam Khomeini International University, Buein Zahra Higher*

Education Centre of Engineering and Technology, Iran

ARTICLE INFO

Article history:

Received 14 August 2021

Revised 2 November 2021

Accepted 2 November 2021

Available online 8 December 2021

Keywords:

Quantum entanglement

Heisenberg interaction

Dzyaloshinskii-Moriya interaction

External magnetic field

Spin chain

ABSTRACT

In this paper, the quantum correlation of a 2-spin Heisenberg model system with Dzyaloshinskii-Moriya interaction in presence of an external magnetic field is studied. Three types of exchange interactions, namely, XX, XY, and XZ are considered. The thermal entanglement of these systems is investigated under the change of the external magnetic field. We found that the temperature behavior of the three models is similar. Moreover, we study the magnetic field dependence of negativity in three models and obtain the critical magnetic field.

1 Introduction

Entanglement is a basic characteristic of quantum physics which has attracted attention in recent decades as a non-classical correlation in the quantum systems [1,2,3]. Quantum entanglement has an important role in various fields of quantum information, quantum computation, quantum teleportation, quantum communication, and superdense coding [4,5,6]. In the solid state, the Heisenberg spin systems have been devoted as a suitable system to study the entanglement properties of the quantum systems. Spins have been recognized as candidates for quantum solid state research [7,8]. Therefore, many studies have been performed to understand the behavior of the quantum

entanglement in spin systems. An important interaction between spins in quantum systems is all the various kinds of Heisenberg models such as XX, XY, XZ, XXZ, etc [9,10,11,12,13]. The Heisenberg model describes the interaction of qubits not only in solid state systems, but also in quantum dots, optical lattice, and nuclear spin [14,15,16]. In recent years, the thermal entanglement of the 2-qubit systems with spin-spin interaction and spin-orbit interaction has been studied in the literature [17,18,19]. Vidal et al introduced the negativity as a measure of bipartite entanglement [20].

In the Heisenberg model, the order parameter is a vector that rotates in the three-dimensional space and

*Corresponding author.

Email address: Jahanshir@bzeng.ikiu.ac.ir

DOI: 10.22051/jitl.2022.37268.1059

possesses symmetry in the absence of the magnetic field. In the XY Heisenberg model, spins are rotated in plane, so the order parameter has two components. This model has been found in super-fluids such as ⁴He. Basically, the Heisenberg model- whether isotropic or anisotropic- is often used to study the critical point and phase transition in magnet systems. In fact, the Heisenberg interaction is a more realistic model to study magnet systems. Effect of anisotropy in the exchange interaction between neighbor spins is significant, since according to many studies, the anisotropic property of the Heisenberg interaction can preserve and even increase the entanglement in the quantum spin systems. Motivated by these, in the present study, we compare the thermal entanglement behavior of the 2-qubit systems in isotropic and anisotropic Heisenberg models. We study the XX, XY, and XZ Heisenberg model with added DM interaction under the external magnetic field. The paper is organized as follows: in section II, we briefly give the Hamiltonian of the model to define the negativity. In section III, we investigate and discuss the results. Finally, section IV contains the conclusion of the research.

2 Method and results

The general Hamiltonian of the two-spin Heisenberg model with antisymmetric DM interaction and in the presence of the magnetic field is written as:

$$H = J_x S_1^x S_2^x + J_y S_1^y S_2^y + J_z S_1^z S_2^z + D(S_1^x S_2^y - S_1^y S_2^x) + h(S_1^z + S_2^z), \quad (1)$$

where $J_x \cdot J_y \cdot J_z$ are the exchange coefficients in three directions of x, y, z. D is the Dzisloshinski-Moriya interaction parameter along the z direction, S is the spin operator, and h is the external magnetic field. We limit our study to a two- dimensional Heisenberg interaction. To study the effect of the Heisenberg interaction on the thermal entanglement of a 2-qubit spin system, we consider three different kinds of the XX, XY, and XZ Heisenberg interaction. First, we investigate the XX Heisenberg model.

2.1 XX-DM-hz

The 2- qubit isotropic Heisenberg model subjected to the magnetic field and DM interaction is modeled by the Hamiltonian:

$$H = J(S_1^x S_2^x + S_1^y S_2^y) + D(S_1^x S_2^y - S_1^y S_2^x) + h(S_1^z + S_2^z). \quad (2)$$

Here, $J_x = J_y = J$. To determine the energy levels of the model, we should express the matrix of the Hamiltonian in the standard basis of $|\downarrow\downarrow\rangle, |\downarrow\uparrow\rangle, |\uparrow\downarrow\rangle, |\uparrow\uparrow\rangle$:

$$H = \begin{bmatrix} 2h & 0 & 0 & J \\ 0 & 0 & J + 2iD & 0 \\ 0 & J - 2iD & 0 & 0 \\ J & 0 & 0 & -2h \end{bmatrix}. \quad (3)$$

Then, we diagnosis the Hamiltonian matrix and calculate the eigen-values of the matrix. The eigen - values of this Hamiltonian are:

$$E1 = -E2 = \frac{1}{2}\sqrt{J^2 + D^2},$$

$$E3 - E4 = -\frac{h}{2}. \quad (4)$$

To calculate the quantum entanglement, we use the negativity measure. The negativity can be obtained using the density operator $\rho(T) = \exp(-\beta H) / Z$ where $Z = Tr(\exp(-\beta H))$ is the partition function and $\beta = 1/kT$. For simplicity, we take $k=1$. By selecting the appropriate set of the orthonormal product basis states for the density operator, the partial transpose is defined by its matrix elements

$$\rho_{m\mu, n\nu}^{T_1} = \langle v_m v_\mu | \rho | v_n v_\nu \rangle = \rho_{m\nu, n\mu}. \quad (5)$$

The negativity of a state ρ is by definition as

$$N = \sum_i |\mu_i|, \quad (6)$$

where μ_i is the negative eigenvalue of the partial transpose density matrix ρ^{T_1} . Thus, the negativity can be written as:

$$N = \frac{\|\rho^T\| - 1}{2}. \quad (7)$$

The temperature dependence of the system is shown in Fig. 1. As seen in this figure, raising the temperature reduces the negativity because by increasing the

temperature, the excited states involve the state of the system and then the state of the system converts into a mixed state that decreases the negativity. According to the figure, there is a critical temperature in which the negativity reaches zero. It is important to postpone the critical temperature. This results in protecting the entanglement of the system against the gradual or sudden death.

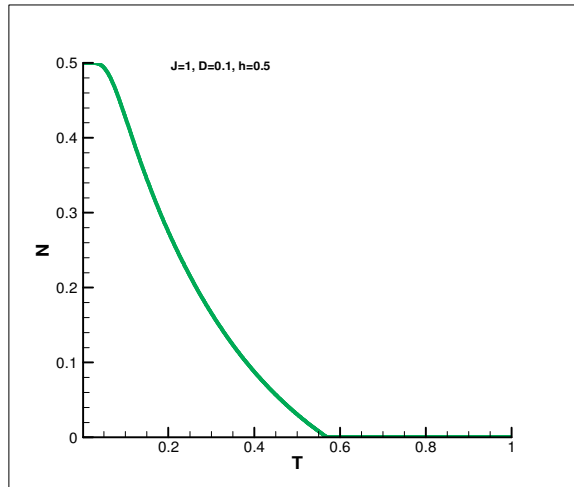


Figure 1. Temperature dependence of the XX-DM-h model.

The DM interaction can help the entanglement to maintain non- zero until higher temperatures. Figure 2 shows that raising the DM interaction increases the critical temperature and then is a positive factor to avoid the system from the disentanglement in a finite temperature. One can conclude that in contrast to the destructive role of temperature, DM interaction has an effective and reinforcing role for preserving the entanglement. Although, in very low temperatures, DM interaction cannot influence the thermal entanglement. It seems in temperatures near zero, the entanglement is independent of the DM interaction.

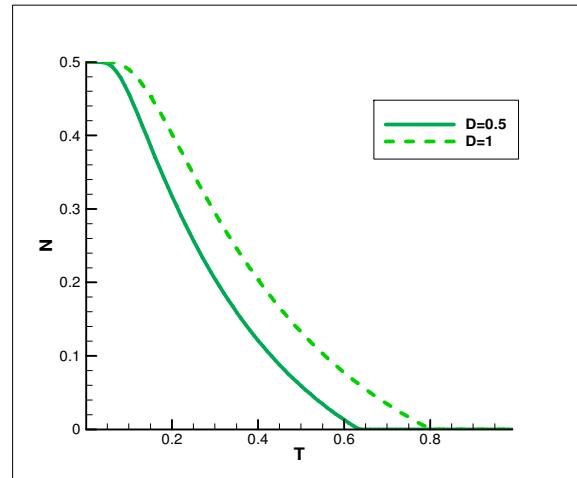


Figure 2. Thermal entanglement of the system in two different DM interactions. $J=1$, $h=0.5$.

Figure 3 shows the effect of the magnetic field on the negativity. As seen in this figure, there is a critical magnetic field above which the entanglement of the system disappears. Our study shows that this critical point depends on the exchange interaction parameter (J). In fact, a competition between the exchange interaction and the magnetic field leads to a critical point. In magnetic field values lower than J , the Heisenberg interaction entangles the system, but by increasing the magnetic field, the destructive effect of h disentangles the system.

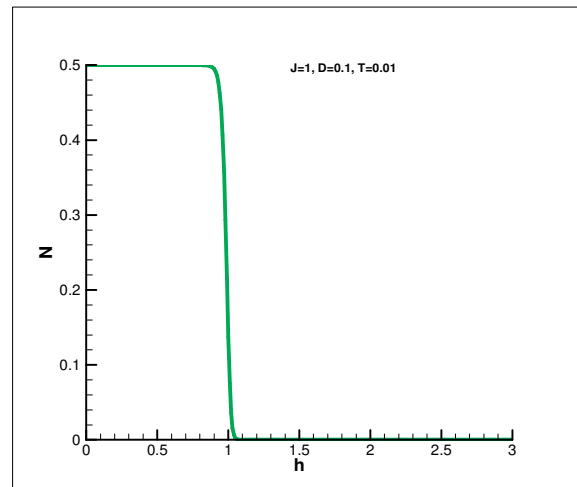


Figure 3. Magnetic field dependence of the negativity in the XX-DM-h model.

2.2. XY-DM-h

The second model that we study is the anisotropic Heisenberg model with added DM interaction and under the external magnetic field. The Hamiltonian is:

$$H = J_x S_1^x S_2^x + J_y S_1^y S_2^y + D(S_1^x S_2^y - S_1^y S_2^x) + h(S_1^z + S_2^z). \quad (8)$$

The Hamiltonian matrix is expressed as:

$$H = \begin{bmatrix} h & 0 & 0 & \frac{J_x - J_y}{4} \\ 0 & 0 & \frac{J_x + J_y + 2iD}{4} & 0 \\ 0 & \frac{J_x + J_y - 2iD}{4} & 0 & 0 \\ \frac{J_x - J_y}{4} & 0 & 0 & -h \end{bmatrix}, \quad (9)$$

The eigen -values of this matrix are:

$$E1 = -E2 = \frac{1}{4} \sqrt{(J_x + J_y)^2 + 4D^2},$$

$$E3 = -E4 = \frac{1}{4} \sqrt{(J_x - J_y)^2 + 16h^2}, \quad (10)$$

Figure 4 shows the thermal entanglement of this model. Similar to the previous model, raising the temperature reduces the negativity of the system wher in high temperatures the entanglement of the system disappears. There is a difference between the thermal behavior of the entanglement in the XX Heisenberg and XY Heisenberg models. The critical temperature in the XY model is higher than the XX model. It seems that the anisotropy parameter leads to a higher critical temperature. Thus, the anisotropy of the Heisenberg interaction can preserve entanglement against the destructive role of the temperature.

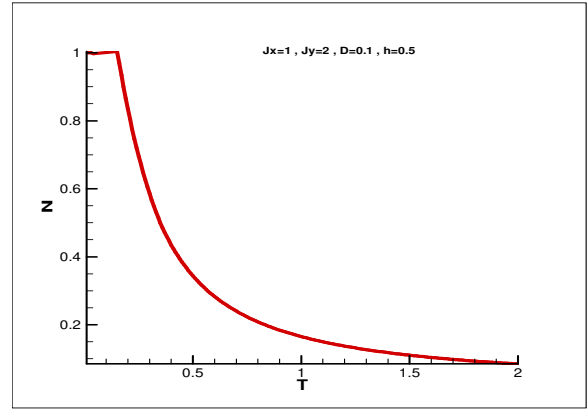


Figure 4- temperature dependence of the XY-DM-h model.

Figure 5 shows the magnetic field dependence of the negativity in the XY Heisenberg model. As seen in the figure, there is a critical magnetic field in which the entanglement of the system becomes zero. Although, below the h_c value, the entanglement of the system is independent of the magnetic field, above the h_c value, the entanglement of the system shows a descending behavior in terms of magnetic field. We can conclude that compared to the isotropic Heisenberg model, the anisotropy in the exchange interaction compensates the destructive effect of the magnetic field.

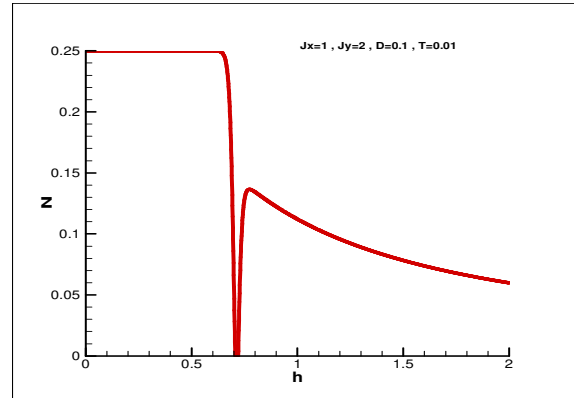


Figure 5. magnetic field dependence of the negativity in the XY-DM-h model.

2.3. XZ-DM-h

The second model that we study is the anisotropic Heisenberg model with added DM interaction under the external magnetic field. The Hamiltonian is:

$$H = J_x S_1^x S_2^x + J_y S_1^z S_2^z + D(S_1^x S_2^y - S_1^y S_2^x) + h(S_1^z + S_2^z), \quad (11)$$

and the Hamiltonian matrix can be written as:

$$H = \begin{bmatrix} J_z + 2h & 0 & 0 & J_x \\ 0 & -J_z & J_x + 2iD & 0 \\ 0 & J_x - 2iD & -J_z & 0 \\ J_x & 0 & 0 & J_z - 2h \end{bmatrix}. \quad (12)$$

The eigen-values of this Hamiltonian are:

$$\begin{aligned} E1 &= \frac{-1}{4}(J_z + X) \\ E2 &= \frac{-1}{4}(J_z - X) \\ E3 &= \frac{-1}{4}(J_z + Y) \\ E4 &= \frac{-1}{4}(J_z - Y), \end{aligned} \quad (13)$$

where

$$X = \sqrt{J_x^2 + 4D^2}, \quad Y = \sqrt{J_x^2 + 16h^2}.$$

Figure 6 shows the thermal entanglement of this model. Similar to the previous models, at high temperatures, the entanglement of the system in the XZ-DM-h model disappears. But, the critical temperature of this model is different from the two previous models.

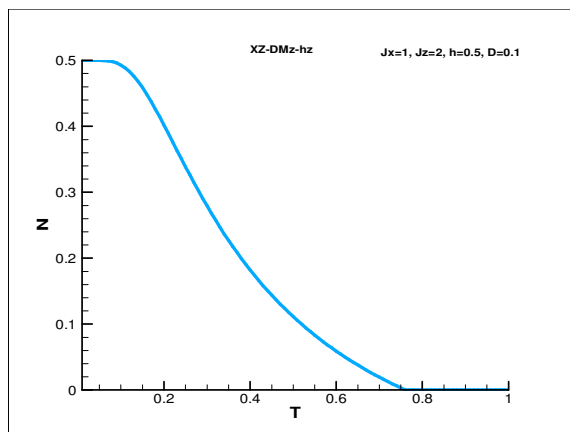


Figure 6. Temperature dependence of the negativity in the XZ-DM-h model.

Figure 7 shows the magnetic field dependence of the entanglement in the XZ-DM-h model. The behavior of the negativity in this model is similar to the previous model, but the critical magnetic field is greater in this model than the XY-DM-h model. It seems that the direction of the anisotropy affects the value of the critical magnetic field. In other words, the anisotropy in the h direction can delay the critical point.

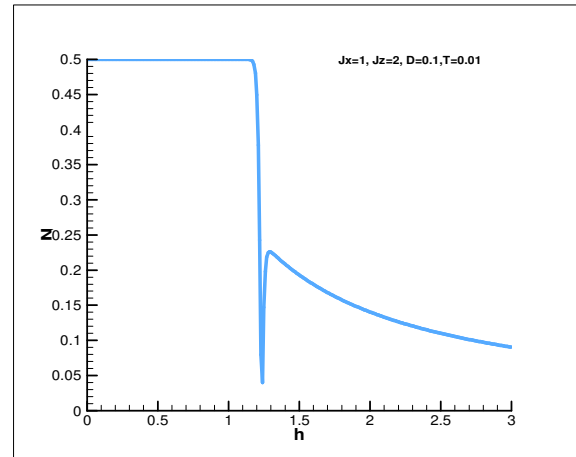


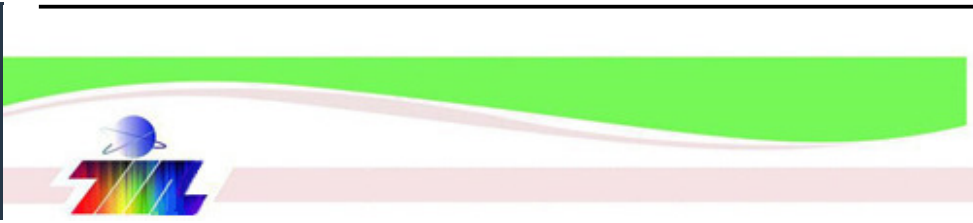
Figure 7. Magnetic field dependence of the negativity in the XZ-DM-h model.

4 Conclusions

In this study, we investigated the effect of different Heisenberg interactions on the negativity of the two- spin system. Three types of the exchange interaction, XX, XY, and XZ are considered. The thermal entanglement of these systems is investigated under the change of the external magnetic field. We found that the temperature behavior of the system is similar, although the critical temperature is different. Also, we investigated the effect of the external magnetic field on the negativity of the system. We observed that all three models have a critical magnetic field in which the negativity of the system becomes zero. In fact, the anisotropic Heisenberg interaction can affect the critical temperature and critical magnetic field of the two- spin systems.

References

- [1] E. Schrodinger, "Mathematical proceedings of the Cambridge philosophical society." *Mathematical Proceedings of the Cambridge Philosophical Society*, **31** (1935) 555.
- [2] Z. Xi, Y. Li, and H. Fan, "Quantum coherence and correlations in quantum system." *Scientific Reports*, **5** (2015) 10922.
- [3] L. Amico, R. Fazio, A. Osterloh, and V. Vedral, "Entanglement in many-body systems." *Reviews of Modern Physics*, **80** (2008) 517.
- [4] G. J. Mooney, C. D. Hill, and L.C. L. Hollenberg, "Entanglement in a 20-Qubit Superconducting Quantum Computer." *Scientific Reports*, **9** (2019) 13465.
- [5] S. P. Kulik, "Quantum teleportation with qubits", Kulik, S. P. "Quantum teleportation with qubits." *Russian Microelectronics*, **35** (2006).
- [6] W. K. Wootters, "Quantum Entanglement as a Resource for Communication. In: *Quantum Mechanics at the Crossroads.*" The Frontiers Collection. Springer, Berlin, Heidelberg (2007).
- [7] S. Simmons, R. Brown, H. Riemann, et al." Entanglement in a solid-state spin ensemble." *Nature*, **470** (2011) 69.
- [8] G. Burkard, "Spin-entangled electrons in solid-state systems." *Journal of Physics: Condensed Matter*, **19** (2007) 233202.
- [9] G. L. Kamta, A. F. Starace, "Anisotropy and Magnetic Field Effects on the Entanglement of a Two Qubit Heisenberg XY Chain." *Physical Review Letters*, **88** (2002) 107901.
- [10] K. Guo, M. Liang, H. Xu, et al. "Entanglement in a two-spin (1/2, 3/2) mixed-spin Heisenberg XX chain with an inhomogeneous external magnetic field." *Journal of Physics A: Mathematical and Theoretical*, **54** (2011) 491.
- [11] L. S. Lima, "Thermal Entanglement in the Quantum XXZ Model in Triangular and Bilayer Honeycomb Lattices." *Journal of Low Temperature Physics*, **198** (2020) 241.
- [12] T. Martin, T. A. Giresse, "Entanglement Dynamics of a Two-qubit XYZ Spin Chain Under both Dzyaloshinskii-Moriya Interaction and Time-dependent Anisotropic Magnetic Field." *International Journal of Theoretical Physics*, **59** (2020) 2232.
- [13] Z. Ling, Y. Xue-Xi, S. He-Shan, G. Yan-Qing, "Thermal entanglement in 1D optical lattice chains with nonlinear coupling." *Chinese Physics*, **14** (2005) 1168.
- [14] V. Murg, F. Verstraete, J. I. Cirac, "Variational study of hard-core bosons in a two-dimensional optical lattice using projected entangled pair states." *Physical Review A*, **75** (2007) 033605.
- [15] G. Burkard D. Loss, and D. P. DiVincenzo, "Coupled quantum dots as quantum gates." *Physical Review B*, **59** (1990) 2070.
- [16] W. D'ur, G. Vidal, and J. I. Cirac Dür, Wolfgang, Guifre Vidal, and J. Ignacio Cirac. "Three qubits can be entangled in two inequivalent ways." *Physical Review A*, **62** (2000) 062314.
- [17] F. Kheirandish, S. J. Akhtarshenas, and H. Mohammadi, "Effect of spin-orbit interaction on entanglement of two-qubit Heisenberg X Y Z systems in an inhomogeneous magnetic field." *Physical Review A*, **77** (2008) 042309.
- [18] F. Rojas, "Thermal entanglement of a coupled electronic spins system: interplay between an external magnetic field, nuclear field and spin-orbit interaction." *Quantum Information Processing*, **14** (2015) 1973.
- [19] O. S. Duarte, C. S. Castro, D. O. Soares-Pinto, M. S. Reis, "Witnessing spin-orbit thermal entanglement in rare-earth ions." *Europhysics Letters*, **103** (2013) 40002.
- [20] G. Vidal and R. F. Werner, "Computable measure of entanglement." *Physical Review A*, **65** (2002) 032314.



DFT study of silicon channel effects embedded between armchair graphene nanoribbons with different widths on mechanical and electronic properties

Scientific research paper

Mehdi Zarepour*

Microwave/mm-wave and Wireless Communication Research Lab, Electrical Engineering Department, Amirkabir

University of Technology, Tehran, Iran

ARTICLE INFO

Article history:

Received 8 October 2021

Revised 16 November 2021

Accepted 16 November 2021

Available online 10 December 2021

Keywords:

Graphene nanoribbon

Silicon channel

Bandgap

DFT

ABSTRACT

Graphene Nano-Ribbons (GNR) are strong candidates for future materials in the electronics industry. In this paper, we extract the mechanical and electrical properties of AGNRs combination of different widths and deposition of silicon dimer to create Metal-insulator-semiconductor by the DFT method. Results demonstrate that by decreasing the mean width and strain of AGNR-AGNR composite and replacing the carbon dimer with silicon dimer, the bandgap of the system will reduce. The AGNR-Si-AGNR composite is a promising candidate for transistor application due to the small bandgap and high current flow allowance because of the high electron state near the Fermi's level electronic state involvement under the bias voltage.

1 Introduction

Electronic devices are everywhere in our lives since miniaturization using the Nanoscale components has allowed extremely powerful devices to be portable. Graphene's unique mechanical, electrical, and thermal properties have attracted attention for various applications such as electronic applications [1,2]. Some of these properties are incredibly strong, about 200 times stronger than steel, high thermal conductivity (5 KW/mK), high electron mobility at room temperature (2.5×10^4 cm²/V.s), high surface to the volume ratio (2630 m²/g), and high modulus of elasticity (1TPa) [3]. Indeed, graphene's current density is 10⁶ times greater than copper's current, and its mobility is estimated to be 250 times that of silicon. In addition to all of this, its flexibility and other properties make it ideal for various applications, from solar cells,

battery technology, piezoelectric, touch screens, gas sensors, biosensors, and many others [4, 5].

Graphene does not possess a bandgap by itself; therefore, it cannot be used in electronics, which requires large current on/off ratios. In the case of nanoribbons, they may have the bandgap due to the width differences. For specific graphene ribbons of a few nm in width, the theory predicts that the bandgap varies as a function of the ribbon width W [6, 7] with $\Delta E(W) \sim 1\text{eV} \cdot 0 \text{ nm}/W$. This means that the bandgap of ~ 100 meV is expected for a ribbon of 10 nm, or conversely, a ribbon of width ~ 1 nm would be required to get the bandgap of silicon (~ 1 eV). As quantum confinement only relies on the geometric structure of the ribbon, the bandgap can in principle be varied by design, contrary to the fixed bandgap of a semiconductor like silicon. Moreover, graphene high mobility and high current

*Corresponding author.

Email address: MehdiZarepour@aut.ac.ir

DOI: 10.22051/jitl.2022.38021.1063

carrying capabilities, has motivated us to combine graphene nanoribbons with silicon to achieve a semiconductor composition or Schottky contact.

Graphene not only exhibits excellent mechanical, thermal, optoelectronic, and electrical properties but can also be combined with several organic materials to produce high-performance organic field-effect transistors [8]. From the semiconductor technology point of view, there are two incredible properties which make graphene more special than the other semiconductors, 1) zero-overlap with very high electron transfer, 2) zero bandgap opening at the Dirac point where conduction and valence bands meet each other [9]. This characteristic of semiconductors is due to the current flow over the gap between the valence band and conduction band. This flow can emerge with light absorption, heat, or external electric field induction. If the flow is generated by the external electric field to switch “on” and “off”, then it is called field-effect transistors (FETs) [10, 11]. Consequently, the bandgap should emerge in graphene for use as a semiconductor. There are several methods that have developed to imply bandgap in graphene, such as exposure to a vertical electric field, vacancy in the crystalline structure, adding impurities, dopant, oxidation, alloys, and decreasing the width of the graphene sheets [12].

Graphene strips, which have a width of several nanometers, are known as graphene nano-ribbons (GNR) [13]. Many studies focus on the electrical properties of GNR, which have shown the effects of the edges open to the bandgap [3,5,14]. The edges of these structures are classified into two different categories of armchairs and zigzags [3]. The zigzag structures can be metallic, but armchair structures can exhibit metal or semiconducting properties, which in a semiconductor state, the energy gap changes with the ribbon width [15]. Therefore, electrical properties in nanotechnology applications are characterized by the shape of the edge and width of the nanoribbon [16]. Fabrication of GNR has been reviewed by Celis et al. [12], and it has revealed that the bandgap varies in different fabrication mechanisms.

Recently, band engineering and elastic metallic and semiconductor properties of strained armchair GNR (AGNR) were studied by Prabhakar et al. [1]. They showed that the strained GNR passivized with

hydrogen molecules could have large out-of-plane deformations demonstrating the properties of relaxed shape graphene.

The metal-semiconductor junction of GNR was studied by Hong et al. [17]. Four types of this junction have been simulated to show that the junction conductance strongly depends on the atomistic features of the access geometry from the metallic GNR to the semiconducting GNR. Sevinçli et al. [18] demonstrated that periodically repeated junctions of AGNRs of different widths formed multiple quantum well structures and showed that periodically repeating heterojunctions made of armchair graphene nanoribbons of different widths can form stable superlattice structures. Another junction is the semiconductor-semiconductor heterostructure (SSH) AGNR junction. SSH's energy gap can be tunable, and it is possible to bring a bright future for graphene electronic applications [19]. Graphene heterojunctions are used in transistors [20] and photodetectors [21].

In this research, three types of AGNR metal-semiconductor junctions included GNR6(+)-GNR5, GNR6-GNR5(+), and GNR-Silicon-GNR (GSG), are analyzed by using the Density Functional Theory (DFT) method as shown in Fig.1. Silicon atoms have larger core dimensions than carbon, electrons in the valence band can participate more freely in the conduction process than carbon atoms. Consequently, a gate or channel forms in the Si atoms ambience.

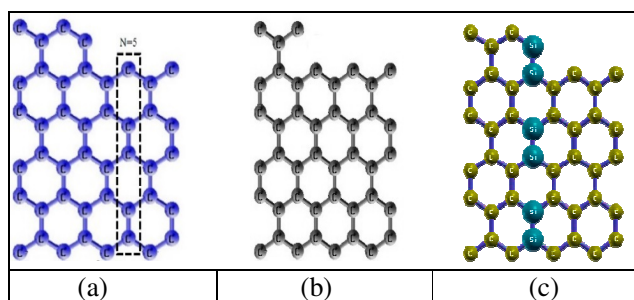


Figure 1. (a) Armchair GNR6(+)-GNR5. (b) Armchair GNR6-GNR5(+). (c) AGNR-silicon-AGNR-silicon (GSG) structure.

Their mechanical, electrical, and semiconductor properties have been studied by charge total energy, stress, strain, charge analysis, density of states (DOS) and band structure. A quantum espresso (QE) package has been used to study the structures. QE is an integrated suite of Open-source computer codes for electronic-structure calculations and materials

modelling. It is based on DFT, plane waves, and pseudopotentials [22].

2 Theoretical and computational method

DFT is a prevalent method for many-body systems by solving approximate versions of the Schrodinger equation [23, 24]. The accuracy of this method is noticeable [25]. This is not a single unit but usually comes as various parts, each intended to include some physical effects [6]. The electronic structure calculation employs the first principle method containing the self-consistent pseudopotential method [26-27] using the B3LYP¹. Hybrid methods attempt to incorporate some of the more useful features from Abinitio or empirical methods (specifically Hartree-Fock methods) with some of the improvements of DFT mathematics while tending to be the most commonly used method for computational chemistry practitioners [23]. This method becomes one of the most popular semi-empirical hybrid functional methods [6,25].

To obtain the optimized atomic position and relax the atomic structure, an energy cutoff of 40 Ry is employed. A double plus polarization basis set is used for the localized basis orbitals to deal with the many atoms in a unit cell of the GNRs of various widths [28]. After relaxing the structures, self-consistent calculations are employed to extract the right plane waves, eigenvalues, eigenvectors, and Fermi's energy. Then, to cover all probable states, non-self-consistent calculations are carried with a 12*1*1 K-Point mesh in reciprocal space. In the next step, the K-Gamma-M-K route for electron motion vectors in reciprocal space is divided to 60 points to calculate energies and, consequently, the band structure of composites.

Furthermore, the DOS, charge analysis, and partial density of states are calculated. The same process has been done to extract GNR(6)-GNR(5) and GNR(6)-Si-GNR(5) properties and investigate the effects of the combinations, and silicon channel replaced by carbon dimer. The optimized distance between two lattices of 15 Å was employed to neglect the interaction between layers.

For AGNR with a width of N (N is the number of dimers) or ribbon width ($W = (N - 3) \frac{\sqrt{3}}{2} + \sqrt{3}$), for $\frac{1}{W} \ll 1$, the bandgap's energy Δ_a is given by [7]:

$$\Delta_a \sim \begin{cases} 0, & N = 3m - 1 \\ \frac{\pi}{W + \frac{\sqrt{3}}{2}}, & N = 3m \\ \frac{\pi}{W}, & N = 3m + 1 \end{cases}, \quad (1)$$

where $m=1, 2, 3, 4, \dots$. According to Eq. (1), the system is metallic when $N=3m-1$.

Here for $m=2$, N will be 5, 6, 7. For $N=5$ dimers, the bandgap is equal to 0 (as shown in Fig.2), and in the case of $N = 6$ from Equation (1), the bandgap is equal to 0.6 eV. To study the effect of the combination of $N=5$ and $N=6$ GNRs together without the intermediate channel, the configuration of two systems consisting of one more dimer from each GNRs with different widths like Fig. 1 has been considered. Following the previous study, the bandgap of the GNRs has an inverse relation with the GNRs width, and therefore, by increasing the GNR width, the bandgap will decrease [7].

Indeed, the bandgap has a direct [27] relation with strain. As strain increases, a small shift in minimum conduction and maximum valance band states will appear, and the current transmitted under bias voltage will increase with strain reduction. Therefore, strains are calculated for these structures from the young modulus and stress tensor.

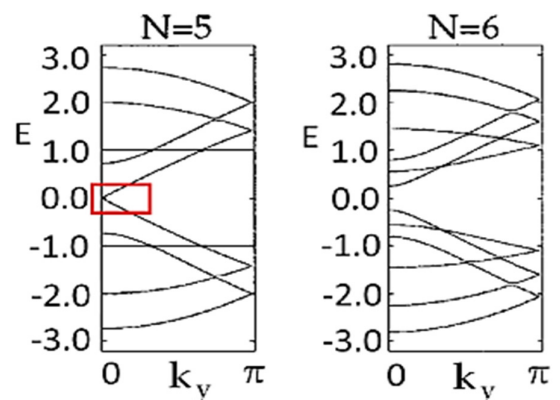


Figure 2. Band structure of $N=5$ dimers and $N=6$ dimers of AGNR [5, 28].

¹ Becke, 3-parameter, Lee-Yang-Parr

3 Results and discussion

After relaxing the structures, a bond length of 1.418 Å is obtained. The lowest energy is resulted in the GNR-Si-GNR configuration which indicates that this composite is more stable than other configurations. The flat structure remains for all of the composites where deflection or defect is found.

The DOS calculations are shown in Fig. 3 for all of the composites. The Fermi's level is shifted to 0. For the GNR6(+)-GNR5, most of the states are accommodated at the conduction band, but for the GNR6-GNR5(+) most of the states are located at the bottom of Fermi's level. In the case of GNR6-Si-GNR5, states are accumulated near the Fermi level. These results show that replacing the silicon channel modifies the semiconductor properties of the composite, and more current will appear under the bias voltage. Moreover, as shown in Table 1, Lowdin's charge analysis shows that by replacing the silicon channel with carbon dimer, charges from silicon atoms move toward the neighbor carbon dimers. This is another support for the DOS results, which is declared under the bias voltage, where more current will flow at the channel.

Normalized band structure diagrams are plotted in the K-Gamma-M-K path in the Brillouin Zone as shown in Fig. 4. The results of this section confirm the results discussed in the previous section. By decreasing the width of GNRs, the bandgap will decrease. For the GNR6(+)-GNR5 the bandgap value is equal to 0.3 eV which is very close to the theoretical predictions discussed in Eq. (1). For the GNR6-GNR5(+) configuration, the bandgap will decrease to 0.19 eV due to reduction in the mean width. However, the main result is the reduction of the bandgap energy due to the replacement of the carbon dimer by the silicon channel.

In case when the electrons of the valance band get closer to the conduction band in turn increases the current once the bias voltage employees due to the involvement of more states. Indeed, mechanical properties are calculated from the stress tensor and reported young modulus for GNRs before calculating the strain from $E = \sigma / \varepsilon$. The results are 0.0103, 0.0105, and 0.0078 for GNR6(+)-GNR5, GNR6-

GNR5(+), and GNR6-Si-GNR5, respectively. These results are another witness to decreasing the bandgap by silicon dimer replacement. According to the claim of the previous section, by decreasing the strain of the system, the bandgap will decrease.

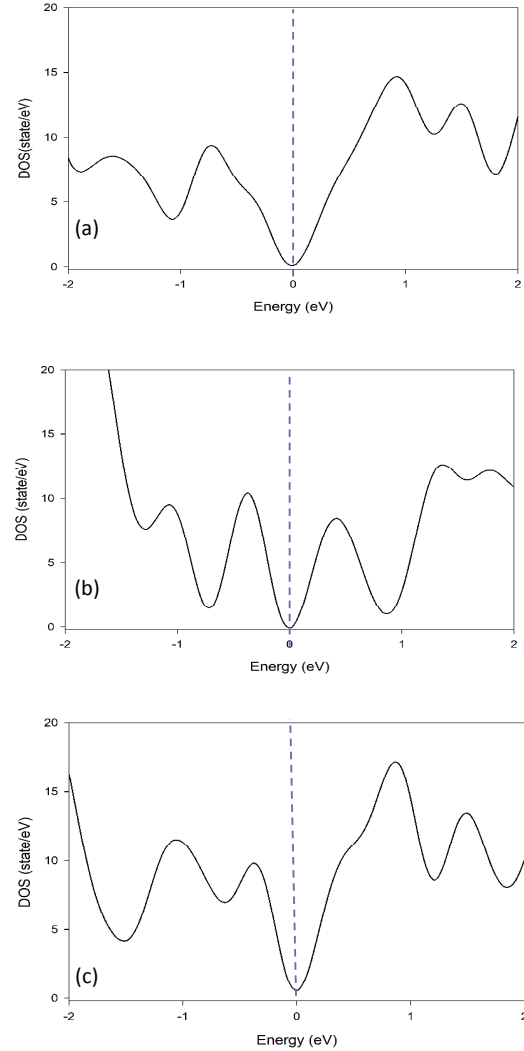


Figure 3. (a) DOS diagram of GNR6(+)-GNR5. (b) Armchair GNR6-GNR5(+). (c) AGNR-silicon-AGNR-silicon (GSG) structure.

I simulated the semiconductor AGNR with $N=6$ connects to metal AGNR with $N=5$, as shown in Fig. 1a. In the GNR-GNR (GG) structure, the energy band gap is modulated in real space where specific states are confined in certain segments [18] as shown in Fig. 2.

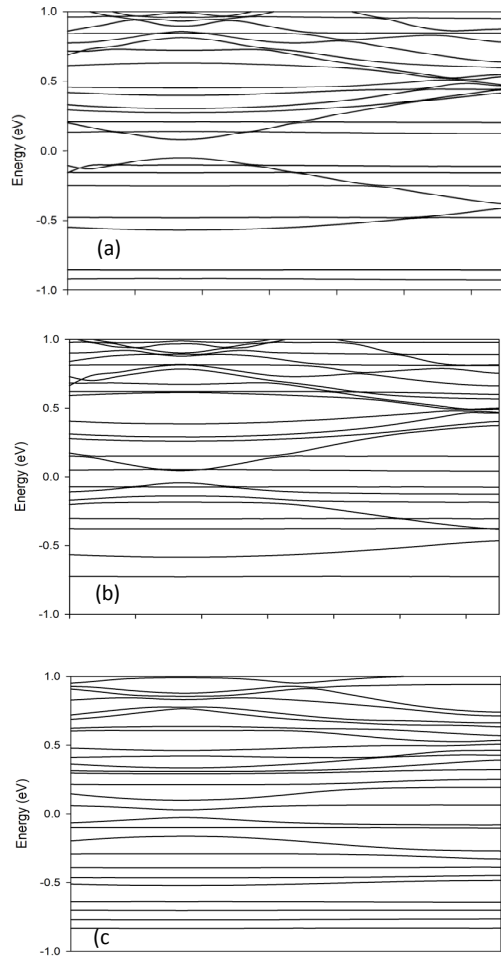


Figure 4. (a) Band structure diagram of GNR6(+)-GNNR5. (b) Armchair GNR6-GNNR5(+). (c) GNR-silicon-GNR-silicon (GSG) structure.

Band structure calculations allow extracting partial density of states (PDOS), which represent the number of energy levels per unit energy that show the electronic coupling and orbital contributions. PDOS clearly explains the details of modifications in the energy band structure due to the bonding between Si and C atoms.

Moreover, to determine the bandgap opening and electronic characterization, by considering the shape of curves near the Fermi level, one can interpret the system. S, P_x, P_y, and P_z orbitals of silicon and carbon in the composite have been plotted to be compared together and to determine the overlap after the creation of bonds and whether the bonds are strong or not.

Table.1 Lowdin charges of atoms and orbitals near silicon channel

Left carbon dimer before substitution of silicon channel	Atom # 13: total charge = 3.9139, s = 0.9855, p = 2.9284, Atom # 14: total charge = 3.9348, s = 0.9282, p = 3.0066, Atom # 15: total charge = 3.9362, s = 0.9343, p = 3.0019, Atom # 16: total charge = 3.9244, s = 0.9336, p = 2.9908, Atom # 17: total charge = 3.9401, s = 0.9266, p = 3.0135, Atom # 18: total charge = 3.9783, s = 1.0648, p = 2.9136,
Left carbon dimer after substitution of silicon channel	Atom # 13: total charge = 4.1718, s = 1.0299, p = 3.1419, Atom # 14: total charge = 4.1793, s = 1.0643, p = 3.1150, Atom # 15: total charge = 4.2036, s = 1.0257, p = 3.1778, Atom # 16: total charge = 4.1844, s = 1.0408, p = 3.1436, Atom # 17: total charge = 4.1953, s = 1.0285, p = 3.1668, Atom # 18: total charge = 4.2254, s = 1.0143, p = 3.2111,
Right carbon dimer before substitution of silicon channel	Atom # 19: total charge = 3.8924, s = 1.0733, p = 2.8191, Atom # 22: total charge = 3.9295, s = 0.9238, p = 3.0057, Atom # 23: total charge = 3.9089, s = 0.9227, p = 2.9862, Atom # 26: total charge = 3.9047, s = 0.9401, p = 2.9646, Atom # 27: total charge = 3.9608, s = 0.9188, p = 3.0420,
Right carbon dimer after substitution of silicon channel	Atom # 19: total charge = 4.5762, s = 1.0889, p = 3.4873, Atom # 22: total charge = 4.1306, s = 1.0363, p = 3.0942, Atom # 23: total charge = 4.1925, s = 1.0258, p = 3.1667, Atom # 26: total charge = 4.1440, s = 1.0415, p = 3.1025, Atom # 27: total charge = 4.2363, s = 1.0081, p = 3.2282, Atom # 28: total charge = 3.8655, s = 0.9158, p = 2.9498,

As shown in Fig. 5, the majority of S orbital states of carbon are placed between -22 and -15 eV, far from the Fermi level, and for the Silicon atoms, the majority of S orbital states are placed between -15 and -7.5 eV.

In the case of P_x orbitals of silicon and carbon atoms (as shown in Fig 6), for both orbitals, most states are placed between -10 and 5, and the main contribution lies in the construction of the bond.

For P_y orbitals of two atoms, as observed from Fig. 7, the states are distributed between -20 and 5 eV, but the strong peaks are at -5 to -10 eV. Common states are not as much as those for P_x orbitals. Due to the high overlap of these orbitals, they play a significant role in C-Si-Cbond formation.

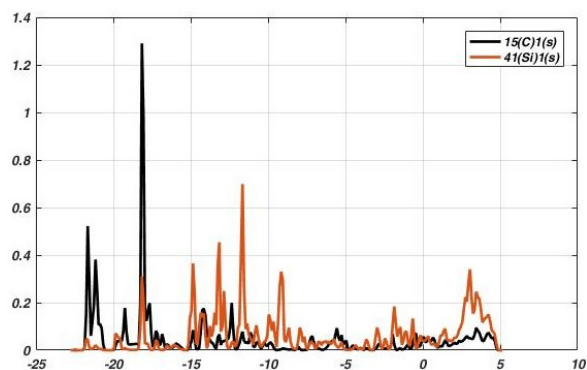
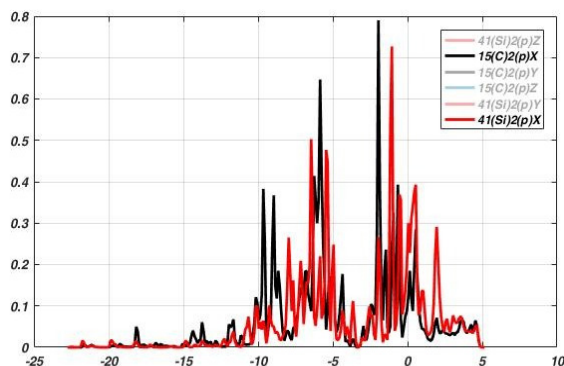
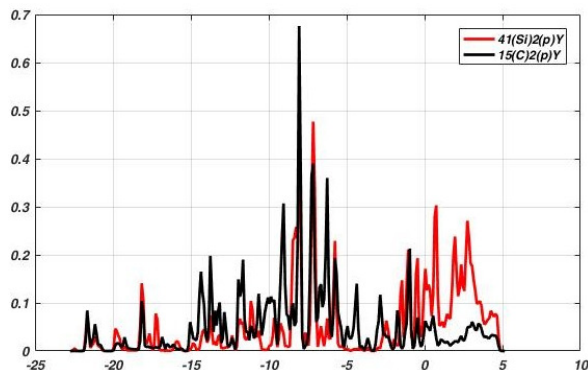


Figure 5. DOS versus Energy S orbit of Carbon and Silicon.

Figure 6. DOS versus Energy P_x orbit of Carbon and Silicon.Figure 7. DOS versus Energy P_y orbit of Carbon and Silicon.

This comparison is also made for the pair of other orbitals. Results demonstrate that these pairs have not significantly contributed to the bond. Among them, three pairs of above orbitals play an essential role in the formation of a strong bond due to the state overlaps.

4 Conclusions

In this study, it is found that the energy gap of the AGNR-Si-AGNR structure can be modulated in a wide

range. Studies under DFT methods and quantum espresso (QE) packages show that the electronic properties of GNRs and their composites are functions of their widths and impurities. The composition of GNRs with different widths, can tune the bandgap and other properties, leading to design PN junctions. Moreover, by substitution of carbon dimer by the silicon dimer, this composite shows semiconductor properties, which can be used as the field effect transistors. It will show an increase in current flow under the external bias voltage due to the enhancement of electronic states near the Fermi energy.

Availability of data and materials

The datasets used and/or analyzed during the current study are available from the corresponding author on reasonable request.

Competing interests

The authors declare that they have no competing interests.

Funding

There is no funding.

Acknowledgment

I would like to thank Amirkabir University of Technology for supporting this research.

References

- [1] S. Prabhakar, R. Melnik, "Band engineering and elastic properties of strained armchair graphene nanoribbons: semiconductor vs metallic characteristics." arXiv preprint arXiv:1901.00576, 2019.
- [2] F. Schwierz, "Graphene transistors." *Nature Nanotechnology*, **5** (2010) 487.
- [3] E. Kan, Z. Li, J. Yang, "Graphene nanoribbons: geometric, electronic, and magnetic Properties." *Physics and Applications of Graphene-Theory*, Sergey Mikhailov, IntechOpen (2011).
- [4] J. Wang, M. Liang, Y. Fang, T. Qiu, J. Zhang, L. Zhi, "Rod-coating: towards large-area

- fabrication of uniform reduced graphene oxide films for flexible touch screens." *Advanced Materials*, **24** (2012) 2874.
- [5] M. Aliofkhazraei, N. Ali, W. I. Milne, C. S. Ozkan, S. Mitura, J. L. Gervasoni, *Graphene Science Handbook: Nanostructure and Atomic Arrangement*: CRC Press (2016).
- [6] J. R. Reimers, "Computational methods for large systems: electronic structure approaches for biotechnology and nanotechnology." *John Wiley & Sons* (2011).
- [7] K. Wakabayashi, K.-i. Sasaki, T. Nakanishi, T. Enoki, "Electronic states of graphene nanoribbons and analytical solutions." *Science and Technology of Advanced Materials*, **11** (2010) 054504.
- [8] F. Hao, X. Chen, "First-principles study of lithium adsorption and diffusion on graphene: the effects of strain." *Materials Research Express*, **2** (2015) 105016.
- [9] D. R. Cooper, B. D'Anjou, N. Ghattamaneni, B. Harack, M. Hilke, A. Horth, et al., "Experimental review of graphene. *International Scholarly Research Notices*." **2012** (2012) 501686.
- [10] F. Schwierz, "Graphene transistors." *Nature Nanotechnology*, **5** (2010) 487.
- [11] N. Lu, L. Wang, L. Li, M. Liu, "A review for compact model of graphene field-effect transistors," *Chinese Physics B*, **26** (2017). 036804.
- [12] A. Celis, M. Nair, A. Taleb-Ibrahimi, E. Conrad, C. Berger, W. De Heer, et al., "Graphene nanoribbons: fabrication, properties and devices." *Journal of Physics D: Applied Physics*, **49** (2016) 143001.
- [13] T. Fang, A. Konar, H. Xing, D. Jena, "Mobility in semiconducting graphene nanoribbons: Phonon, impurity, and edge roughness scattering." *Physical Review B*, **78** (2008) 205403.
- [14] A. Naeemi, J. D. Meindl, "Conductance modeling for graphene nanoribbon (GNR) interconnects." *IEEE electron device letters*, **28** (2007) 428.
- [15] P. Zhao, M. Choudhury, K. Mohanram, J. Guo, "Analytical theory of graphene nanoribbon transistors." *Design and Test of Nano Devices, Circuits and Systems, 2008 IEEE International Workshop on*, pp. 3-6, 2008
- [16] S. Mehmet Gokhan, "The effects of vacancy location and concentration on the transport properties of armchair and zigzag graphene nanoribbons." *Materials Research Express* (2019).
- [17] S. Hong, Y. Yoon, J. Guo, "Metal-semiconductor junction of graphene nanoribbons." *Applied Physics Letters*, **92** (2008) 083107.
- [18] H. Sevinçli, M. Topsakal, S. Ciraci, "Superlattice structures of graphene-based armchair nanoribbons." *Physical Review B*, **78** (2008) 245402.
- [19] B. Fan and S. Chang, "Confined state energies in AGNR semiconductor-semiconductor heterostructure." *Physics Letters A*, **381** (2017) 319.
- [20] Y. Lv, W. Qin, C. Wang, L. Liao, X. Liu, "Recent Advances in Low-Dimensional Heterojunction-Based Tunnel Field Effect Transistors." *Advanced Electronic Materials*, **5** (2019) 1800569.
- [21] M. Moradinasab, M. Pourfath, M. Fathipour, and H. Kosina, "Numerical study of graphene superlattice-based photodetectors." *IEEE Transactions on Electron Devices*, **62** (2015) 593.
- [22] <http://www.quantum-espresso.org/resources/tutorials>
- [23] F. Giustino, "Materials modelling using density functional theory: properties and predictions" *Oxford University Press* (2014).

- [24] R. M. Martin, "Electronic structure: basic theory and practical methods." Cambridge university press (2004).
- [25] A. Shokuhi Rad, M. Esfahanian, S. Maleki, G. Gharati, "Application of carbon nanostructures toward SO₂ and SO₃ adsorption: a comparison between pristine graphene and N-doped graphene by DFT calculations." *Journal of Sulfur Chemistry*, **37** (2016) 176.
- [26] E. Rudberg, P. Salek, Y. Luo, "Nonlocal exchange interaction removes half-metallicity in graphene nanoribbons." *Nano letters*, **7** (2007) 2211.
- [27] G. Gui, J. Li, and J. Zhong, "Band structure engineering of graphene by strain: first-principles calculations." *Physical Review B*, **78** (2008) 075435.
- [28] Y. W. Son, M. L. Cohen, S. G. Louie, "Energy gaps in graphene nanoribbons." *Physical review letters*, **97** (2006) 216803.
- [29] N. Merino-Díez, A. Garcia-Lekue, E. Carbonell-Sanromà, J. Li, M. Corso, L. Colazzo, et al., "Width-dependent band gap in armchair graphene nanoribbons reveals Fermi level pinning on Au (111)." *ACS nano*, **11** (2017) 11661.



Effect of vacancy defects on the Josephson current in zigzag graphene narrow strips

Scientific research paper

Somayyeh Zareei¹, Vahid Daadmehr^{1,2*}, Hossein Hakimi Pajouh^{1*}, Zahra Faraei³

¹*Department of Physics, Faculty of Physics and Chemistry, Alzahra University, Tehran, Iran*

²*Magnet & Superconducting Res. Lab, Department of Physics, Alzahra University, Tehran, Iran*

³*Department of Physics, Institute for Advanced Studies in Basic Sciences (IASBS), Zanjan 45137-66731, Iran*

ARTICLE INFO

Article history:

Received 8 October 2021

Revised 16 November 2021

Accepted 19 November 2021

Available online 10 December 2021

Keywords:

Graphene narrow stripe

Josephson current

Vacancy defect

Lattice model

ABSTRACT

We investigate the Josephson current in a superconductor/zigzag graphene narrow strip/superconductor (Sc-ZGNS-Sc) junction with vacancy defects. For this purpose, we extend a recursive Green's function based numerical method to ZGNSs and take into account the effect of vacancies including random single vacancy distributions and also chain-like linear defects. We investigate how the Josephson current is affected by the length and width of the strip and the concentration of the vacancies. We find that the Josephson current exhibits an exponential dependence on the vacancy concentration. The exponent coefficient is a nonlinear function of the length of the lattice and the vacancy concentration. For the width dependence we find a linear relation between the Josephson current and the width of the ZGNS which propose a semi classical treatment of the electron transport in the system. Finally, we study the effect of chain-like linear defects and compare them with randomly distributed single vacancies.

1 Introduction

Since its discovery, graphene, a single atomic layer of carbon atoms in a hexagonal lattice structure, has attracted much research attention, both theoretically and experimentally, due to its unique mechanical, thermal, and electrical properties [1, 2, 3]. The peculiar electronic structure of graphene has become a major cause of enthusiasm among scientists. Linear energy dispersion relation near the discrete Fermi points and chiral nature of charge carriers in graphene has been reported which have caused attractive phenomena [4, 5]. Among the phenomena of graphene, the superconducting proximity effect is one of the most attractive properties from both basic and applied points

*Corresponding authors.

Email address: Daadmehr@alzahra.ac.ir; hhpajouh@Live.com

DOI: 10.22051/jitl.2022.37391.1061

of view. This phenomena has been studied theoretically [6] and experimentally [7] where good contacts between the superconductor electrodes and graphene have been established while the Josephson current through a superconductor-graphene-superconductor junction has been measured.

In graphene, high carrier mobility at room temperature, and unique electrical properties make them a promising material for a variety of nano-electronics applications [8]. At present, graphene can be synthesized in two ways: namely top-down method and bottom-up method. The top-down approach can involve the structural breakdown of graphite followed by the interlayer separation to produce graphene sheets

[9] while the bottom-up technique such as chemical vapor deposition, epitaxial growth and total organic synthesis implements carbon molecules as building blocks [10]. In the preparation processes of graphene, it is difficult to avoid defects. Various defects, such as vacancy defects [11, 12, 13], impurity defects [14, 15] and adsorption defects [16, 17], could be introduced. In most cases these unavoidable defects can influence the characteristics of the graphene, such as energy band structure, carrier mobility, thermal and electrical conductivities, electronic transport properties like the Josephson current and so on. On the other hand, the different types of defects could change the topology or the curvature and then change the geometric structure of graphene [18]. Perhaps even more importantly, nearest neighbor carbon atoms to defect rearrange themselves into a variety of different polygons, not only hexagons (pentagons, octagons and so on), to form different structures with lower energy states by changing the bonding geometry around the defect. The vacancy defects, which are a very basic type of defect, are discussed here. A vacancy defect is empty space of a carbon atom located in the inner part or on the edge of graphene, which usually either appears during synthesis process [19, 20], or artificially is produced by techniques like ion and electron irradiation or chemical approaches [12, 13, 21].

The effect of short-range disorder on graphene's conductance has been investigated in [22]. It was illustrated in [23] that the electrical conductance of graphene largely depends on the type and concentration of point defects. Single vacancy low concentrations noticeably do not degrade electron transport. In comparison, double vacancy induces a moderate reduction of 25–34% in graphene. By increasing the concentration of defects, the electrical conductivity can be reduced by a factor of about 2-3 compared to low concentrations. Reference [24] investigates the disordered single-layer graphene Josephson junctions with dimension of $W \gg L$ and shows that if we consider the average current as a function of vacancy concentration, increasing vacancy concentration leads to power-law suppression of the critical current.

Reference [25] shows that the position and concentration of vacancies in graphene nanoribbons affect their transmission spectrum and thus their current-voltage characteristics. Motivated by this, we

present in this paper a numerical study of the Josephson current in a graphene strip Josephson junction with different vacancy concentrations.

In our previous work [26], we examined the Josephson current for a graphene strip without vacancy, the results of which were in good agreement with the theoretical and experimental results obtained for graphene. Josephson current in a two dimensional square lattice contacting two superconductors was studied by Furusaki [27]. Generalizing the conventional recursive Green's function technique to superconducting systems, he developed a method to numerically study the DC Josephson current in dirty SNS junctions. The results showed an agreement with the estimations of analytic calculations. Extending this formalism to brick lattices, we study the Josephson effect in a narrow strip of graphene with arbitrary length L and width $W < L$ for zigzag edges. Transferring the hexagonal lattice structure into a brick-like structure conserves the lattice topology [28], which is responsible for the low-energy excitations of the graphene strip. With this method, we investigate the Josephson current in graphene strips with different length and different vacancy concentrations.

The paper is organized as follows. In section 2 we describe our numerical method to calculate the Josephson current using a lattice model which is a basic tool for the numerical study of the effects of vacancy defects. In section 3, results are presented followed by the related discussions. Finally, we end the paper with the main conclusions in section 4.

2 Model and method

The system consists of a graphene nano stripe (GNS) coupled to two conventional s-wave spin-singlet superconductor leads as shown in Figure 1. We proposed a 2D array arranged in a brick-wall lattice. This lattice represents a special case of the honeycomb lattice [28, 29], both of which can be strained into each other through continuous deformation and support two Dirac points in the corners of the 2D Brillouin zone (Fig. 2). By this consideration, our starting point is the tight-binding Hamiltonian on the pristine (without vacancy) Sc-GNS-Sc system, which we include the possibility for different horizontal and vertical nearest neighbors hopping. The full Hamiltonian takes the form:

$$\begin{aligned}
 H = & -t_h \sum_{\sigma} \left(\sum_{j=0}^{n_x} \sum_{k=0}^{n_y} (c_{j,k,\sigma}^{\dagger} c_{j-1,k,\sigma} + c_{j-1,k,\sigma}^{\dagger} c_{j,k,\sigma}) \right) - \\
 & t_v \sum_{\sigma} \left(\sum_{\substack{j=0 \\ j \text{ is odd}}}^{n_x} \sum_{k=0}^{n_y} (c_{j,k,\sigma}^{\dagger} c_{j,k+1,\sigma} + c_{j,k+1,\sigma}^{\dagger} c_{j,k,\sigma}) \right) - \\
 & t_v \sum_{\sigma} \left(\sum_{\substack{j=0 \\ j \text{ is even}}}^{n_x} \sum_{k=0}^{n_y} (c_{j,k,\sigma}^{\dagger} c_{j,k-1,\sigma} + c_{j,k-1,\sigma}^{\dagger} c_{j,k,\sigma}) \right) + \sum_{j=0}^{n_x} \sum_{k=0}^{n_y} \sum_{\sigma} \varepsilon_{j,k} c_{j,k,\sigma}^{\dagger} c_{j,k,\sigma} - \\
 & \mu \sum_{j=-\infty}^{\infty} \sum_{k=0}^{n_y} c_{j,k,\sigma}^{\dagger} c_{j,k,\sigma} - \\
 & \sum_{j=-\infty}^{\infty} \sum_{k=0}^{n_y} (\Delta_{j,k} c_{j,k,\downarrow}^{\dagger} c_{j,k,\uparrow}^{\dagger} + \Delta^* c_{j,k,\uparrow} c_{j,k,\downarrow}), \quad (1)
 \end{aligned}$$

where $c_{j,k,\sigma}^{\dagger}$ ($c_{j,k,\sigma}$) is a creation (annihilation) operator of an electron on site $\mathbf{r} = (j, k)$ with spin σ ($= \uparrow$ or \downarrow). t_h (t_v) is the nearest neighbors hopping matrix element in the horizontal (vertical) direction and μ is the chemical potential. Here, j and k are the cell counters in horizontal and vertical directions, respectively. The number of places in the transverse direction is as $n_y + 1$ and in the horizontal direction is as $n_x + 1$. So, the length of the normal region (L) is $n_x a_0$ and its width (W) is $n_y a_0$, where a_0 is the lattice constant. The system has a strip geometry that confines the graphene electrons in a (large) length and a finite (small) width, so, $n_y \ll n_x$. The order parameter Δ_{jk} is assumed to be constant in the left (Δ_L for $j < 0$) and right ($\Delta_R e^{i\phi}$ for $j > n_x$ that ϕ is the phase difference between the left and right superconductors) superconductors and zero in the middle region ($0 < j_x < n_x$).

Imposing the current conservation law, one finds the Josephson current through the interface between the j th and $(j+1)$ th cells, as follows [27, 30]:

$$\begin{aligned}
 I = & -\frac{iet}{\beta \hbar} \sum_{\sigma} \sum_{k=0}^{n_y} \langle c_{j,k,\sigma}^{\dagger} c_{j+1,k,\sigma} - c_{j+1,k,\sigma}^{\dagger} c_{j,k,\sigma} \rangle \\
 = & \frac{iet}{\beta \hbar} \sum_{\omega_n} \sum_{k=0}^{n_y} \text{Tr} [G_{\omega_n}(j, k; j \\
 & + 1, k) - G_{\omega_n}(j \\
 & + 1, k; j, k)], \quad (2)
 \end{aligned}$$

where $\langle \dots \rangle$ means the thermal average and $\beta = 1/K_B T$ with k_B is the Boltzman constant, and T is the temperature. $G_{\omega_n}(j, k; j', k')$ is the Nambu Green's Function (2×2 matrix) with the Matsubara frequency $\omega_n = \pi K_B T (2n + 1)$ ($n = 0, \pm 1, \pm 2, \dots$) which in each region satisfies the equation of motion [27]:

$$\begin{pmatrix} i\omega_n - \mathbf{H}_{j,k} & -\Delta_{j,k} \\ -\Delta_{j,k}^* & i\omega_n + \mathbf{H}_{j,k}^* \end{pmatrix} \mathbf{G}_{\omega_n}(j, k; j', k') = \delta_{j,j'} \delta_{k,k'}. \quad (3)$$

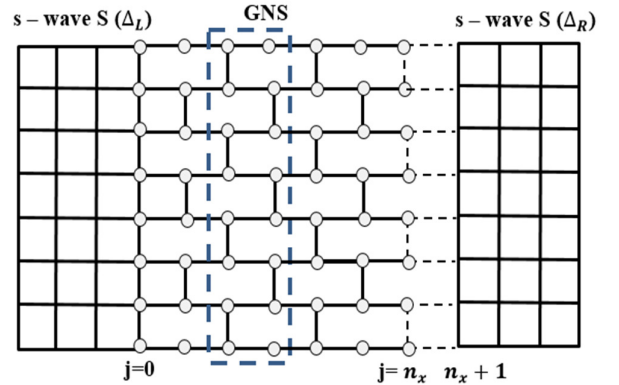


Figure 1. Schematic illustration of the Sc-ZGNS-Sc junction which the order parameter in the left (right) superconductor is as Δ_L ($\Delta_R e^{i\phi}$) and in the middle normal region is zero. The unit cell is indicated with blue dashed lines. White empty circles are the Carbon atoms in the brick-wall lattice of the graphene strip.

It is possible to explicitly calculate the Green's function of three separate regions. Substituting the connected Green's function in Eq. (2) will compute the Josephson current. The procedure has been outlined in detail in Ref [27] and also appendix A. We will here only outline the essentials in order to illustrate how we extend this numerical method to a brick-wall lattice and also how we include the vacancies.

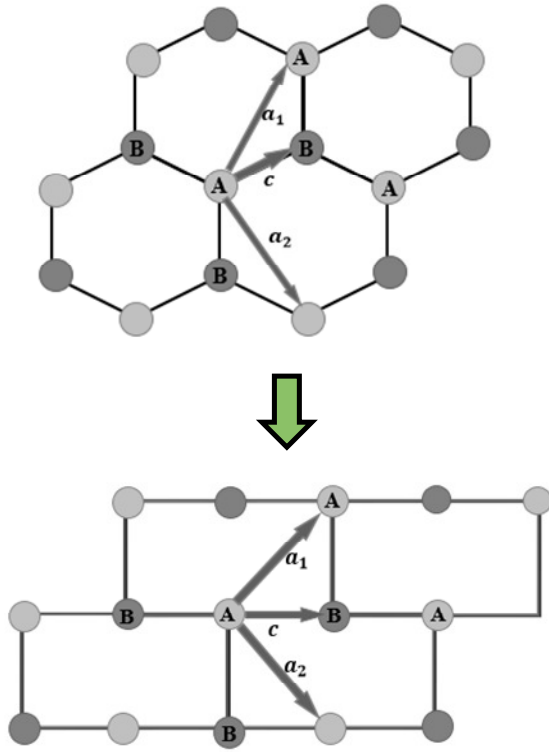


Figure 2. Schematic structure of honeycomb lattice and brick-wall lattice. The sub lattices A and B in the unit cell and the basis vector c is represented in both lattice. The primitive unit cell is defined by the primitive vectors a_1 and a_2 .

For the normal region we can think of unit cells as shown in Figure 1 which the j th cell consists of the sites (j, k) with $k = 0, \dots, ny$. Attaching the cells to the left superconductor one by one and using the curvise Green function method [31], Green's function of the middle region is:

$$G_{\omega_n}(j, k; j', k') = [i\omega_n \delta_{k,k'} I - H_j(k, k') - H_t G_{\omega_n}(j-1, k; j-1, k') H_t]^{-1}, \quad (4)$$

where $H_j(k, k') = \begin{pmatrix} H_0 & 0 \\ 0 & -H_0^* \end{pmatrix}$ is the BdG Hamiltonian of the j th cell with

$$H_0 = -t_v(\delta_{k,k'-1} + \delta_{k,k'+1}) + (\epsilon_{j,k} - \mu)\delta_{k,k'} \quad \text{and} \quad H_t = -t_h \begin{pmatrix} 1 & 0 \\ 0 & -1 \end{pmatrix}$$

being the hopping between two neighboring cells. The effect of a vacancy is taken into account through the change in the hopping elements t_h and t_v . We consider two distinct approaches. In the first approach, removing of a single carbon atom is

equivalent to disappearing of one vertical and two horizontal hopping elements. This attitude is perfected by forming a weak horizontal bond between the left and right atoms of the vacancy which is shown schematically in Figure 3. The new bond has a modified hopping matrix element which is relative to t_h as $t_h e^{-\ell/a}$ with ℓ being the length of the new bond while a is the lattice constant. Accidental placement of two or more holes in a horizontal row corresponds to a longer bond length, resulting in a smaller hopping coefficient.

Our next approach is based on the fact that in graphene, the formation of divacancies (DVs) are energetically more favorable than two separate vacancies (about 8 eV compared to 15 eV) [32, 33]. They can be created either by the coalescence of two single vacancies or by removing two neighboring atoms. The presence of such thermodynamically preferred DVs which causes a defective lattice to be cohesive are very common in reported experimental graphene samples [34, 12]. Removing an atom from the lattice causes the geometry around the vacancy to change so that all the dangling bonds are saturated as the lattice relaxes to a lower energy state. This lattice relaxation leads to non-hexagonal bond geometries and the formation of non-hexagonal rings, causing slight disturbances in the bond lengths around the vacancy (Fig. 9).

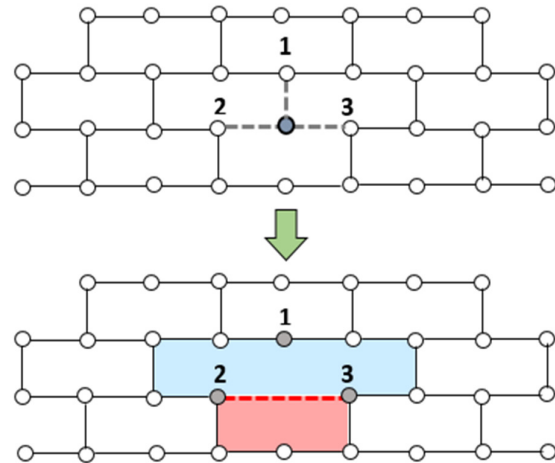


Figure 3. Removing of a single carbon atom of GNS lattice. In the first approach, one vertical and two horizontal hopping elements disappear. In the second approach, removing an atom from the lattice causes the geometry around the vacancy to change so that non-hexagonal rings are formed.

3 Results and discussion

We start with a pristine lattice by considering different lengths from $n_x = 10$ to 120 and different widths from $n_y = 10$ to 50. The chemical potential in the normal region is set to be $\mu_n = 0.001 \text{ eV}$ and for the superconducting regions, we assume $\mu_s = 1.7 \text{ eV}$. This means that the Fermi wave vector in the S regions is large compared to the normal region and so we allowed to adopt a step function model for Δ at the interface [35]. The temperature is $T = 3.13 \text{ K}$ (which is in the range of temperatures related to reference [36]) and we consider three different widths. The results are plotted in Fig. 4a for three values of the width ($n_y/n_x = 0.1, 0.2, 0.5$).

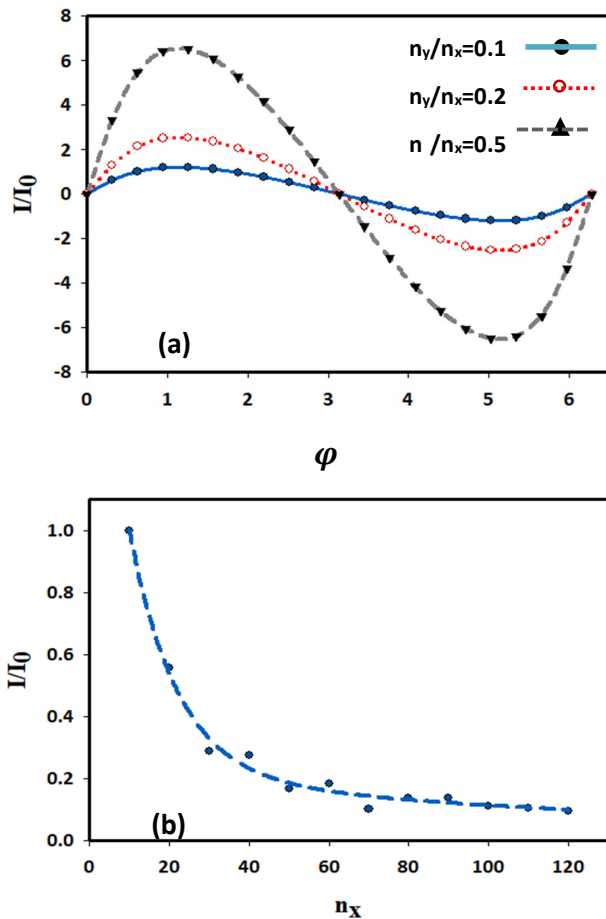


Figure 4. Normalized Josephson current density of Sc-pristine ZGNS-Sc junction in terms of (a) phase difference of superconductors with different ratio of width to the length of the ZGNS region and (b) the length of the graphene strip, with fixed $n_y = 10$. The current is scaled to I_0 that is the current of pristine ZGNS with the width (the length) of $n_y=10$ ($n_x=10$) and $= \frac{\pi}{2}$.

The phase dependence of the Josephson current which deviates from the traditional sinusoidal form, is in good agreement with the predicted theoretical [37] and experimental [36] results. This feature is due to the low density of conduction channels near the Dirac point and exponentially-decaying evanescent states.

This relationship is maintained when the junction length L is shorter than the superconducting coherence length ξ , where $\xi = \hbar v_F / \Delta_0$, to allow coherent transport of superconducting pairs. It should be noted that the largest phase drop we can put over the whole structure is π . Qualitatively, Fig. 4a is in agreement with the numerical results shown in [37]. Reference [36] experimentally measures CPR of a graphene Josephson junction and shows that the CPR is skewed with respect to the commonly observed sinusoidal behavior. As seen, whatever the ratio of the stripe width to the length is greater, the maximum current is also greater, which is the same as the result obtained from Figure 8, in which it was shown that current has linear dependence on the width. Figure 4b shows the length dependence of the current in the short junction region. As can be seen, it decays exponentially with increasing length. In reference [37] it is shown that in low doping limit, $\mu \approx 0$, functionally, the I vs. L dependence form is also close to the traditional Ginzburg-Landau $Ce^{-L/\xi N}$ form.

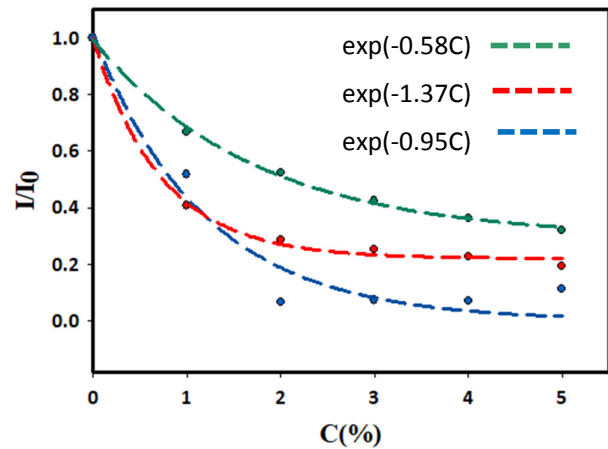


Figure 5. Normalized Josephson current vs. the concentration of vacancies for three different lattice lengths of ZGNS (green dashed line for $n_x=10$, red dashed line for $n_x=50$ and blue dashed line for $n_x=100$).

Now we turn to the vacancy defects. We study how the presence of various distributions of vacancies influences the Josephson current of our system. Figure 5, shows the Josephson current in terms of vacancies concentrations for three different lattice lengths ($n_x = 10, 50, 100$). The vertical axes is normalized to the Josephson current of the perfect sample (I_0). To achieve a satisfactory statistical behavior, we averaged on about 300 different random configurations of vacancy's distributions to obtain each point in these curves. Vacancy concentration (C) which is the ratio of the number of vacancies to the number of all carbon atoms, varies from 0% to 5%. Each single vacancy corresponds to formation of a two adjacent nine-member and five-member neighboring rings (Figure 3). As one can see in Figure 5, the first result is that the presence of vacancies leads to the reduction of the Josephson current. Here the dashed lines show the exponential fits and represent a decay coefficient for each vacancy concentration (γ). As seen, γ is a function of the graphene strip.

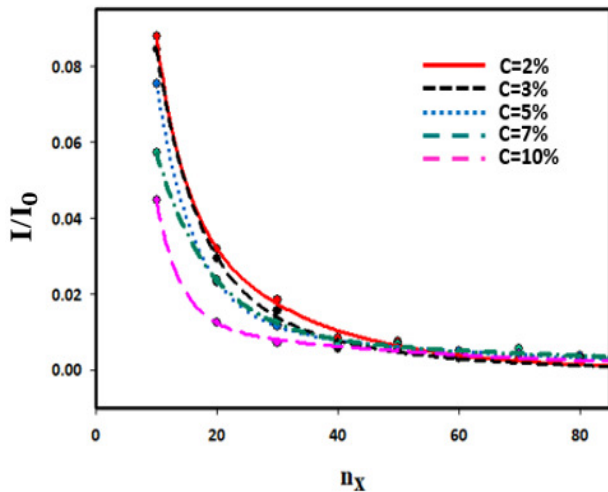


Figure 6. Normalized Josephson current density vs. length of ZGNS for three different concentrations of vacancies (C=2%, 3%, 5%, 7% and 10%). The dashed lines show the exponential fitting.

The longer ZGNS ($n_x=100$) drops faster than those of shorter ones ($n_x=10, 50$) and approaches to zero. Figure 6 shows this feature from a different viewpoint. The Josephson current through the defective ZGNS is plotted as a function of its length at different vacancy concentrations, C=2%, 3%, 5%, 7% and 10%. Each curve defines a localization length (ξ) exponent for a specific concentration which is not only a function of

the system size but it depends on the vacancy concentration. The Josephson current is caused by Andreev bound states that characterize quasi-classical paths that start at one of the superconducting leads and return to the starting point after reaching the opposite superconductor. These Andreev paths constitute the supercurrent channels and the total phase change in each Andreev loop which is related to the mean free path of charge carriers between two superconductors that have to be an integer multiple of 2π . Increasing the vacancy concentration reduces the average free path of the electron, thus reduces the number of supercurrent channels and consequently the Josephson current. Therefore, it is not far-fetched that the dependence of the Josephson current on the length and concentration of vacancies is similar to the dependence of the conduction on these parameters [38].

When a carbon atom is removed from the graphene stripe lattice, the probability of the carrier hopping from this vacancy is exponentially reduced. The results show that the same exponential reduction is reflected in Josephson's current.

Moreover, increasing the concentration of vacancies, quantum mechanically, corresponds to a greater correlation between them. This increase in correlation manifests itself in the enlargement of the exponent's coefficient α . To better illustrate this result, in Fig. 7, we present the log plot of normalized Josephson current in terms of n_x . Table 1 shows the numerical values of the localization length (which is the inverse of α). As can be seen, the localization length increases with increasing concentration of vacancies.

Table 1. Comparison of the exponent coefficient α and localization length ξ for different vacancy concentrations.

The vacancy concentration	2%	3%	5%	7%
The Coefficient (α)	0.025	0.023	0.012	0.0084
Localization length (nm)	40	43.48	83.33	119.05

We also discuss the dependence of the Josephson current on the width of ZGNS (Figure 8). Our results show that the Josephson current increases linearly with increasing the width of ZGNS. It seems that we are dealing with a quasi-classical phenomenon. If we

consider each of the longitudinal lines of the ZGNS lattice as a transport channel that connects the left and right superconductors, the increase in lattice width corresponds to a linear increase in the number of these channels.

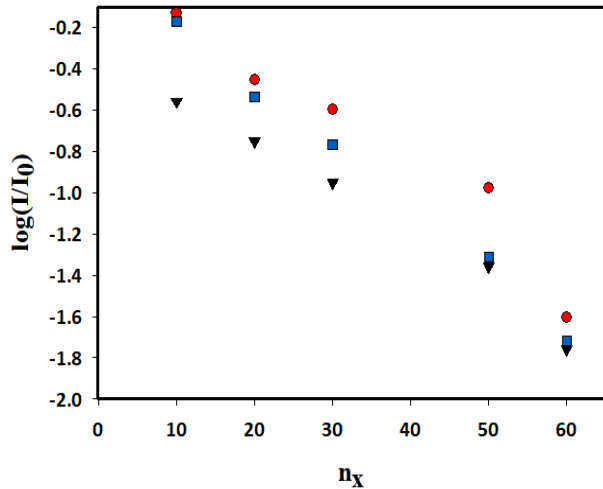


Figure 7. Plot of $\log(I/I_0)$ as function of length of ZGNS for three different concentrations of vacancy: $C=2\%$ (red circle), $C=5\%$ (blue square) and $C=7\%$ (black triangle).

This linear increasing is also observed in the normal state resistance of ZGNR [39, 40]. At very narrow widths, which are not the subject of our discussion, the effect of borders is noticeable, and this classical view does not work. But in the mesoscopic dimension of perfect graphene strips, electron transport is quasi-ballistic and is analyzed using the Landau-Büttiker formalism [41, 42]. Although the presence of vacancies changes the lattice linkages, but the linear behavior of the current with respect to the width remains true.

Now we consider divacancies which strongly disrupt the uniformity of C–C bonds around these defects in graphene lattice. When all the dangling bonds are saturated and no dangling bonds remain, in the place of these defects, two pentagons and one octagon appear instead of the previous four hexagons. In addition, the rotation of the created bonds also leads to the creation of various other polygons. Figure 9 shows schematically three types of these polygons in the graphene honeycomb lattice and their equivalents in our brick-wall lattice. Multiple DVs form an extended line of defects (ELDs). These defects can be fabricated by controlled focused electron beam irradiation [43] or

single atom resolution aberration corrected transmission electron microscopy [44].

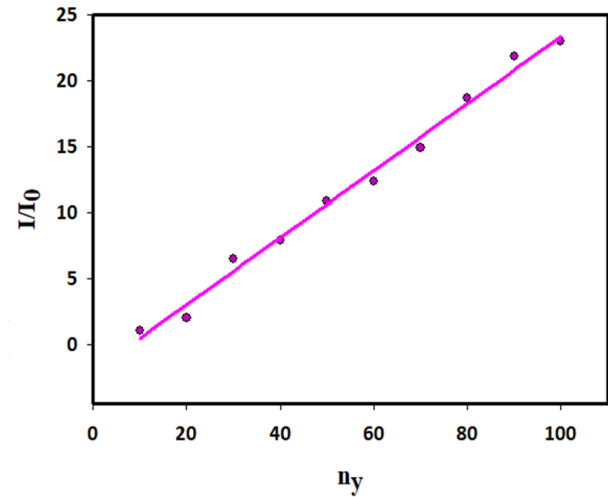


Figure 8. Normalized Josephson current vs. width of ZGNS for vacancy concentration $C=5\%$ and $n_x = 10$. The current of ZGNSs is scaled to I_0 that is the current of pristine ZGNS with the width of $n_y=10$.

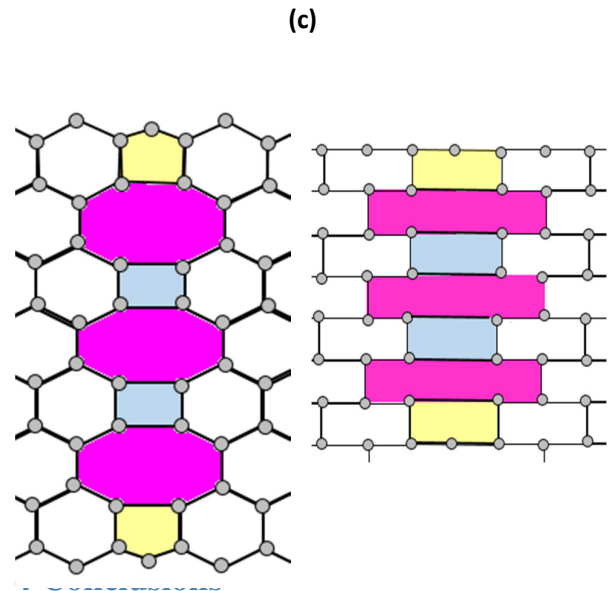
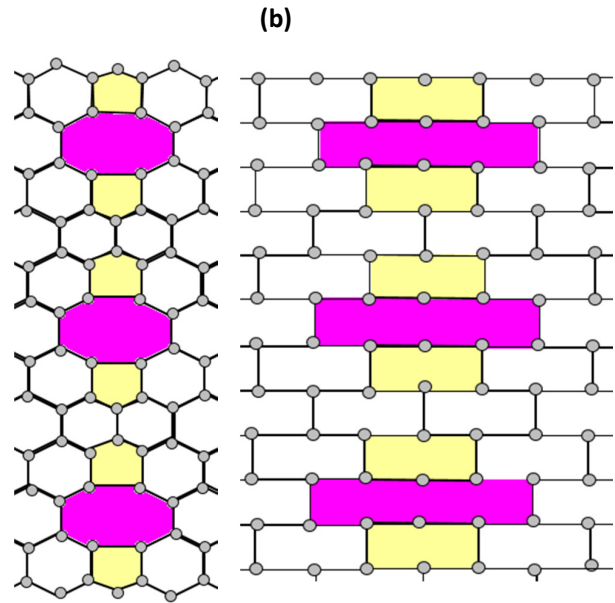
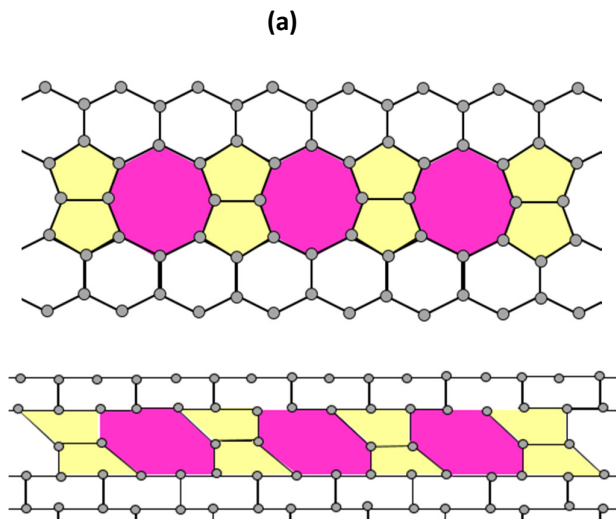
To find the relation between Josephson current and the formation of different ELDs, we have compared the Josephson current in three different ELDs with simple combination of single vacancies which place next to each other. As shown in Fig. 9, in each ELD, two neighboring atoms are removed which results in an eight-member ring in the lattice. In the first horizontal 5-8-5 ELD (Fig. 9a), the eight-member rings are on a horizontal line but in the other two vertical 5-8-5 ELD (Fig. 9b), and 4-8 ELD (Fig. 9c), the rings are all on the same vertical line. The difference between the last two is that in the vertical 5-8-5 ELD, there is a vertical C-C bond between two neighboring DV rings, but in the 4-8 ELD there is no space between the DV rings. It can be seen that the number of vacancies in each ELD is equal to the number of 8-member rings formed.

Table 2 illustrates the comparison of the Josephson current in these three ELDs and the correspondence randomly distributed SVs. The lattice is considered as $n_x=60$ and $n_y=40$ with 6 vacancies that the concentrations of the vacancies in all four configurations are the same, but the Josephson currents are very different from each other.

Using the physics, we described earlier, this difference is understandable. In the horizontal ELD, the removing of 6 carbon atom results in disconnection of only one transport channel, but in vertical ELDs, three transport channels are disjointed. Hence, we expect to have a larger Josephson current in the horizontal loop Josephson current in the horizontal loop. To compare vertical ELDs, it is necessary to pay attention to the fact that in 4-8 ELD, the vacancies are closer to each other, so the correlation between them is stronger and as a result the localization length is shorter and the current reduction due to this configuration will be greater. Calculating the current in a lattice of six holes randomly distributed in the lattice shows that the Josephson current in this case is less than the horizontal loop but more than vertical loop.

Table 2. Comparison of Josephson current of 6 vacancy defects in ZGNR lattice with $n_x=60$ and $n_y=40$ for 4 different configurations.

Defect type	Configuration	Josephson current (I/I_0)
Single vacancy	5-9	0.82
Double vacancy	horizontal 5-8-5	0.94
	vertical 5-8-5	0.3
	5-8-4-8-5	0.15



In this work, we investigate the effect of vacancy defects on the Josephson current of a Sc-ZGNS-Sc hetero structure. We found that the behavior of the Josephson current is a combination of semi classical and quantum treatments. When the width of the ZGNS increases, the semi classical part reveals as a linear increase of the Josephson current in terms the width. It seems that adding each row of lattice corresponds to adding a transport line and consequently a linear increase in Josephson current. This behavior is independent of the concentration of vacancies. However, the dependence of Josephson current to the length arises quantum mechanically from the

exponentially decaying of the hopping matrix elements and also the correlation of vacancy places. These features are confirmed in the study of the Josephson current of linear chain of divacancies. Finally, we considered the role of linear chain of divacancies which is usually formed in real samples.

Acknowledgments

S. Z. and V. D. wish to thank for financial support of the vice chancellor research and technology of Alzahra university.

Appendix A

As given in reference [27], the Green's function can be calculated separately for each region (the left superconductor, the normal region, the right superconductor). Then, the Green function of the connected system is obtained which is needed in calculating the Josephson current. By starting from the left superconductor ($j \leq 0$) which at first is not connected to the normal region (Figure 1) the Green function in the edge of the left superconductor is given by:

$$\begin{aligned}
 G_{\omega_n}(0, k; 0, k') &= \sum_{=1}^{n_{y+1}} \frac{e^{ip_{m,L}^+}}{t_h \Omega_{n,L}(n_y + 2)} \sin[q (k + 1)] \sin[q (k' + 1)] \times \begin{pmatrix} -\Omega_{n,L} - \omega_n & i\Delta_L \\ i\Delta_L & \Omega_{n,L} - \omega_n \end{pmatrix} \\
 &- \sum_{=1}^{n_{y+1}} \frac{e^{-ip_{m,L}^-}}{t_h \Omega_{n,L}(n_y + 2)} \sin[q (k + 1)] \sin[q (k' + 1)] \times \begin{pmatrix} \Omega_{n,L} - \omega_n & i\Delta_L \\ i\Delta_L & -\Omega_{n,L} - \omega_n \end{pmatrix}, \quad (5)
 \end{aligned}$$

Where $\Omega_{n,L(R)} = \sqrt{\omega_n^2 + \Delta_{L(R)}^2}$, $q_m = m\pi / (n_y + 2)$,

and $p_{m,L(R)}^\pm = \arccos[-(\mu + 2t_h \cos q_m \pm \Omega_{n,L(R)}) / 2t_h]$.

Next we separate the normal region into cells in such a way that the j th cell consists of the site (j, k) ($k=0, \dots, n_y$) and attach the cells to the left superconductor one by one, see Figure 1. Then we obtain the Green's function in normal region that is given in model and method section.

Finally we attach the right superconductor to the semi-infinite SN system. To this end we need the Green function for the right superconductor:

$$\begin{aligned}
 G_{\omega_n}(n_x + 1, k; n_x + 1, k') &= \sum_{=1}^{n_{y+1}} \frac{e^{ip_{m,R}^+}}{t_h \Omega_{n,R}(n_y + 2)} \sin[q (k + 1)] \sin[q (k' + 1)] \\
 &\times \begin{pmatrix} -\Omega_{n,R} - \omega_n & i\Delta_R e^{i\varphi} \\ i\Delta_R e^{-i\varphi} & \Omega_{n,R} - \omega_n \end{pmatrix} \\
 &- \sum_{=1}^{n_{y+1}} \frac{e^{-ip_{m,R}^-}}{t_h \Omega_{n,R}(n_y + 2)} \sin[q (k + 1)] \sin[q (k' + 1)] \\
 &\times \begin{pmatrix} \Omega_{n,R} - \omega_n & i\Delta_R e^{i\varphi} \\ i\Delta_R e^{-i\varphi} & -\Omega_{n,R} - \omega_n \end{pmatrix}. \quad (6)
 \end{aligned}$$

Then the Green function of the connected system which we need in calculating the Josephson current is obtained from the following two equations:

$$\begin{aligned}
 G_{\omega_n}(n_x, k; n_x + 1, k') &= \sum_{k'=0}^{n_y} \{ [G_{\omega_n}(n_x, k; n_x, k')]^{-1} \\
 &- H' G_{\omega_n}(n_x + 1, k; n_x + 1, k') H' \}^{-1} \times H' \\
 &\times G_{\omega_n}(n_x + 1, k; n_x + 1, k'), \quad (7)
 \end{aligned}$$

$$\begin{aligned}
 G_{\omega_n}(n_x + 1, k; n_x, k') &= \sum_{k'=0}^{n_y} G_{\omega_n}(n_x + 1, k; n_x + 1, k') \\
 &\times H' \{ [G_{\omega_n}(n_x, k; n_x, k')]^{-1} \\
 &- H' G_{\omega_n}(n_x + 1, k; n_x + 1, k') H' \}^{-1}. \quad (8)
 \end{aligned}$$

The Josephson current is calculated from Eqs. (2), (7), and (8).

References

- [1] A.K. Geim, "Graphene: Status and Prospects." *Science*, **324** (2009) 1530.
- [2] Marks, M.C. Hersam, "Carbon nanomaterials for electronics, optoelectronics, photovoltaics, and sensing." *Chemical Society Reviews*, **42** (2013) 2824.

- [3] Y. Zhu , et al, "Graphene and Graphene Oxide: Synthesis, Properties, and Applications." *Advanced Materials*, **22** (2010) 3906.
- [4] A.K. Geim, K.S. Novoselov, "The rise of graphene." *Nature Materials*, **6** (2007) 183.
- [5] A.H. Castro Neto, F. Guinea, N.M. R. Peres, K.S. Novoselov, and A.K. Geim, "The electronic properties of graphene." *Reviews of Modern Physics*, **81** (2009) 109.
- [6] C.W. J. Beenakker, M. Titov , "Josephson effect in ballistic graphene." *Physical Review B*, **74** (2006) 041401.
- [7] C. Ojeda-Aristizabal, M. Ferrier, S. Guéron, and H. Bouchiat, "Tuning the proximity effect in a superconductor-graphene-superconductor junction." *Physical Review B*, **79** (2009) 165436.
- [8] M. Wilson, "Electrons in atomically thin carbon sheets behave like massless particles." *Physics Today*, **59** (2006)21.
- [9] V. Eswaraiyah, et al, "Top down method for synthesis of highly conducting graphene by exfoliation of graphite oxide using focused solar radiation." *Journal of Materials Chemistry*, **21** (2011) 6800.
- [10] L. Tang, et al, "Bottom-up synthesis of large-scale graphene oxide nanosheets/" *Journal of Materials Chemistry*, **22** (2012) 5676.
- [11] Y. Kim, J. Ihm, E.Yoon, G.D. Lee, "Dynamics and stability of divacancy defects in graphene." *Physical Review B*, **84** (2011) 075445.
- [12] J. Kotakoski, A.V. Krasheninnikov, U. Kaiser, and J.C. Meyer, "From Point Defects in Graphene to Two-Dimensional Amorphous Carbon." *Physical Review Letters*, **106** (2011) 105505.
- [13] A. Hashimoto, K. Suenaga, A. Gloter, K. Urita, S. Iijima, "Direct evidence for atomic defects in graphene layers." *Nature*, **430** (2004) 870.
- [14] K. Brenner, R. Murali, "In situ doping of graphene by exfoliation in a nitrogen ambient." *Applied Physics Letters*, **98** (2011) 13115.
- [15] C. Zhang, L. Fu, N. Liu, M. Liu, Y. Wang, Z. Liu, "Synthesis of Nitrogen□Doped Graphene Using Embedded Carbon and Nitrogen Sources." *Advanced Materials*, **23** (2011) 1020.
- [16] L. Li, S. Reich, J. Robertson, "Defect energies of graphite: Density-functional calculations." *Physical Review B*, **72** (2005) 184109.
- [17] C. Ataca, E. Akturk, H. Şahin, S. Ciraci, "Adsorption of carbon adatoms to graphene and its nanoribbons." *Journal of Applied Physics*, **109** (2011) 013704.
- [18] M. Terrones, A.R. Botello-Méndez, J. Campos-Delgado, F. López-Urías, Y.I. Vega-Cantú, F.J. Rodríguez-Macías, A.L. Elias, E. Munoz-Sandoval, A.G. Cano-Marquez, J. Charlier, "Graphene and graphite nanoribbons: Morphology, properties, synthesis, defects and applications." *Nano Today*, **5** (2010) 351.
- [19] P.T. Araujo, M. Terrones, M.S. Dresselhaus, "Defects and impurities in graphene-like materials." *Materials Today*, **15** (2012) 98.
- [20] C.Ö. Girit, et al, "Graphene at the Edge: Stability and Dynamics." *Science*, **323** (2009) 1705.
- [21] M.M. Ugeda, I. Brihuega, F. Guinea, J.M. Gómez-Rodríguez, "Missing Atom as a Source of Carbon Magnetism." *Physical Review Letters*, **104** (2010) 096804.
- [22] Y. Wang, Y. Wu, "Disorder enhanced conductance in graphene." *Physica B*, **478** (2015) 84.
- [23] L. Nanshu, Z. Si, Z. Jijun, "Electrical Conductance of Graphene with Point Defects." *Acta Physico-Chimica Sinica*, **35** (2018) 1142.
- [24] W.A. Muñoz, L. Covaci and F.M. Peeters, "Disordered graphene Josephson junctions." *Physical Review B*, **91** (2015) 054506.
- [25] M. Gokhan Sensoy, "The influence of vacancy-induced local strain on the transport properties in armchair and zigzag graphene nanoribbons."

- Materials Research Express, **6** (2019) 045057.
- [26] S. Zareei, V. Daadmehr, H. Hakimipajouh, Z. Faraei, "Josephson current for a Graphene nanoribbon using a lattice model. Interfaces, Thin films, and Low dimensional systems, **2** (2019) 113.
- [27] A. Furusaki, "DC Josephson effect in dirty SNS junctions: Numerical study." *Physica B: Condensed Matter*, **203** (1994) 214.
- [28] W. Hou, J.M. Chen, "Hidden symmetry and protection of Dirac points on the honeycomb lattice." *Scientific Reports*, **5** (2014) 17571.
- [29] K. Wakabayashi, M. Fujita, H. Ajiki and M. Sigrist, "Electronic and magnetic properties of nanographite ribbons." *Physical Review B*, **59** (1999) 8271.
- [30] Y. Asano, "Numerical method for dc Josephson current between d-wave superconductors," *Physical Review B*, **63** (2001) 052512.
- [31] M.P. López Sancho, J.M. Rubio, "Quick iterative scheme for the calculation of transfer matrices: application to Mo (100)." *Journal of Physics F: Metal Physics*, **14** (1984) 1205.
- [32] A.V. Krasheninnikov, P.O. Lehtinen, A.S. Foster, R.M. Nieminen, "Bending the vacancy energetics and migration in graphite and carbon nanotubes." *Chemical Physics Letter*, **418** (2006) 1205.
- [33] A.A. El-Barbary, R.H. Telling, C.P. Ewels, M.I. Heggie, P.R. Briddon, "Structure and energetics of the vacancy in graphite." *Physical Review B*, **68** (2003) 144107.
- [34] F. Banhart, J. Kotakoski, A.V. Krasheninnikov, "Structural Defects in Graphene." *ACS Nano*, **5** (2011) 26.
- [35] C.W.J. Beenakker, "Specular Andreev Reflection in Graphene." *Physical Review Letters*, **97** (2006) 067007.
- [36] G. Nanda, et al., "Current-Phase Relation of Ballistic Graphene Josephson Junctions." *Nano Letters*, **17** (2017) 3396.
- [37] A.M. Black-Schaffer and S. Doniach, "Self-consistent solution for proximity effect and Josephson current in ballistic graphene SNS Josephson junctions." *Physical Review B*, **78** (2008) 024504.
- [38] effect on the electronic transport of zigzag graphene nanoribbon using recursive Green's function." *Computational Materials Science*, **101** (2015) 156.
- [39] Z. Chen, Y. Lin, M.J. Rooks, P. Avouris, "Graphene Nano-Ribbon Electronics." *Physica E*, **40** (2007) 228.
- [40] Z. Xiao, C. Durkan, "Unravelling the electrical properties of epitaxial Graphene nanoribbons." *Advanced Materials Interfaces*, **6** (2019) 1801794.
- [41] M. time: Effective area in magnetically induced interference." *Physical Review B*, **36** (1987) 6255.
- [42] C. Durkan, *Current at the nanoscale: An introduction to nanoelectronics*, second edition, World Scientific Publishing Company (2013).
- [43] J.H. Warner, G. Do Lee, K. within Extended Arm Chair Defects in Graphene." *ACS Nano*, **7** (2013) 9860.
- [44] A.W. Robertson, G. Allen, "Partial dislocations in graphene and their atomic level migration dynamics." *Nano letters*, **15** (2015) 5950.



Optimization of electron scattering from random potential barriers on the surface of topological insulators

Scientific research paper

Hamid Dehnavi¹, Mehdi Saadat^{2*}

¹*Department of Physics, North Tehran Branch, Islamic Azad University, Tehran, Iran*

²*Department of Physics, Shahid Rajaei Teacher Training University, Tehran, Iran*

ARTICLE INFO

Article history:

Received 14 December 2021

Revised 9 January 2022

Accepted 13 January 2022

Available online 27 January 2022

Keywords:

Topological insulators
Random potentials,
Transmission coefficient
Conduction
Potential barriers

ABSTRACT

Optimization of electron scattering has been investigated using random potential barriers. Random potential barriers can be defined in two situations. In the first case when line defects are placed regularly on the surface of the topological insulator, but their strength changes randomly. In the second case when the potential barriers strength are constant while location of line defects on the surface of the topological insulator are changing randomly. To obtain better results, probability of transmission in the random potential states are calculated N times. These N values are averaged and the result is compared with the probability of transmission in the regular case. It seems that, in propagating of incident electrons for some amounts of incident energy, number of defects, strength of potential, even direction of propagation, the results are close to the values obtained for the regular case. For some amounts of incident energy or some structural parameters significant differences are seen. We encounter large variation in electrical conduction, when the location of potential barriers change randomly, relative to the case that strength of random potential is changed. In fact, the reason for higher electrical conductivity is the constructive interference that occurs between propagating electron waves. Therefore, in the presence of such random potential barriers, the conduction and transmission of incident electrons have been improved.

1 Introduction

Recently, a new quantum behavior in the field of condensed matter physics and materials science has attracted much attention. The materials in which this strange behavior is observed are known as topological insulators [1], [2]. These materials with surface states with and without energy gap in the bulk of insulation result from a strong spin-orbit interaction and time-reversal symmetry [3], [4], [5], [6]. In other words, the superficial states of conduction are maintained in such

materials as long as the time-reversal symmetry is not broken [7], [8], [9].

Impurities on the surface of topological insulators cause scattering of the wave function showing interesting electronic properties [10], [11], [12], [13]. Impurities in fact, in the presence of an electric field and a spin-orbit coupling, cause electron scattering. This effect has been observed experimentally in thin layers of GaAs and InGaAs [14]. Impurities also deform the 3D Dirac cone in Bi_2Se_3 [13]. In other words, magnetic impurities can create a local energy

*Corresponding author.

Email address: Saadat@sru.ac.ir

DOI: 10.22051/jitl.2022.38844.1064

gap by suppressing the local state density and inducing an interaction RKKY (Ruderman, Kittel, Kasuya, Yosida) in the system [10], [11].

Surface defects and ripples in topological insulators can also scatter Dirac electrons. Bismuth-based topological insulators such as Bi_2Te_3 and Bi_2Se_3 [15] are inexpensive materials that have excellent electrical conductivity on their surfaces [16], [17]. Okada et al. [18] created a series of local ripples on the surface of Bi_2Te_3 . They proposed 2D defects to control the properties of Dirac fermions in topological insulators. Such local ripples can be created by periodic buckling during sample growth or by chain induction through a piezoelectric crystal [18].

One-dimensional periodic potentials on the surface of these materials are responsible for trapping surface electrons and displacing energy levels. In this case, regular linear defects (local ripples) are modeled by the delta-function potential [19], [21]. Using an approach of quantum mechanics, Ting and An investigated the scattering of surface states of a single potential barrier in Bi_2Te_3 by the hexagonal warping effects [20]. They showed that, passing of the incident electrons under certain conditions when line defect is along ΓM can be perfect, and since there is a limited possibility for the reflection of electrons, when the incident wave has a component along ΓK its Fermi energy increases. The warping parameter plays an important role in changing the constant energy contour (CEC) from a circle to a hexagon and then to a snowflake shape with sharp corners. The torsion of the CEC is modulated by an external magnetic field [22], [23]. However, at high energies, where the warping effect is strong, it may significantly increase the electrical conductivity and thus the induction passage channels shown by the CEC snowflake shape [23]. The influence of the local delta-function potentials in two and three dimensions along the ΓK on the transmission of incident electrons in Bi_2Te_3 has been reported [19]. We have also reported up to 20 barriers in both directions ΓK and ΓM in our previous work [24]. The results show that the electrical conductivity fluctuations with strong delta-function potential and that the electronic transmission on the surface of topological insulator can be controlled by structural parameters.

In this paper, we try to investigate electronic transmission on the surface of a topological insulator in presence of random ripples. We consider a series of line defects with values of random strength and random distance from each other in two directions ΓK and ΓM . The transmission coefficients as well as the conductivity of the incident electrons are calculated for different structural parameters such as: number of potential barriers, strength of potential, distance of barriers, and the energy of the incident electron in two modes. At first the strength of potential barriers and then location of potential barriers varies randomly. In each case we obtain the values of transmission coefficients and conduction N times, then we calculate the mean values, and finally the results are compared to the cases in which the ripples were regular.

2 Method

We consider 3D topological insulator Bi_2Te_3 with strong warping effect and Dirac cone on the surface. By adjusting the Fermi level of the surface states, we can avoid the interaction between the surface and volume states [25]. Single particle Hamiltonian for surface electrons with torsional hexagonal states can be expressed as follows:

$$H(p_x, p_y) = v(p_x \sigma_y - p_y \sigma_x) + \lambda(p_x^3 - 3p_x p_y^2) \sigma_z, \quad (1)$$

since $p_x = -i\hbar \partial_x$ and $p_y = -i\hbar \partial_y$ are the 2D momentum operators of surface electrons, and σ_j ($j = x, y, z$) are the Pauli matrices. $v = 2.55 \text{ eV} \cdot \text{\AA}$ is the Fermi velocity and $\lambda = 250 \text{ eV} \cdot \text{\AA}^3$ is the warping parameters [25], [26]. For a more physical expression of the electron wave function propagated in the $\Gamma K(x)$ direction, we express it as follows:

$$\tilde{\psi}_k(\vec{r}) = \frac{1}{\sqrt{|v_x(\vec{k})|}} \psi_k(\vec{r}) \quad (2)$$

where $\psi_k(\vec{r})$ is the eigenstate of the Hamiltonian expressed by Eq. (1) and $v_x(\vec{k})$ is the electron group velocity along the x-axis [20], [24].

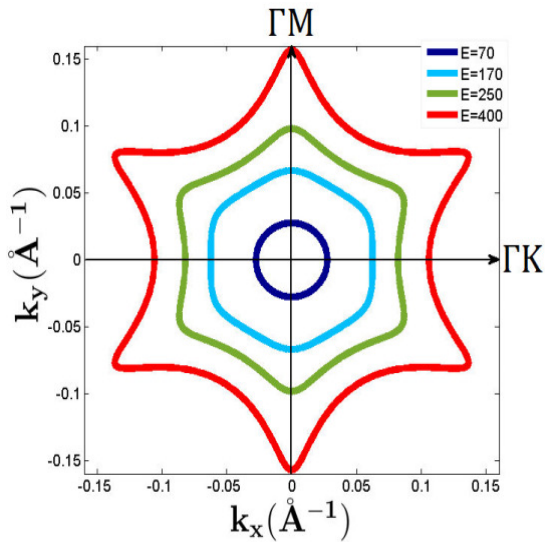


Figure 1. Fixed energy contours are displayed in the plane $k_x - k_y$ for energies (70, 170, 250, and 400) meV.

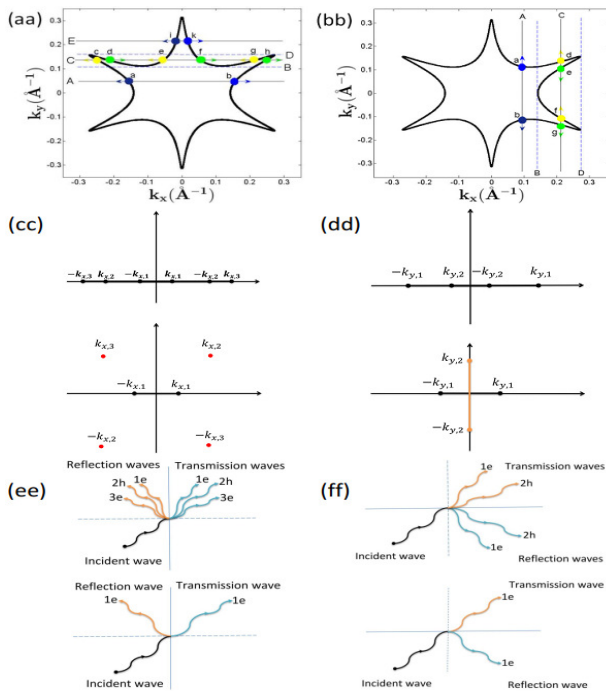


Figure 2. The roots are investigated in two states on a constant energy contour when the contour is hexagonal. The diagrams (aa), (cc), and (ee) show six roots. In the diagrams (bb), (dd), and (ff) four roots are shown [20].

Figure 2, the CEC snowflake states show the points more clearly on it; the amount of Fermi energy has been taken very large. In diagram (2aa), as we can see, the direction of wave motion is considered in the

direction of the momentum k_x , lines A and E intersect the energy contour at only two points (a,b) or (i,k), which shows that for values of k_y according to diagram (2aa) we will have only two real roots and four mixed roots. For certain values of k_y that this range is marked on CEC using dashes B and D, the line C intersects the contour at six points (c,d, e,f,g,h) which shows that the energy equation in k_x direction has six real roots for specific values of k_y . Graph (2cc) shows the state of six real roots and two real roots in the $k_x - k_y$ plane. In diagram (2ee), schematically, the case where we have two real roots in which the incident wave according to diagram (2aa) has a certain k_y momentum, scattered by a defect, we have a reflected wave and a transmission wave. In the case that we have six real roots, the incident electron wave has a certain amount of momentum k_y as shown in diagram (2aa), scattered by a defect, we have three reflected waves and three passing waves. In diagram (2bb), in which the direction of motion of the incident electron wave is in the k_y direction, for values of k_x (zero momentum value is indicated by the dashed line B) line A intersects the CEC at only two points, which shows that the energy equation in terms of k_y has only two real roots and two purely imaginary roots. The range of momentum is shown in diagram (2bb) by the dashed lines B and D, line C intersects the CEC at four points (d,e,f,g), which shows that the energy equation has four real roots. Diagram (2dd) shows the state of four real roots and two real real roots on the $k_x - k_y$ plane. Diagram (2ff) schematically shows the incident electron wave has had a specific motion according to diagram (2bb), when an electron encountered a defect on the surface of insulator in the k_x direction, it will have only one reflected wave and one transmission wave. If the incident wave according to diagram (2bb) has had a momentum k_x in the range between the dashed lines B and D, we will have two reflected waves and two transmitted waves. According to the shapes (2cc) and (2dd) the roots have positive and negative pairs. When all the roots are real, according to the diagrams (2ee) and (2ff) a wave travels in directions k_x and k_y in the a holelike form [24].

3 A SUPERLATTICE ALONG $\Gamma K(x)$ or $\Gamma M(y)$

Here ripply structures include N delta-function potential with random potential strength and random distance from each other on the surface of topological insulator Bi_2Te_3 , along X or Y axis. The wave function of electron in the region $(n-1)d < x < nd$, is the eigenstate of equation $\{H(-i\partial_x, k_y) + \sum_{n=0}^{N-1} U\delta(x-nd)\}\psi_k^{(n)}(\vec{r}) = E\psi_k^{(n)}(\vec{r})$. Because of this, the eigenvalue equation is a third-order partial differential equation relative to x , so we will have three boundary conditions [20], [24]. After applying the boundary conditions on the wave function and using the 6×6 transfer matrix, the relationship between the n^{th} coefficient and the $(n+1)^{th}$ coefficient is obtained [24].

Note that the Hamiltonian is not symmetric under transformation $p_x \leftrightarrow p_y$, therefore, the electron wave function in the region $(n-1)d < y < nd$, is an eigenstate of a second-order partial differential equation relative to y : $\{H(k_x, -i\partial_y) + \sum_{n=0}^{N-1} U\delta(y-nd)\}\psi_k^{(n)}(\vec{r}) = E\psi_k^{(n)}(\vec{r})$, so two boundary conditions will be obtained [20], [24]. By applying boundary conditions to the wave function, a 4×4 transfer matrix is obtained, which relates the n^{th} coefficient to the $(n+1)^{th}$ coefficient [24]. According to Fig. 2, if all roots are real, the transmission coefficient T is the sum of $|t|^2$'s. If two roots are real, the transmission coefficient T is only $|t_1|^2$ [20]. In the case of N barriers, when the potential strength is random, every one receives a random value in the range $(U \pm 0.1)eV \cdot \text{\AA}$, then the transmission coefficient is calculated. This operation is repeated N times and N values are obtained for the transmission coefficients before averaging the values. Also when the distances between potential barriers are random, in each calculation, location of barriers receives arandom values in the range $(d \pm 0.1)\text{\AA}$. This operation can be repeated few times to obtain few transmission coefficients. Averaging these values we draw the transmission coefficient diagram in terms of $d(\text{\AA})$ or $U(eV \cdot \text{\AA})$. We observe fluctuations in the transmission diagram and that we can compare it with the transmission diagram of a regular superlattice. The following equation is used to calculate $\bar{T}(E, \theta)$:

$$\bar{T}(E, \theta) = \frac{1}{N} \sum_i^N T(E, \theta) \quad (3)$$

To calculate the electrical conductivity of topological insulators in the $\Gamma K(x)$ direction, potential strength of each N barriers or the distance of the barriers are random values in the range $(U \pm 0.1)eV \cdot \text{\AA}$ and $(d \pm 0.1)\text{\AA}$. This operation can be repeated few times before averaging the obtained values for electrical conductivity. The following equations are used to calculate the electrical conductivity and its average [19]:

$$G/G_0 = \int_0^{\pi/2} T(E, \theta) \cos\theta d\theta \quad (4)$$

$$\overline{G/G_0} = \frac{1}{N} \sum_i^N G/G_0 \quad (5)$$

where $\theta = \arctan(k_y/k_x)$ indicates the angle of incident electron and G_0 is a constant.

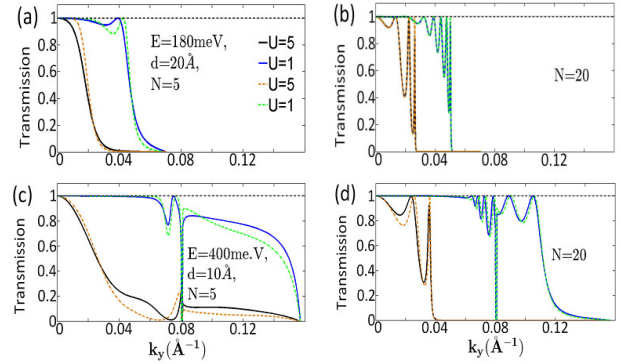


Figure 3: Transmission coefficients in terms of momentum k_y . Ripples are parallel to x axes while N is the number of them distributed randomly in direction y .

4 Results and discussion

In Fig. 3 the lattice constant d in diagrams (a) and (b) is a random value in range $(20 \pm 0.1)\text{\AA}$ in solid line curves, and a constant value, 20\AA for dashed line curves. The lattice constant d in diagrams (c) and (d) is a random value in the range $(10 \pm 0.1)\text{\AA}$ for solid curves and a constant value, 10\AA for dashed line curves. In diagrams (a) and (b) the incident electron energy is 180meV and 400meV in diagrams (c) and (d). The number of line defects in diagrams (a) and (c) is $N=5$ and $N=20$ in diagrams (b) and (d). Dependence of energy and wave number of the incident electron in transmission through the line defects with random

lattice constant in Bi_2Te_3 , plotted in Fig. 3. The transmission coefficient in terms of k_y at two incident energies $E = 180\text{meV}$ and $E = 400\text{meV}$ for 5 and 20 barriers expanded along the y -direction are shown. Location of potential barriers takes a random value in the range $(20 \pm 0.1)\text{\AA}$ in diagrams (3a) and (3b) and takes a random value in range $(10 \pm 0.1)\text{\AA}$ in diagrams (3c) and (3d). Each point of the solid black lines with $(U = 5\text{eV.\AA})$, and blue $(U = 1\text{eV.\AA})$ are obtained 50 times, averaging these values leads to \bar{T} which is shown in the diagrams. The values of T in the dashed line diagrams of Fig. 3, with the same potential strength $(1.5)\text{eV.\AA}$, are plotted in diagrams (3a), (3b) for lattice constant $d = 20\text{\AA}$ and in diagrams (3c), (3d) for lattice constant 10\AA . In this figure for a smaller number of barriers there is more difference between \bar{T} and T , because with increasing the number of barriers, the random values increase and as a result, the mean value is averaged with more numbers, which bring it closer to a fixed value. By increasing the incident energy for less number of barriers, the average values show a better transmission coefficient than the fixed transmission values. The reason is due to the constructive interference modes [28], caused by the random spacing of the barriers. At the peaks of the transmission coefficient curves, the conditions for the transmission of electrons in the steady state are better seen.

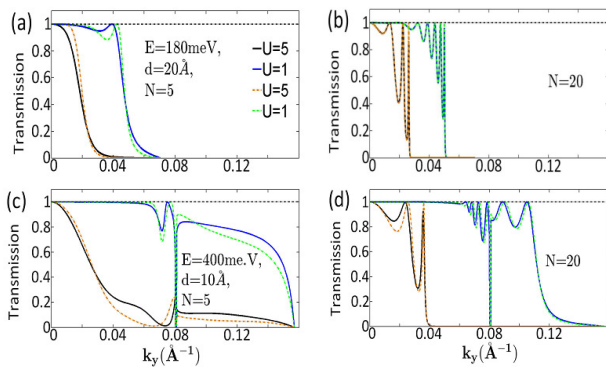


Figure 4: Transmission coefficients in terms of momentum k_x . Ripples are parallel to the y axes while N is the number of them, distributed randomly in direction x . Because in the random mode, destructive interference takes place between the transmitted and reflected waves.

In Fig. 4 the distance of potential barriers in solid curves is in the range $(10 \pm 0.1)\text{\AA}$. For dashed line

curves the constant value is 10\AA . The number of barriers in diagrams (a) and (c) are $N = 5$ and in diagrams (b) and (d) are $N = 20$. The potential strength of solid line and dashed line curves is $(1,5)\text{eV.\AA}$. Incident energy of electron in diagrams (a) and (b) is $E = 170\text{meV}$ and in diagrams (c) and (d) is 250meV . In Fig. 4 line defects were extended along the x -direction. As it is shown in the diagrams, transmission coefficients in the random lattice constant case and regular lattice constant case are plotted in terms of k_x at two incident energy, one less than the critical limit $E = 170\text{meV} (< 180\text{meV})$ and the other more than the critical limit $E = 250\text{meV}$. Like Fig. 3, the lattice constant d selects random values in the range $(10 \pm 0.1)\text{\AA}$. Note that the incident electron moves in the direction y , so for low and high energies and two barriers, there is a little difference between T and \bar{T} in graph (d) for $U = 1\text{eV.\AA}$ except at the peaks. This slight difference may be due to the fact that the sharp peaks became smooth in the averaging process. In diagram (4a) since the peaks are not sharp, there is no noticeable difference between the averaged transmission coefficient in the random case and the transmission coefficient in the regular case. While in diagrams (4b) and (4d) where $U = 5\text{eV.\AA}$ there are more sharp peaks that have been averaged that lead to correct transmission coefficients. In diagram (4d), where the potential strength is $U = 1\text{eV.\AA}$ after averaging, a significant decrease can be seen in the transmission coefficient relative to the regular case which is due to non-constructive interference modes. For more number of barriers, diagrams (4b) and (4d), with increasing number of peaks, we see a decrease in the average amount of transmission coefficient at the same peak.

By comparing Figs. 3 and 4, we see that, amount of transmission coefficient through random defects is strongly dependent on the direction in which they are located. In Fig. 4, random values of the lattice constants (distance between potential barriers) that lead to the average value of \bar{T} have less influence than T due to regular superlattice except for diagram (4d) with $U = 1\text{eV.\AA}$ which is an exception. In Fig. 3 this effect is more visible, which is due to the properties of electrons transmitting through the line defects in the x and y directions. Source of these differences are in

their boundary conditions and also Hamiltonian asymmetry under the transformation $k_x \leftrightarrow k_y$ [24].

Figure 5, the potential strength of solid line curves are in the range $(5 \pm 0.1)eV.\text{\AA}$ while for dashed line curves, the of potential height of barriers is $5eV.\text{\AA}$. The distance between potential barriers for solid line and dashed line curves is $(10,20)\text{\AA}$. The energy of the incident electron in diagrams (a) and (b) is 180meV and in diagrams (c) and (d) is 400meV . Number of potential barriers, which is in the y -direction, in diagrams (a) and (c) are $N=5$ and in diagrams (b) and (d) are $N=20$.

Figure 6 potential barriers are in the x -direction, there are two categories of solid line and dashed line graphs. The heights of random potential barriers are in range $(5 \pm 0.1)eV.\text{\AA}$ while the height of regular potential barriers is $5eV.\text{\AA}$. The distance between potential barriers for both categories of curves is $(10,15)\text{\AA}$. In diagrams (a) and (b) energy of the incident electron is 170meV and in diagrams (c) and (d) is 250meV . The number of defect lines in diagrams (a) and (c) are $N=5$ and in diagrams (b) and (d) are $N=20$.

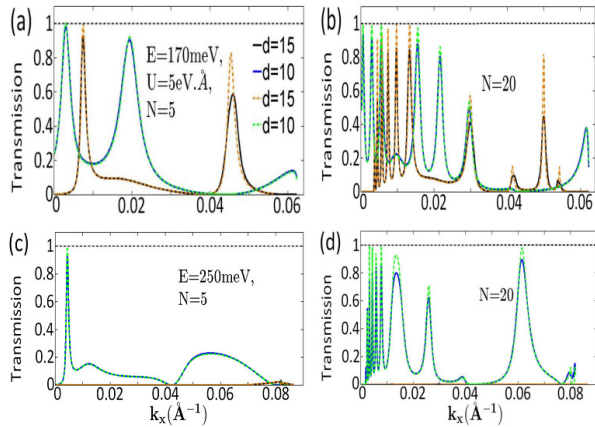


Figure 5: The transmission coefficient for barriers of random height. Ripples are parallel to x axes and N is the number of them in direction y .

In Figs. 5 and 6 instead of random distance between barriers, we have selected the strength of potential barriers randomly. In Fig. 5 we consider the random potential barriers in the y -direction. Transmission coefficient in terms of k_y are plotted for two set of curves in each graph. Solid curves which are the mean transmission coefficient have been calculated using random values for potential strength in range $U = (5 \pm$

$0.1)eV.\text{\AA}$ and dashed line curves are transmission coefficient using a fixed value $U = 5eV.\text{\AA}$ for barriers height. In both cases distance between barriers are $(10,20)\text{\AA}$. At incident energies lower than critical limits, by reducing the distance between potential barriers from 20\AA to 10\AA , the difference of mean value of transmission coefficients \bar{T} , and T increase. But at higher incident energies the difference between \bar{T} and T decreases. Specially in the case that the number of barriers increases, the difference in the transmission peaks is obvious, which can be due to the constructive interference of transmitted and reflected electron waves. Dependence of incident energy and spatial distance between the superlattice line defects in Bi_2Te_3 are plotted in Fig. 6 for random and fixed potential strengths.

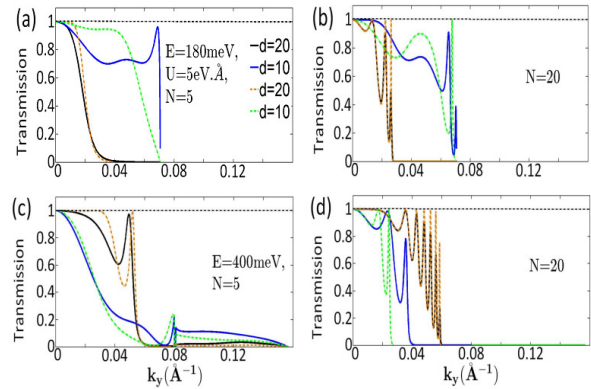


Figure 6. The transmission coefficient for barriers of random height. Ripples are parallel to the y axes while N is the number of them in direction x .

Transmission coefficients in terms of k_x for two incident energies $E = 170\text{meV} (< E_c)$ and $E = 250\text{meV} (> E_c)$ are shown for $N = 5$ and $N = 20$ line defects extended along the x -direction. The amount of potential strength that each barrier selects randomly is in the range of $(5 \pm 0.1)eV.\text{\AA}$. Solid curves show the mean value of the transmission coefficient, \bar{T} , and dashed line curves show the value of the transmission coefficient of regular superlattice, T , for two fixed lattice constant $(10,15)\text{\AA}$. When electron waves propagate in the x -direction, the difference between \bar{T} and T is in sharp peaks. For low number of barriers of (graphs (6a) and (6c)) the difference between \bar{T} and T decreases with increasing incident electron energy. Also for more number of defect lines (graph (6b) and

(6d)) transmission coefficients decrease with increasing of the incident electron energy which leads to sharp peaks. This small difference, is due to low effect of random potential strength on the interference modes. Solid line curves are mean values of electrical conductivity for random barriers in terms of distance between barriers and potential strength while dashed line curves are electrical conductivity for regular superlattice. Diagram (a) is the mean value of the electrical conductivity for random potential strength in the range $(5 \pm 0.1)eV \cdot \text{\AA}$, and the dashed line curve is electrical conductivity for fixed value $U = 5eV \cdot \text{\AA}$. Diagram (b) is the mean value of the electrical conductivity for random distance between barriers in range $(10 \pm 0.1)\text{\AA}$ and dashed line curve is electrical conductivity for fixed value $d = 10\text{\AA}$. The incident energies for both categories in black and blue curves are 180meV and 400meV respectively.

On the surface of topological insulators, electrical conductivity can be checked by the movement of Fermi electrons. In Fig. 7, electrical conductivity calculated for $N = 5$, extended in y-direction where N is number of line defects. In this figure each point of graphs in Fig. 7 is the mean value of 50 calculation for random input variables. In diagram (7a) for 400meV incident electron energy, there is very little difference between the mean values of electrical conductivity in the random case, $\overline{\frac{G}{G_0}}$, and its counterpart in regular superlattice, $\frac{G}{G_0}$. In Fig. 7a at 180meV incident electron energy, for those values of d which is nearly less than 10\AA there is a large difference between the electrical conductivities in random and regular cases. After 10\AA , there is no difference between these two values, because of interference of different modes. In diagram (7b), in solid line curves where the strength of potential barriers are random, electrical conductivity has a large difference with its counterpart in regular case, plotted by dashes line curves. Electrical conductivity in averaged mode, at least in a wide range of U is larger than electrical conductivity in regular superlattice. This behavior is due to the constructive interference of modes, caused by random distance between barriers. There are well-defined peaks which decrease and increase with increasing the thickness of the central layer of the structure. This behavior is a result of resonant tunneling through structure and

quantum-well states formed in the central layer [29], [30], [31], [32].

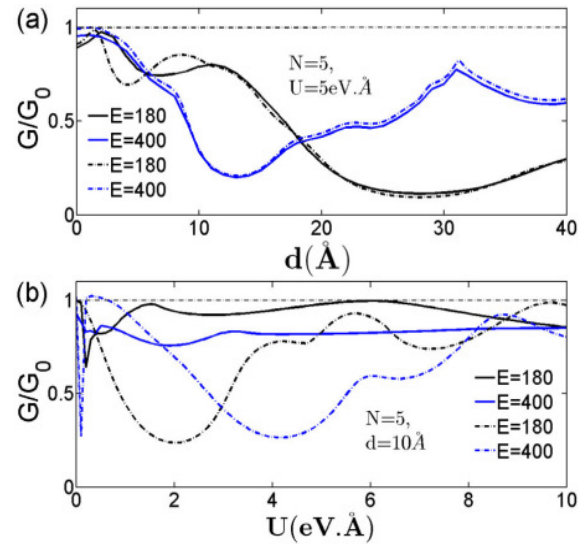


Figure 7. Diagram (a) is Electrical conductivity in terms of distance between barriers and diagram (b) is Electrical conductivity in terms of potential strength.

4 Conclusions

In summary, we compared transmission coefficients and electrical conductivities of two cases: random potential include potential strength and lattice constant, with regular superlattice. In both cases we used the Dirac delta-function form for potential barriers. By changing the structural parameters such as, potential heights, distance between barriers, energy of incident electrons, and direction of incident electrons significant differences are seen in the transmission coefficients and electrical conductivity for random and regular cases. Generally, randomness of potential and interfering between the transmitted and reflected electron waves are responsible for these behaviors. In electrical conductivity, there are more differences between the averaged values of random superlattice and fixed values of regular superlattice. In a situation where the lattice constant is random, the mean value of electrical conductivity is higher than its counterpart with fixed lattice constant. This suggests that random potentials can be closer to the real behavior of surface conduction in the Bi_2Te_3 topological insulator. Therefore, by creating random potential barriers, the electrical conductivity of incident electrons is

improved. Defect resonance modes have been reported by STM (scanning tunneling microscopy) for incident energies less than 200meV above the Dirac point surface [12], [33], [34]. This formalism can be generalized to the infinite random potential barrier on the surface of these insulators.

References

- [1] X. Qi, S. Zhang, "Topological Insulators and Superconductors." *Reviews of Modern Physics*, **83** (2011) 1057.
- [2] X. Qi, S. Zhang, "The Quantum Spin Hall Effect and Topological Insulators." *Physics Today*, **63** (2010) 33.
- [3] L. Fu, C.L. Kane, "Topological Insulators with Inversion Symmetry." *Physical Review B*, **76** (2007) 045302.
- [4] L. Fu, C. L. Kane, E. J. Mele, "Topological Insulators in Three Dimensions." *Physical Review Letters*, **98** (2007) 106803.
- [5] C. L. Kane, E. J. Mele, "Z₂ Topological Order and the Quantum Spin Hall Effect." *Physical Review Letters*, **95** (2005) 146802.
- [6] C. L. Kane, E.J. Mele, "Hall and Spin Hall Viscosity in 2D Topological Systems." *Physical Review Letters*, **95** (2005) 146801.
- [7] N. Nagaosa, "A New State of Quantum Matter." *Science*, **318** (2007) 758.
- [8] J.E. Moore, L. Balents, "Topological Invariants of TimeReversal-Invariant Band Structures." *Physical Review B*, **75** (2007) 121306(R).
- [9] J.E. Moore, "Topological insulators: The Next Generation." *Nature Physics*, **5** (2009) 375.
- [10] Q. Liu, C-X. Liu, C. Xu, X-L. Qi, S.C. Zhang, "Magnetic Impurities on the Surface of a Topological Insulator." *Physical Review Letters*, **102** (2009) 156603.
- [11] A.A. Zyuzin, D. Loss, "RKKY Interaction on Surfaces of Topological Insulators with Superconducting Proximity Effect." *Physical Review B*, **90** (2014) 125443.
- [12] Y. Xu, J. Chiu, L. Miao, H. He, Z. Alpichshev, A. Kapitulnik, R.R. Biswas, L.A. Wray, "Disorder Enabled Band Structure Engineering of a Topological Insulator Surface." *Nature Communications*, **8** (2017) 14081.
- [13] L. Miao et al, "Observation of a Topological Insulator Dirac Cone Reshaped by Non-Magnetic Impurity Resonance." *npj Quantum Materials*, **3** (2018) 29.
- [14] Y. K. Kato, R. C. Myers, A. C. Gossard, D. D. Awschalom, "Observation of the Spin Hall Effect in Semiconductors." *Science*, **306** (2004) 1910.
- [15] H. J. Zhang, C. X. Liu, X. L. Qi, X. Dai, Z. Fang, S. C. Zhang, "Topological Insulators in Bi₂Se₃, Bi₂Te₃ and Sb₂Te₃ with a Single Dirac Cone on the Surface." *Nature Physics*, **5** (2009) 438.
- [16] M. Z. Hassan, C. L. Kane, "Colloquium: Topological Insulators." *Reviews of Modern Physics*, **82** (2010) 3045.
- [17] Y. Xia et al., "Observation of a Large-Gap Topological-Insulator Class with a Single Dirac Cone on the Surface." *Nature Physics*, **5** (2009) 398.
- [18] Y. Okada, W. Zhou, D. Walkup, C. Dhital, S.D. Wilson, V. Madhavan, "Ripple-Modulated Electronic Structure of a 3D Topological Insulator." *Nature Communications*, **3** (2012) 1158.
- [19] H. Li, J. M. Shao, H. B. Zhang, D. X. Yao, G. W. Yang, "Resonant Tunneling in a Topological Insulator Superlattice." *Journal of Applied Physics*, **114** (2013) 093703.
- [20] J. An, C.S. Ting, "Surface States Scattering From a Step Defect in the Topological Insulator Bi₂Te₃." *Physical Review B*, **86** (2012) 165313.
- [21] D. Zhang, C. S. Ting, "Impact of Step Defects on Surface States of Topological Insulators." *Physical Review B*, **85** (2012) 115434.
- [22] T. Chiba, S. Takahashi, G.W. Bauer, "Magnetic-Proximity-Induced Magnetoresistance on

- Topological Insulators." *Physical Review B*, **95** (2017) 094428.
- [23] M. Arabikhah, A. Saffarzadeh, "Surface State Transport in Double-Gated and Magnetized Topological Insulators with Hexagonal Warping Effects." *Journal of Physics: Condensed Matter*, **31** (2019) 445001.
- [24] H. Dehnavi, A.A. Masoudi, M. Saadat, H. Ghadiri, A. Saffarzadeh, "Electron Scattering in a Superlattice of Line Defects on the Surface of Topological Insulators." *Journal of Physics: Condensed Matter*, **32** (2020) 415002.
- [25] Y. L. Chen et al., "Experimental Realization of a Three-Dimensional Topological Insulator, Bi_2Te_3 ." *Science*, **325** (2009) 178.
- [26] L. Fu, "Hexagonal Warping Effects in the Surface States of the Topological Insulator Bi_2Te_3 ." *Physical Review Letters*, **103** (2009) 266801.
- [27] K. Kuroda et al, "Hexagonally Deformed Fermi Surface of the 3D Topological Insulator Bi_2Te_3 ." *Physical Review Letters*, **105** (2010) 076802.
- [28] U. Fano, "Effects of Configuration Interaction on Intensities and Phase Shifts." *Physical Review*, **124** (1961) 1866.
- [29] A. Saffarzadeh, "Tunnel magnetoresistance in double spin filter junctions." *Journal of Physics: Condensed Matter*, **15** (2003) 3041.
- [30] M. Chshiev, D. Stoeffler, A. Vedyayev, K. Ounadjela, "Magnetic Diode Effect in Double Barrier Tunnel Junctions." *Europhys.letters*, **58** (2002) 257.
- [31] A. Kalitsov, A. Coho, N. Kioussis, A. Vedyayev, M. Chshiev, and A. Granovsky, "Impurity-induced tuning of quantum well states in spin-dependent resonant tunneling" *Physical Review Letters*, **93** (2004) 046603.
- [32] M. Wilczynski, J. Barnas, "Tunnel magnetoresistance in ferromagnetic double-barrier planar junctions: Coherent tunneling regime." *Journal of Magnetism and Magnetic Materials*, **221** (2000) 373.
- [33] M. L. Teague et al., "Observation of Fermi-Energy Dependent Unitary Impurity Resonances in a Strong Topological Insulator Bi_2Se_3 with Scanning Tunneling Spectroscopy." *Solid state commun*, **152** (2012) 747.
- [34] Z. Alpichshev et al, "STM Imaging of Impurity Resonances on Bi_2Te_3 ." *Physical Review Letters*, **108** (2012) 206402.



Electrical properties of magnetic tunnel junctions affected by two types of interfacial roughness

Scientific research paper

Zhaleh Ebrahimnejad*

Department of Physics, West Tehran Branch, Islamic Azad University, Tehran, Iran

ARTICLE INFO

Article history:

Received 25 December 2021

Revised 6 January 2022

Accepted 9 January 2022

Available online 27 January 2022

Keywords:

Interfacial roughness

Tunnel magnetoresistance

Electrical properties

Spin polarization

ABSTRACT

The theoretical study has been done for investigating the effect of two types of rough interfacials on the electrical properties of magnetic tunneling structures. Surface roughness is found to have a strong influence on the spin polarized transport through magnetic tunneling junctions. The scattering mechanism because of rough interfaces causes reduction of the maximum achievable value for transmission probability resonance. Also, the presence of roughness interfacial causes a change in the spin polarization and the tunneling magnetoresistance ratios. The asymmetry distribution of the density of states may be reduced while the spin polarization and the tunneling magnetoresistance show an irregular behavior.

1 Introduction

Tunneling magnetoresistance (TMR) discusses the dependence of the resistance of magnetic tunnel junctions (MTJs) on the relative orientation of the magnetization directions of the ferromagnetic electrodes when their orientations changes from antiparallel AP to parallel P; $TMR = \frac{G_P - G_{AP}}{G_P} \equiv \frac{R_P - R_{AP}}{R_P}$ [1,2]. Spin Filter (SF) tunneling has become a very active part of research, many efforts have been devoted to this field because of large values of TMR discovery [3,4]. During the last two decades, spintronics which indicates the manipulation of electron spin along with its charge is an interesting field of research. It is applied in a wide variety of applications such as precise detection of defective cells, data designing of single as well as parallel logic gates, computer and mobile games, storage to robotics, speed control and navigation [5-8].

The method of interfaces production has a strong effect on the magnitude and polarization of the transport through MTJs. The information about the interfaces and details of models of the interfaces are the necessary step to analyze the electrical properties of MTJs theoretically and experimentally [3-5]. Several methods have been applied to simulate the tunneling structures interfaces to describe the transport phenomena through heterojunctions, theoretically. The diagrammatic techniques within diffusive perturbation theory [9], the transfer matrix method that treats each rough interface separately [10], and the diagrammatic techniques within the Born approximation [11]. The actual MTJs contain large amounts of roughness at the interfaces between the structure layers because there are many various models that have been used to generate them. Actually, the transport through MTJs affected by the roughness type of interfaces [12] and on the other hand, due to the existence of large spin dependent

*Corresponding author.

Email address: Ebrahimi.zhaleh@wtia.ac.ir

DOI: 10.22051/jitl.2022.38934.1065

scattering, magnetic materials exhibit the high degree of SP and the TMR [13, 14] Many researches have been done to investigate the characteristics of polarized currents [15–18].

Here, the roughness scattering from the two interfaces in a double barrier MTJs has been studied. The first and third interfaces have been considered rough. The type of first interface roughness is different from the third one. They have been generated by Ballistic deposition (BD) and Random Deposition (RD) models, respectively. Indeed, in this paper the effect of two different types of used rough interfacials in MTJs structures have been investigated simultaneously on the spin dependent transport properties of MTJs.

2 Method and results

The nearly free electron approximation and the transfer matrix method have been used to calculate the electronic properties in order to study the effect of roughness type on TMR and spin polarized transport in MTJs. The MTJ considered here consists of the NM layer and two ferromagnetic semiconductor barriers. Based on the experimental works results the top and bottom interfaces have dissimilar structures in heterojunctions, and bottom/top interfacials could be much rougher or smoother than the bottom/top interfacials depending on the growth conditions [19]. Hamiltonian in the presence of applied voltage V_a , is considered as

$$H_j(Z) = \frac{-\hbar^2}{2m_j^*} \frac{d^2}{dz^2} + V_j(Z) + V_j^\sigma, \quad j=1-5 \quad (1)$$

where m_j^* is the effective mass in 5 regions:

$$V_j(z) = \begin{cases} 0, & (j = 1) \\ E_F + V(r_{\parallel}, z) - \frac{eV_a}{4}, & (j = 2) \\ -\frac{eV_a}{2}, & (j = 3) \\ E_F + V(r_{\parallel}, z) - \frac{3eV_a}{4}, & (j = 4) \\ -eV_a, & (j = 5) \end{cases} \quad (2)$$

that, $V(r_{\parallel}, z) = \phi_0[\theta(z - f(r_{\parallel}))]$, where $\theta(z)$ is the unit step function and $f(r_{\parallel})$ is interface thickness of the rough interfaces [19]. The wave function presents as

$$\psi_j = \sum_q (a_{j\sigma}^\gamma(\mathbf{q})e^{(ik_j z)} + b_{j\sigma}^\gamma(\mathbf{q})e^{-(ik_j z)})e^{(i\mathbf{q}\cdot\mathbf{r}_{\parallel})}, \quad (3)$$

in each region. $\mathbf{q}=(q_x, q_y)$ is the transverse wave vector, k_j is the wave numbers in each j th region, and $\mathbf{r}_{\parallel} = (x, y)$ is the in-plane coordinate vector. $a_{j\sigma}^\gamma(\mathbf{q})$ and $b_{j\sigma}^\gamma(\mathbf{q})$ correspond to forward and backward propagation states, respectively. The direct and scattered components of the transmission probability have been denoted by $\gamma = 0$ and \pm . Based on the transfer matrix:

$$\begin{bmatrix} a_{5\sigma}^{(+)} \\ a_{5\sigma}^{(0)} \\ a_{5\sigma}^{(-)} \\ 0 \\ 0 \\ 0 \end{bmatrix} = M \begin{bmatrix} 0 \\ a_{1\sigma}^{(0)} \\ 0 \\ b_{1\sigma}^{(+)} \\ b_{1\sigma}^{(0)} \\ b_{1\sigma}^{(-)} \end{bmatrix}, \quad (4)$$

where $a_{1\sigma}^{(\pm)} = 0$ denotes that in layer 1 there is only the direct incident component [19].

$b_{5\sigma}^{(\gamma)} = 0$ since there is no reflection in the last region. The transmission through the MTJs can be considered by the continuity conditions of the wave function ψ and the probability current density of the electron $(1/m^*)(d\psi/dz)$ as follows

$$T_\sigma^{(\gamma)}(E_z, V_a) = \frac{k_5^{(\gamma)}}{k_1^{(\gamma)}} \frac{m_1^*}{m_5^*} \left| \frac{a_{5\sigma}^{(\gamma)}}{a_{1\sigma}^{(\gamma)}} \right|^2, \quad (5)$$

Total transmission is achieved by $T_{tot} = \sum_\gamma T^{(\gamma)}$. [19]. Moreover, the current density can be written as [20]

$$j(V_a) = \frac{em^*K_B T}{4\pi^2\hbar^3} \int_0^\infty T(E_z, V_a) \ln \frac{1 + \exp\left(\frac{E_F - E_z}{K_B T}\right)}{1 + \exp\left(\frac{E_F - E_z - eV_a}{K_B T}\right)} dE_z, \quad (6)$$

where $T(E_z, V_a)$ is the transmission probability. As presented before, the spin polarization is obtained from the current densities, $sp = \frac{j_{\uparrow} - j_{\downarrow}}{j_{\uparrow} + j_{\downarrow}}$. $J_{\uparrow(\downarrow)}$ and $J_{P(AP)}$ are the portion currents of spin up (down) and parallel (anti-parallel) configurations, respectively [21,22]. The values of used parameters are as the following. The thicknesses of barriers and quantum wells are 0.5 and 0.75 nm, respectively. $m_1 = m_0$ and $m_2 = 1.5m_0$ for the electron effective mass in NM and FMS materials, respectively which m_0 is the electron mass in free space. Also, E_F is the electron Fermi energy which has been taken as 1.25eV. The parameters for EuS barrier layers are $I = 0.1\text{eV}$ and $S = 7/2$ [23], and T_c is 16.5K [24,25]. In the calculation, the applied voltage is $V_a = 50\text{mV}$.

For each spin, there are two fundamental parallel conduction channels in SF structures. The net current density is the average of the spin-up and spin-down current densities $j_{\text{net}} = (j_{\text{up}} + j_{\text{down}})/2$. Indeed the Spin-up and spin-down electrons fell the different heights of the barriers and therefore, the spin channel with the lesser barrier height has a greater transmission coefficient. This indicates that the current entering the collector electrode is spin polarized. The first and third rough interfaces have been produced by two standard models of deposition, BD and RD respectively. Random deposition (RD) is the simplest model of surface generation which during this model each particle is randomly released over a position (site) of a surface and added to the top of the selected column. The produced interface/surface is uncorrelated because the growth of columns is independent of each other. The common deposition model is the Ballistic deposition (BD). In this model, a particle is dropped over a randomly chosen position (site) above the surface located at a distance that is larger than the maximum height of the interface, therefore the surface heights depend on the neighboring columns heights and hence the generated interface/ surface is correlated [26,27]. As a difference of the present work with previous ones, it is interested to investigate the effect of two types of interfacials

roughness on the electrical properties of MTJs, simultaneously.

Figure. 1 shows the spin filter transmission probability through MTJs with mentioned rough interfaces. The resonant tunneling in these curves occur when the incident electron energy coincides with the energy of the lowest quasi-bound energy level in the quantum well. For a MTJs with perfect interfaces, the transmission probability reaches unity at the resonance.

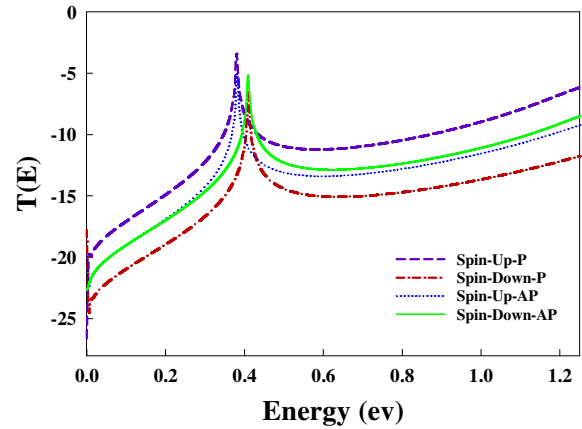


Figure 1. The logarithm of Spin filter transmission probabilities as a function of incident electron energy for two different spin orientations and parallel and antiparallel alignments. .

The scattering mechanism because of rough interfaces causes a reduction of the maximum achievable value of transmission probability resonance. The calculations have been carried out at $T=0\text{K}$.

The transmission coefficient for the spin-up orientation of electrons in the parallel alignment is higher than the spin-down electrons and also higher than the two-spin orientations at anti-parallel alignment. Also there is a small difference in the current density in both magnetic configurations. Based on the results of Fig. 1, for the electrons with spin- up orientation the transmission probability in the parallel alignment has the bigger values than the spin-down electrons. Moreover, it is bigger than the two-spin orientations at anti-parallel alignment. There is a small difference in the current density in both magnetic configurations.

In order to investigate the effect of temperature variations on the transport through rough MTJs, the transmission probability has been calculated for spin-up orientation and parallel alignment.

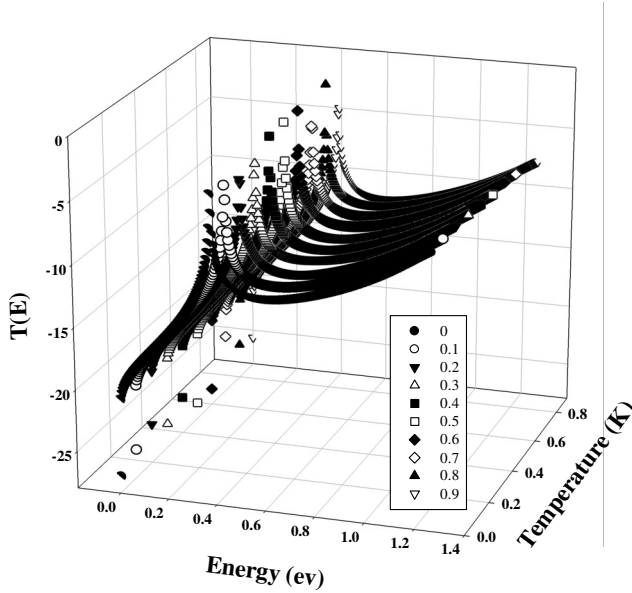


Figure 2. The logarithm of transmission probability has been calculated for spin-up orientation and parallel alignment for different values of temperature.

The results present the temperature dependence of the spin polarization for MTJs with rough interfaces. At temperatures $T > T_c$, there is no spin splitting. This splitting ascribed to the exchange splitting of the EuS conduction band. Therefore, the transmission coefficients for two spin orientations coincide [12].

Figures 3 and 4, show the spin polarization and the TMR as a function of the NM (quantum well) layer thickness at $T = 0$ K while the bias voltage $V_a = 50$ mV is applied to the junction.

Based on the results, TMR and spin polarization oscillate by increasing the thickness of the NM layer. For the MTJs with perfect (no rough) interfaces, TMR and spin polarization have the well-defined peaks. The origin of this oscillatory behavior is related to the quantum-well states of the NM layer and the spin-polarized resonant tunneling. An electron entering on a MTJ has a maximum quantum mechanical tunneling probability and its energy agrees to a resonant state in the NM layer. The height of peaks reduces as the thickness of NM layer increases [25, 27, 28].

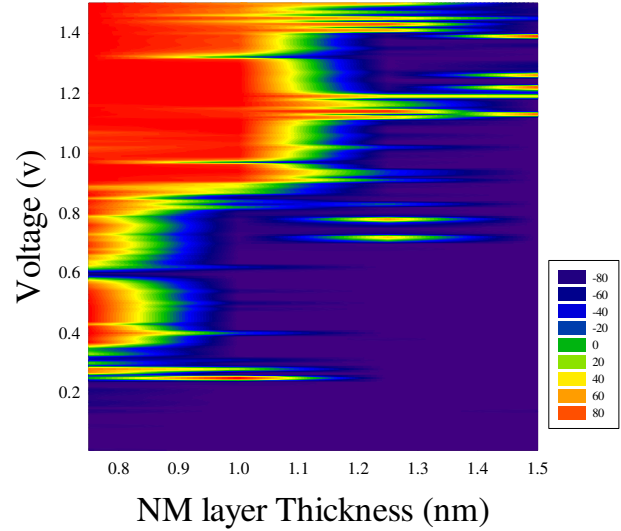


Figure 3. Spin polarization as a function of the thickness of NM well layer and applied voltage, at $T = 0$ K.

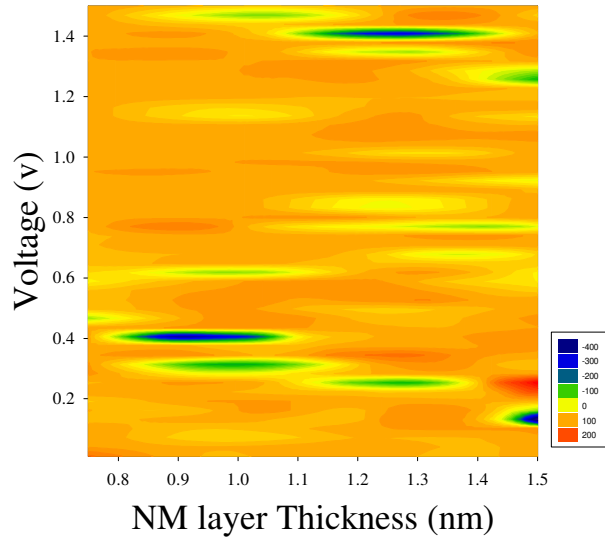


Figure 4. TMR as a function of the thickness of NM well layer and applied voltage, at $T = 0$ K.

Based on Figs. 3 and 4, the spin polarization and the TMR change periodically as the variation of NM layer thickness. The period and value of these parameters vary as a function of the applied voltage and the NM layer thickness. The presence of roughness interfacial may cause spin-flip scattering through the transport. This could be the origin of change in the spin polarization and the TMR quotients. Because, some of the majority electrons change their spin orientation and they tunnel into the corresponding minority states.

Therefore, the asymmetry distribution of the density of states may be reduced. Moreover, the location and the amount of resonant energies vary by increasing the NM layer thickness.

The electron scattering phenomena can create the valleys and peaks resonance energies. This indicates that for MTJs by rough interfaces, the spin polarization and the TMR show an irregular behavior. The results are in a good agreement with experiments, electron transport via imperfections and roughness goes to a reversal in the sign of the SP and the TMR ratios while typical nonlinear tunneling currents have been observed in the current-voltage characteristics [3]. These behaviors of the spin polarization and the TMR reveal the influence of interfaces roughness type [27, 28]. Also, changing the rough interfaces in MTJ has no effective effect on the obtained results.

4 Conclusions

In the present study, the effect of two different types of rough interfacials in a magnetic tunneling structure has been investigated. The first and third interfacials have been generated with two different standard models of deposition. The transport properties of the MTJs have been calculated, the results show that the scattering mechanism because of rough interfaces tends to reduce the maximum achievable value of the transmission probability resonance. Also, the spin polarization and the tunneling magnetoresistance ratios are strongly affected by the roughness, while the asymmetry distribution of the density of states is reduced as they present the irregular behaviors.

References

- [1] P. X. Xu, "Influence of roughness and disorder on tunneling magnetoresistance." *Physical Review B*, **73** (2006) 180402R.
- [2] Y. Li, Ch.-Ray. Chang, "Influence of interfacial roughness on the tunnel magnetoresistance." *Physics Letters A*, **287** (2001) 415.
- [3] T. Kado, "Large room-temperature inverse magnetoresistance in tunnel junctions with a Fe_3O_4 electrode." *Applied Physics Letters*, **92** (2008) 092502.
- [4] H. Wu, et al., "Spin-dependent transport properties of $\text{Fe}_3\text{O}_4/\text{MoS}_2/\text{Fe}_3\text{O}_4$ junctions." *Scientific Reports*, **5** (2015) 15984.
- [5] Zh. Zhu, et al., "Magnetic and transport properties of amorphous, B2 and L_{21} Co_2MnGa thin films." *AIP Advances*, **10** (2020) 085020.
- [6] Arpita Koley, Santanu K. Maiti, Judith Helena Ojeda Silva, David Laroze, "Spin Dependent Transport through Driven Magnetic System with Aubry-Andre-Harper Modulation." *Applied Sciences*, **11** (2021) 2309.
- [7] L. D. Yuan, et al., "Giant momentum-dependent spin splitting in centrosymmetric low-Zantiferromagnets." *Physical Review B*, **102** (2020) 014422.
- [8] Y. Jiao, et al., "First-Principles Prediction of Spin-Polarized Multiple Dirac Rings in Manganese Fluoride." *Physical Review Letters*, **119** (2017) 016403.
- [9] P. Johansson, "Theory for light emission from a scanning tunneling microscope." *Physical Review B*, **42** (1990) 9210(R)
- [10] W. T. Dietz, R. B. Darling, "Coherent electron transport across semiconductor heterojunctions with rough interfaces." *Physical Review B*, **53** (1996) 3925.
- [11] J. Leo, A. H. MacDonald, "Disorder-assisted tunneling through a double-barrier structure." *Physical Review Letters*, **64** (1990) 817.
- [12] C. W. Miller, "The critical role of the barrier thickness in spin filter tunneling." *Journal of Magnetism and Magnetic Materials*, **321** (2009) 2563.
- [14] W. Long, et al., "J. Gate-controllable spin battery." *Applied Physics Letters*, **83** (2003) 1397.
- [15] P. Zhang, et al., "Spin Current through a Quantum Dot in the Presence of an Oscillating Magnetic Field." *Physical Review Letters*, **91** (2003) 196602.
- [16] O. Földi, et al., "Quantum rings as electron spin

- beam splitters.” *Physical Review B*, **73** (2006) 155325.
- [17] N. Hatano, et al., “Non-Abelian gauge field theory of the spin-orbit interaction and a perfect spin filter.” *Physical Review A*, **75** (2007) 032107.
- [18] M. Dey, et al., “Spin Hall effect in a Kagome lattice driven by Rashba spin-orbit interaction.” *Journal of Applied Physics*, **112** (2012) 024322.
- [19] O. Földi, et al., “Networks of Quantum Nanorings: Programmable Spintronic Devices.” *Nano Letters*, **8** (2008) 2556.
- [20] H.C. Liu, and D.D. Coon, “Interface-roughness and island effects on tunneling in quantum wells.” *Journal of Applied Physics*, **64** (1988) 6785.
- [21] M. Wilczynski, J. Barnas, “Tunnel magnetoresistance in ferromagnetic double-barrier planar junctions: Coherent tunneling regime.” *Journal of Magnetism and Magnetic Materials*, **221** (2000) 373.
- [22] E. Y. Tsymbal, O. NMryasov, and P. R LeClair, “Spin-dependent tunneling in magnetic tunnel junctions.” *Journal of Physics: Condensed Matter*, **15** (2003) R109.
- [23] I. Žutić, J. Fabian, S. Das Sarma, “Spintronics Fundamentals and Applications.” *Reviews of Modern Physics*, **76** (2004) 323.
- [24] A. Saffarzadeh, “Tunnel magnetoresistance in double spin filter junctions.” *Journal of Physics: Condensed Matter*, **15** (2003) 3041.
- [25] G. Baum, et al., “Field emission of monoenergetic spin-polarized electrons.” *Applied Physics*, **14** (1977) 149.
- [26] Zh. Ebrahiminejad, et al., “The study of transport properties in rough ferromagnetic semiconductor rough junctions.” *Physica E*, **48** (2013) 70.
- [27] A. L. Barabasi and H. E. Stanley, *Fractal Concepts in Surface Growth*, Cambridge University Press, New York, (1995).
- [28] V. D. Costa, et al., “Tunneling Phenomena as a Probe to Investigate Atomic Scale Fluctuations in Metal/Oxide/Metal Magnetic Tunnel Junctions.” *Physical Review Letters*, **85** (2000) 876.
- [29] D. Bagrets, A. Bagrets, A. Vedyayev, B. Dieny, “Influence of s-d interfacial scattering on the magnetoresistance of magnetic tunnel junctions.” *Physical Review B*, **65** (2002) 064430.